HySA/Catalysis Centre of Competence, Catalysis Institute

Department of Chemical Engineering

University of Cape Town

Fabrication of Catalyst Coated Membranes by Ultrasonic Spray for Proton Exchange Membrane Water Electrolysers

Submitted in partial fulfilment of the requirements of the degr ee of

Master of Science in Chemical Engineering

Author: Nyasha Mawungwe

Supervisor: Dr. Rhiyaad Mohamed

Co-supervisor: Dr. Darija Susac

February 2023

Abstract

Renewable hydrogen, referred to as green hydrogen (GH), holds significant importance in the endeavour to decarbonise the transportation and industrial sectors. GH is generated via the electrochemical process of water splitting, utilising excess renewable energy sources such as solar and wind, thus serving as a sustainable means of energy storage.

The production of GH can be done in a proton exchange membrane water electrolyser (PEMWE), by splitting water into hydrogen and oxygen utilising an important component called the catalyst-coated membrane (CCM). The CCM is composed of a membrane coated with noble metal-based catalyst nanoparticles that make up the anode and cathode electrodes. The sluggish anode kinetics and the elevated cost associated with the CCM have acted as barriers to the widespread acceptance of PEMWEs. In this study, we used ultrasonic spraying for catalyst coating. Previous research suggests that optimising these parameters can enhance PEMWE performance and commercial viability.

The research conducted involved an ultrasonic spraying parameter variation and an anode catalyst loading study. The ultrasonic spraying variation investigated the nozzle height and nozzle speed. The anode catalyst ink was formulated from a commercial catalyst and applied to each membrane forming a half CCM, and thereafter, combined with a commercially developed cathode to form a full CCM. The CCMs were physically characterised, and electrochemically tested. The results were compared to assess the impact of ultrasonic spraying parameters and anode loading on performance and catalyst utilisation. The fabricated samples with approximately 2 mg Ir anode loading were further compared to a commercial CCM benchmark, considering the CL surface, microstructure, performance, and catalyst utilisation.

The results showed the influence of spraying parameters, catalyst type, and loading on microstructure, performance, and utilisation. This showed the importance of optimising parameters and loading to develop comparable low-loaded catalyst layers to assist PEMWE adoption.

Acknowledgements

I would like to extend my gratitude to everyone who has assisted me and made this study possible. Firstly, I wish to thank my supervisors Rhiyaad Mohamed and Darija Susac. Darija Susac for her selfless sharing of knowledge in her expertise, patient equipment training, and frequent constructive feedback. I am immeasurably grateful for her time investment in developing my skills in becoming familiar with sample preparation for microscopy, operating laboratory imaging equipment, and editions to this study report. I am deeply grateful to Rhiyaad for giving me the amazing opportunity to study under his supervision and for imparting his knowledge on CCM performance testing, academic paper critiquing, academic writing, academic presenting, and providing me with invaluable feedback on this thesis.

A special thanks goes to Ziba Rajan for giving up time from her research to train me on equipment used for catalyst ink preparation, operating the ultrasonic spraying machine, and for student research advice. I would like to thank Iosif Vazirgiantzikiz for assisting me with SEM sample preparation, SEM equipment training, and for developing the catalyst layer thickness analysis method steps. I also want to thank Miranda Waldron (Center for Imaging and Analysis, UCT) for always being willing to share her expert knowledge in microscopy work and assist with imaging tasks outside my trained skills. My gratitude goes to Dr Assistant Prof Jasna Jankovic and her student Amir Peyman Soleymani from the University of Connecticut for conducting the STEM-EDX characterisation for this study's samples. Many thanks go to Joe Itota and Jonathan Kiangani for assisting with the CCM performance testing. Clayton Jacobs and Tshepang Tsieane for your willingness to acquaint me with general laboratory protocols and safety rules.

I want to thank my family and friends for their unconditional love and consistent support during this study. A special thanks to my mother Rose Choice and father Albert that have made countless sacrifices to ensure I get the best opportunities to succeed. Tinashe my brother for always encouraging me when I have felt distressed, and lastly my friends Archippe Manzila and Deborah Chikukwa who have shared this master's journey with me. I appreciate you all.

Plagiarism Declaration

1. I know that plagiarism is wrong. Plagiarism is to use another's work and to pretend that it is one's own.
2. I have used the Harvard system for citation and referencing. Each significant contribution to, and quotation in, this report from the work, or works, of other people has been attributed, and has been cited and referenced.
3. This report is my own unaided work, except for assistance received from the teaching staff.
4. I have not allowed, and will not allow, anyone to copy my work with the intention of passing it off as his or her own work.

Signed by candidate

_____

Signature

Table of Contents

List of Figures

List of Tables

1 Introduction

1.1 Background

According to the International Energy Agency (IEA), fossil fuels contribute around 90% of the world's energy supply (IEA, 2017). This dependence on non-renewable resources is not a sustainable solution for the future of humankind. The consumption of fossil fuels leads to the formation of greenhouse gases (GHGs), which have been recognised as a major factor contributing to global climate change. Changes in weather patterns, an

increase in sea levels, and more extreme weather events are disrupting national economies and affecting lives, communities, and countries. Without mitigation action, the planet's average surface temperature is likely to exceed 3^{o}C, with irreversible consequences (Pettersson, Ramsey & Harrison, 2006). In the Paris Agreement outlined in 2016, countries agreed to limit the global temperature rise to below 2^{o}C, and achieving this goal requires the adoption of renewable energy sources to avoid world energy supply disruption (UNFCCC, 2015). Hydropower, solar, and wind are the most widely used renewable energy sources contributing to 91% of the total renewable energy production today (Whiteman Adrian et al., 2021)While the advantage is a potentially unlimited energy supply with zero GHG emissions, a major drawback of these renewable energy sources is the limited storage capacity.

Hydrogen can be a chemical energy storage solution. Currently, most hydrogen production is carried out via natural gas steam reforming (48%), oil reforming (30%), and coal gasification (18%) (Mohammadi & Mehrpooya, 2018). Water electrolysis produces only 4% of the total hydrogen, however when integrated with renewable energy sources such as solar and wind, it offers a GHG-free alternative process (Carmo & Fritz, 2013). In comparison to the more mature alkaline-electrolyser technology, the proton exchange membrane water electrolyser (PEMWE) system has a higher production rate, operates at a higher power density at low operating temperatures (80^{o}C), and has a more compact mass-volume ratio (Ma, Sui & Zhai, 2009). However, the slow kinetics of the oxygen evolution reaction (OER) at the anode and the high platinum group metal (PGM) requirements for anode

catalyst loadings have stifled the widespread economic success of this technology (Rashid et al., 2015).

The PEMWE electrolyser stack consists of stacked unit cells with the catalyst coated membrane (CCM) as the prime and most expensive component for each unit cell. The CCM consists of a Nafion® membrane separating the anode and cathode catalyst layers (CLs), where the OER and hydrogen evolution reaction (HER) occur, respectively. The CLs can be deposited directly onto the membrane using several methods such as screen printing, sputter deposition, doctor blade, Mayer rod, ultrasonic spraying, or indirectly via decal transfer. Ultrasonic spraying is one of the preferred methods due to its capability of high-precision catalyst deposition, low catalyst loadings, and production of reproducible CLs (Manco & Niedzwiecki, 2010). Both electrodes are produced from catalysts synthesized from scarce, expensive PGMs, namely iridium dioxide (IrO_2) for the anode and platinum (Pt) for the cathode.

The overall cell performance (E_{cell}) is influenced by the reversible cell voltage (E_{rev}) stated from the Nernst equation, and a sum of overpotential losses which are, ohmic losses (η_{ohm}) influenced by ionic and electronic charge transfers in cell components and contact resistances, kinetic losses (η_{act}) related to electrochemical reactions largely from the sluggish OER, and mass transport (η_{mtx}) predominantly from the two-phase flow on the anode porous transport layer (PTL_a), and O_2 bubble removal that hinders H_2O transportation to the catalyst active sites. Therefore, the electrode microstructure mostly affects the mass transport losses which decreases the overall cell performance (Pham et al., 2021). Fabrication method parameters can influence the anode CL microstructure and catalyst utilisation leading to a reduction in the anode overpotentials as well as catalyst loadings.

This study focuses on exploring the influence of selected ultrasonic spraying parameters on CCM catalyst layer microstructure and performance. Fabrication of the CCMs includes catalyst ink formulation using two commercially available catalysts, catalyst 1 (IrO_2/TiO_2 (75 wt.% Ir)) from undisclosed supplier 1 and catalyst 2 (IrO_x) from an undisclosed commercial supplier 2. For the ultrasonic spraying parameter study, the catalyst ink was formulated from catalyst 1, and for the catalyst loading evaluation

from catalyst 2. A methodology was developed for catalyst layer thickness measurements and microstructure evaluation. The following characterisation techniques were applied:

- Scanning Electron Microscopy (SEM), for surface morphology, membrane coverage, crack formation, catalyst layer evenness, thickness, and overall catalyst layer microstructure.
- Energy Dispersive X-Ray Spectroscopy (EDS) in combination with SEM and scanning transmission electron microscopy (STEM) for elemental analysis (detection) and distribution.

In-situ CCM performance evaluation was carried out as single-cell electrolyser tests using polarisation curves for catalyst layer structure-performance correlations and identification of optimal spraying process parameters for CCM production.

1.2 Research Scope

- Vary ultrasonic spraying nozzle height and speed to study the impact on anode catalyst layer morphology, thickness, porosity, and composition distribution.
- Fabricate CCMs with different anode catalyst loadings from 0.5 - 6 mg/cm^2 to determine the minimum loading needed for comparable performance to commercial CCM.
- Physically characterise fabricated CCMs using SEM, STEM-EDS to correlate structure to performance.
- Evaluate CCM electrochemical performance and catalyst utilisation via polarisation curves.
- Benchmark optimised ultrasonic-sprayed CCM to commercial CCM.

Key Questions:

- How do ultrasonic spraying nozzle parameters influence the anode catalyst layer microstructure and properties?
- What is the effect of anode catalyst loading on the catalyst layer morphology and electrolyser performance?
- Can optimisation of ultrasonic spraying produce low-loaded CCMs comparable to commercial standards?

Hypotheses:

- Increasing nozzle height will reduce catalyst loading while changing nozzle speed will cause variations in catalyst layer thickness.
- Higher anode catalyst loading will increase CL thickness and agglomerate size, influencing performance.
- Optimised ultrasonic spraying can produce homogeneous, low-loaded catalyst layers comparable to commercial CCMs.

1.3 Thesis Outline

This thesis consists of 7 chapters:

Chapter 1 – An introduction to this study.

Chapter 2 – Literature review of studies related to the study.

Chapter 3 – Describes the experimental steps conducted.

Chapter 4 – The method development, catalyst layer physical characterisation and thickness measurements techniques.

Chapter 5 – Discussion of the results obtained from the study.

Chapter 6 – Drawing conclusions from the study and making recommendations for future studies.

2 Literature Review

2.1 Hydrogen Economy

The transition towards a 'hydrogen economy' has the potential to contribute to reducing fossil fuel energy consumption, and carbon emissions as well as stimulate economic growth and create new jobs (Antonio Scipioni, Alessandro Manzardo & Jingzheng Ren, 2019). Our society is dependent on hydrogen as a reactant in chemical and petroleum processes, among these processes the vast quantity is for ammonia production (50%), petroleum processing (37%) and methanol production (8%)(Ramachandran & Menont, 1998). However, our current major hydrogen production processes are steam reforming natural gas (48%), oil reforming (30%), coal gasification (18%) and water electrolysis (4%) (Mohammadi & Mehrpooya, 2018). These statistics show that most of the hydrogen is still produced from carbon-based raw materials, contributing approximately 96% of the hydrogen supply. However,

these processes result in the production of greenhouse gases: SO_x, NO_x, CO_2, and CO as by-products. Therefore, to reduce or eliminate these emissions, there is a need to develop an environmentally friendly and economically viable carbon-free hydrogen production process. The electrolysis process, when coupled with solar or wind energy, offers a viable option. Since wind and solar energies have wide discrepancies between supply and demand, owing to the intermittent nature of these primary energy sources, the excess electricity can be used to power the water electrolysis process providing a sustainable solution to grid-scale electricity/chemical storage, referred to as a power to gas concept (Babic et al., 2017). Sustainable hydrogen can be used as a feedstock for chemical processes or as an end-use fuel in fuel cells for example, offers a solution to our current energy system challenges and sustainability goals (Ayers et al., 2019).

2.2 Water electrolysis

The main water electrolysis methods are proton exchange membrane (PEM) water electrolysis (PEMWE), alkaline water electrolysis (AWE), and solid oxide electrolysis (SOEC) (Rashid et al., 2015). AWE does not require noble metal-based (PGM) catalysts for electrodes, reducing initial capital costs. However, the drawbacks of this technology are; low current densities due to high ohmic losses, low load range, low H_2 purity due to electrolyte gas crossover, low operating pressures, bulky stack design, and a corrosive electrolyte composed of caustic potash solution 20-30% KOH. The AWE technology has become a mature hydrogen production process that can produce up to the megawatt range and is the current standard for large-scale electrolysis (Carmo & Fritz, 2013).

SOEC utilises a solid oxide or ceramic electrolyte for hydrogen and oxygen production. SOEC operates at high temperatures, typically between 500^{o}C and 850^{o}C, which reduces the process energy requirement. The technology's advantages are high Faraday efficiency of >100% at voltages as low as 1.07V (Laguna-Bercero, 2012) non-noble metal catalyst requirements, and high-pressure operability. The SOEC technology requires advances in stability and degradation for it to achieve large-scale commercialisation (Shiva Kumar & Himabindu, 2019).

Proton exchange membrane water electrolysis (PEMWE) is a technology that was initially developed by General Electric in the 1960s to solve the drawbacks associated

with AWE. The anode and cathode are separated by a perfluorosulfonic acid-based solid polymer electrolyte, i.e. Nafion®, which enables operation at high current densities >2A.cm^{-2} with low gas crossover rates (> 1.25 X 10^{-4} cm^3 .s^{-1}.cm^{-2} for Nafion® 117 at standard pressure). PEMWE has a shorter response time than AWE, produces higher purity H_2 (>99wt.%), and a higher voltage efficiency, with a more compact system design that is suitable for operating pressures up to 350 bar (Manco & Niedzwiecki, 2010). The drawbacks of PEM water electrolysis technology are related to the high noble metal catalyst requirements and high corrosive environments, resulting in high capital costs and low durability of the system. For PEMWE to be commercially viable, more efficient use of the noble metal catalysts is required (Shiva Kumar & Himabindu, 2019).

2.2.1 PEM water electrolysis operating principle

Figure 2.1 illustrates the PEMWE process, in which the CCM is compressed between two porous transport layers (PTLs) that provide mass transport pathways for water and product gases and ensures electron flow to the bipolar plates (BPP). The bipolar plates have flow channels that ensure an even flow of water over the PTLs. The PTLs enable a two-phase transport of water and oxygen at the anode and hydrogen at the cathode, respectively (Ayers et al., 2019). The membrane serves as a proton conductor, electron insulator, and gas separator between the electrodes. When voltage is applied, the water is electrochemically split into oxygen, protons, and electrons at the anode. Protons are conducted from the anode through the membrane to the cathode, and the electrons flow via an external circuit, where they recombine at the cathode to form hydrogen gas (Figure 2.1) (Rashid et al., 2015). The electrochemical reactions below outline the reactions that occur and the nonspontaneous PEMWE process that requires electrical energy;

Equation 2.1: Oxygen Evolution Reaction (OER) at the anode

$$2H_2O \rightarrow O_2 + 4H^+ + 4e^- \qquad E^0 = 1.23\ V$$

Equation 2.2: Hydrogen Evolution Reaction (HER) at the cathode

$$2H^+ + 2e^- \rightarrow H_2 \qquad E^0 = 0.00\ V$$

Equation 2.3: Overall reaction

$$H_2O \rightarrow H_2 + \frac{1}{2}O_2 \qquad \Delta E^0 = 1.23V$$

Equation 2.4: Water electrolysis (Naimi & Antar, 2018)

$$H_2O_{(l)} + (237.2kJ\ mol^{-1})_{electricity} + 48.6(kJ\ mol^{-1})_{heat} \rightarrow H_2 + \frac{1}{2}O_2$$

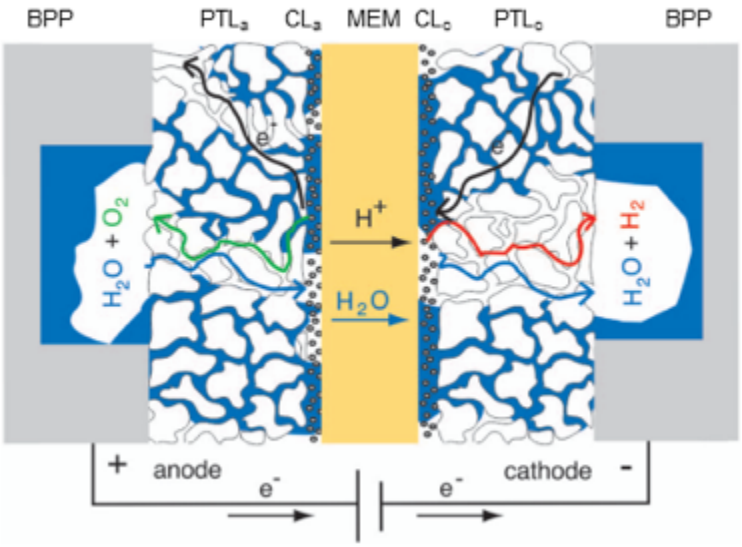

Figure 2.1: Cross section diagram of an electrolysis cell, consisting of a membrane (MEM) coated with anode and cathode catalyst layers (CLa and CLc, respectively) sandwiched between two porous transport layers (PTLc, PTLa) and bipolar plates (BPPs) (Babic et al., 2017)

2.3 Catalyst Coated Membrane (CCM)

As shown in Figure 2.1 the catalyst coated membrane consists of a membrane coated with catalyst layers on both sides, and the catalyst layers function as anode and cathode electrodes.

2.3.1 Membrane

The membrane must be effective in transporting the protons from the anode to the cathode. Perfluorosulfonic acid (PFSA) polymers such as Nafion®, Flemison®, Fumapen®, and Aciplex® are commonly used materials. Nafion membranes with thicknesses generally ranging between 100 μm to 200 μm, such as Nafion® 115 (127-micron), and Nafion® 117 (183-micron), have high oxidative stability and low gas (H_2, O_2) crossover rates, making them suitable for PEMWE applications (Tang, Karlsson & Cleghorn, 2006). However, Nafion membranes limit the choice of electrocatalysts for stability reasons, to Platinum Group-Metals (PGM) which have high activity and high stability, increasing the CCM material cost. For a three-layer

CCM, the catalyst layer is in direct contact with the membrane and the PTL or gas diffusion layer (GDL), to increase catalyst utilisation, electron conductivity, and mass transportation of reactants, H_2O and products H_2 and O_2 from the CL active sites. A GDL is a fibrous porous medium typically made from carbon paper or carbon cloth that has two main functions ensuring the uniform distribution of reactants, H_2O, on the electrode surfaces (anode/cathode), and the transportation of electrons to and from the external circuit (Abderezzak, 2018).

2.3.2 Catalyst layers

The commonly used cathode catalyst is platinum supported on carbon (Pt/C), while the anode uses unsupported iridium, iridium oxide, and iridium oxide supported on titanium dioxide (IrO_x/TiO_2). To reduce high anode overpotentials and lower catalyst costs, it is essential to understand and enhance the microstructure of the catalyst layer (Ayers et al., 2019). A state-of-the-art anode catalyst layer features multiple pathways that allow reactants and products to move in and out of the catalyst surfaces (Xu & Scott, 2010). Three-phase boundaries (TPB) are significant locations in the catalyst layer where reactant, catalyst, and ionomer come into contact, enabling an electrochemical reaction to take place. (Grigoriev, Porembsky & Fateev, 2006). These sites are affected by electrode wettability, proton conductivity, gas transport resistance, and water uptake, which influences CCM overpotential (Sci, 2014a). The catalyst layer (CL) can be studied using Scanning Electron Microscopy (SEM) and Energy dispersive X-ray spectroscopy (EDS), to determine morphology, thickness, uniformity, and elemental distribution (Xu & Scott, 2010).

2.3.3 Hydrogen evolution reaction (HER) cathode catalysts

HER catalysts are limited to Platinum Group Metals (PGM), with the typical HER catalyst being platinum, supported on carbon (Pt/C) (Bernt et al., 2020) (Rashid et al., 2015). Carbon serves as a suitable support material due to its good electron conductivity and high surface area, which enhances Pt distribution and improves catalyst utilisation. Studies have shown that a 0.05 $mg.cm^{-2}$ Pt catalyst loading is adequate for sustaining current densities of 2 $A.cm^{-2}$, due to the fast HER kinetics (Ayers et al., 2019). The significant PEMWE overpotential originates from the OER at the anode.

2.3.4 Oxygen evolution reaction catalysts (OER) anode catalysts

A state-of-the-art OER catalyst has high activity, high selectivity, high electrical conductivity at high potentials, high corrosion stability, and a high surface area to minimise noble metal requirements. A common method to produce high surface area catalysts is utilising porous powders synthesised by wet chemistry methods. Oxide-based catalysts are common due to their high resistance to corrosion at high potentials and acidic conditions (Sci, 2014b). Unsupported iridium, iridium oxide, and iridium oxide supported on titanium dioxide (IrO_x/TiO_2) are state-of-the-art anode catalyst materials for OER (Reier, Oezaslan & Strasser, 2012a). They potentiostatically determined the PGM catalytic activities as Ir > Rh > Pt, and further tests conducted by Miles and Thomason, added ruthenium, gold, and niobium, recorded, Ru > Ir > Pd > Rh > Pt > Au > Nb. Several catalyst factors affect its performance in the OER and these are crystal-field stabilisation energy, crystallinity, crystal size, and dispersion. IrO_2 exhibits higher corrosion-resistance but is less electroactive than RuO_2 (Reier, Oezaslan & Strasser, 2012b). Figure 2.2 shown below follows the Sabatier principle which suggests that for a two-step reaction passing through an intermediate such as the hydrogen reaction, the adsorption energy should be neither too high nor too low (endothermic). If it is too high (endothermic), the adsorption is slow and limits the overall rate, and if it is too low (exothermic), desorption from the catalyst surface is slow. Beginning from a high, positive (endergonic) adsorption energy, ΔG_{ad}, the rate initially increases (ascending section) with a decrease in ΔG_{ad}. Close to $\Delta G_{ad} \approx 0$ the rate passes through a maximum and then starts to decrease as ΔG_{ad} becomes more exogenic (descending section) (Quaino et al., 2014).

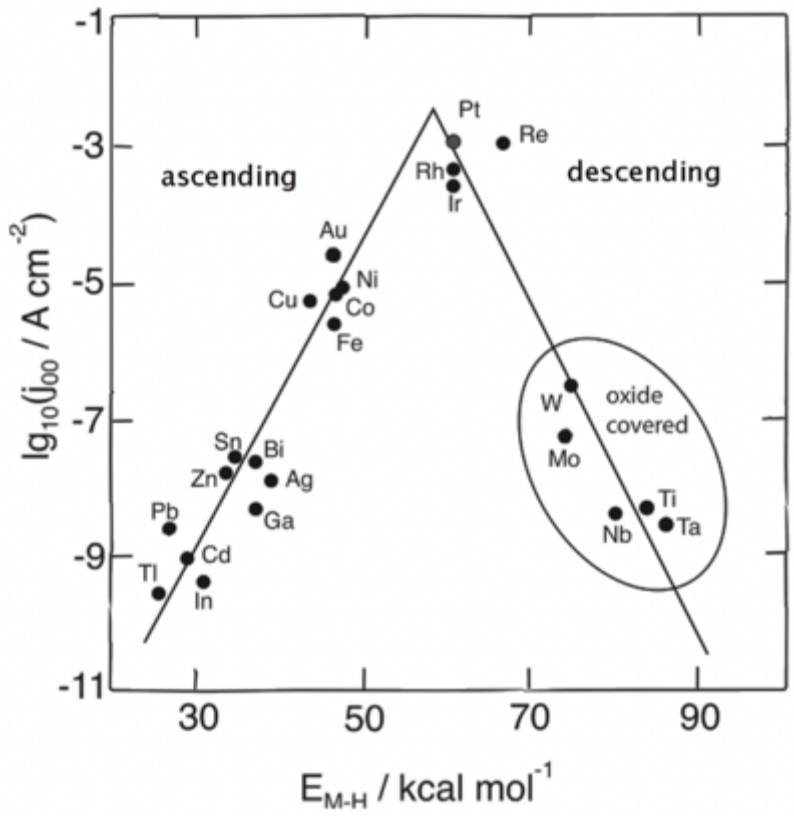

Figure 2.2: Trassati's volcano plot for the hydrogen evolution reaction in acidic conditions, j_{00} is the current density, and E_{MH}, is the hydride energy formation (Trasatti, 1972).

The theoretical activity values on the volcano plot assume ideal surfaces, which eliminates contributions from defects, crystal edges, or the formation of hydroxide layers. Ir is more suitable compared to Rh because it has high metallic conductivity and high stability in high potentials and acidic conditions (Sci, 2014c). The preparation procedure affects the performance and properties of the catalysts. Ir oxides produced at high temperatures have high crystallinity, high stability, but low performance. Catalysts produced at low temperatures have amorphous characteristics, high activity, but low stability in high potentials and acidic conditions (Spöri et al., 2019). Supporting iridium oxide (IrO_x) nanoparticles on conductive surface area materials such as TiC, TaC, TiO_2, or Ti increases mass-specific activity, and the most dimensionally stable catalyst preparation is via thermal decomposition of the metal precursors onto titanium (Reier, Oezaslan & Strasser, 2012b).

2.4 CCM fabrication methods

The CCM fabrication technique is crucial, as it can influence the composition, degradation, and catalyst layer-membrane interface, potentially leading to delamination (Xie et al., 2021). Various methods can be employed, depending on the desired objectives.. Catalyst layers for decal transfer are coated (brushing/spraying) on polytetrafluoroethylene (PTFE) sheets and typically hot-pressed onto the membrane (De las Heras et al., 2018). In the doctor blade method, the catalyst slurry is deposited on the membrane using a micropipette in front of a spreading blade, resulting in the formation of a catalyst layer (Carmo & Fritz, 2013). Similarly, for the Mayer rod technique, a Mayer rod is placed on top of the substrate and rolled over an excess catalyst ink, forming a wet catalyst layer (Bernt & Gasteiger, 2016). Ultrasonic spraying deposits the catalyst ink on the substrate without contact between the fabricating head and the substrate. An air-driven spray gun deposits the catalyst ink on the membrane, enabling high precision and homogenous low catalyst loadings (Bose, Keller & Boisen, 2013a). Ultrasonic spraying is well-suited for laboratory-scale experiments due to its requirement for small to moderate quantities of fabrication materials (ionomer, solvent, catalyst, etc.), enabling multiple variations in fabrication parameters and ensuring the high reproducibility of CCMs (Sassin et al., 2017a).

2.4.1 Ultrasonic spraying

During ultrasonic spraying, the catalyst ink is deposited by a spraying nozzle from a selected distance from the substrate (Figure 2.3). The advantages of ultrasonic spraying are atomized drop size control, which improves catalyst deposition precision, ultra-low flow rate, which enables low catalyst loading, and consistent spraying patterns, which improve reproducibility for manufacturing. These advantages despite low throughput make ultrasonic spraying a preferred deposition method for laboratory experiments because of the number of variables that can be tuned to form an optimal catalyst layer (Carmo & Fritz, 2013).

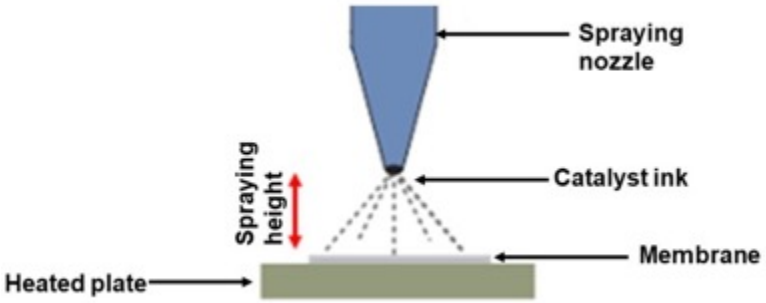

Figure 2.3: Ultrasonic spraying catalyst layer deposition (De las Heras et al., 2018)

2.4.2 Ultrasonic spraying parameters

Ultrasonic spraying is associated with many materials and process parameters that can be varied to fabricate a homogenous CL with high catalyst utilisation (Sci, 2014b). Variable parameters in ultrasonic spraying include the catalyst ink flow rate, number of passes, drying temperature, nozzle speed, nozzle height, air pressure, and pump rate. The extensive range of these parameters underscores the necessity for systematic process optimisation.

In a study by Boisen et al (2013), it was found that the distance between the nozzle and substrate, nozzle speed, and drying temperature had the most significant impact on achieving uniform polymer films. The researchers separated the drying and formation of the sprayed layer in a “dry” and “wet” regime. The wet regime was the equivalent of casting solution on the substrate followed by slow drying, while the drying regime had dry sprayed drops before covering the substrate surface. The optimum spraying conditions were in a narrow window between the two regimes. They used polyvinylpyrrolidone (PVP) to conduct a process parameter study of drying temperature, the distance between the spray nozzle and substrate, and spray nozzle speed. A statistical analysis was conducted, and it determined the distance between the nozzle and substrate as the most significant for depositing a uniform polyvinyl pyrrolidone (PVP) film (Bose, Keller & Boisen, 2013b).

In a parametric study by Endoo et al (2010), the fabrication of proton exchange membrane fuel cell (PEMFC) CCMs was investigated, with a focus on parameters such as drying time, drying atmosphere conditions, catalyst ink ionomer concentration, and drying temperature. The drying temperature had the most influence on CCM

performance, high drying temperatures caused high catalyst particle agglomeration, non-homogenous catalyst distribution, and low active surface area. The investigated drying temperatures were 50^{o}C, 80^{o}C, 100^{o}C, and 140^{o}C. In general, CCMs produced at lower temperatures showed better performance. CCM performance at 50^{o}C was an outlier and was caused by the partial drying of the solvent in the catalyst layer, which could have reduced electronic conductivity. The optimum drying temperature was 80^{o}C, and the catalyst layer had small catalyst agglomerates, 5.88 nm on average, high active surface area, and low ohmic losses of 0.19 ohms at 0.8V potential between the 10kHz and 10MHz range (Endoo, Pruksathorn & Piumsomboon, 2010). Alia et al (2020), performed a similar study by varying drying temperatures (40^{o}C, 60^{o}C, 90^{o}C, 100^{o}C, 110^{o}C). The drying temperature was varied by controlling the spray bed temperature and this affected the drying time of the ink when it contacted the membrane. At a lower temperature than the optimum temperature, 90^{o}C, the low performance was caused by a combination of lower kinetics and higher ohmic losses. The lower kinetics suggested a low catalyst-ionomer integration which was confirmed by thinner capacitances and higher polarisation resistances. At higher temperatures, there are kinetic losses, an increase in ohmic losses, and possible membrane changes which were observed by a slight colour change of the membrane from transparent to orange tinting (Alia et al., 2020).

The nozzle spraying speed had a notable impact on the quantity of catalyst deposited per pass. Lower nozzle speeds resulted in an increased thickness of the catalyst layer due to a greater amount of catalyst being deposited on the substrate per pass. Specifically, a spraying speed of 10 mm.s^{-1} yielded a more uniform sprayed film compared to higher speeds, which reached up to 50 mm.s^{-1} (Bose, Keller & Boisen, 2013b). Spraying height affected CL morphology. When varied between 3.5 cm – 6.4 cm, at 3.5 cm the CCM had more surface cracks than surfaces fabricated at higher heights, because the solvent had a longer timeframe for drying before depositing on the substrate. The surface cracks at a lower height were caused by the evaporation of excess solvent deposited on the membrane, which led to surface deformation during evaporation. At higher heights (5 cm and 6 cm), the solvent had a higher evaporation timeframe to the membrane, producing crack-free CLs, which agreed with results from a similar study performed by Sassin et al (2017). The findings suggested that the nozzle spraying height significantly impacts mass transport voltage losses.

Specifically, the shortest spraying distance from the membrane, at 3.5 cm, exhibited the highest mass transport losses and the lowest current density for a polymer electrolyte membrane fuel cell CCM. The excessive cracking in the CL at 3.5 cm may have impeded water removal at higher current densities, thereby potentially diminishing the overall performance of the CCM.

Alia et al (2020) performed a further study of varying the pump rate (0.1, 0.2, 0.3, 0.4 $ml.m^{-1}$) and the optimum CCM was sprayed at 0.2 $ml.m^{-1}$. Varying the pump rate affected how fast the ink got sprayed on the membrane, and the time required to spray CCMs varied from 24 minutes at 0.4 $ml.min^{-1}$ to 94 minutes at 0.1 $ml.min^{-1}$. It impacted the drying time of the ink, and the higher rates caused pooling of ink on the membrane, which resulted in high ohmic and transport losses because of nonuniform CLs. The kinetic performance was maintained and confirmed by the high exchange current densities, minimal capacitance was measured from cyclic voltammograms, and polarisation resistances from impedance spectra suggested an effective catalyst-ionomer interaction (Alia et al., 2020). These studies underscore the significance of comprehending the influence of ultrasonic spraying parameters on the deposited catalyst layer and their broader impact on CCM performance (Orfanidi et al., 2018).

2.5 Catalyst ink

A catalyst ink is a complex system comprised of a catalyst, a polymer, and a solvent; depending on the catalyst particle size (<50 nm), it can be considered a polymer/colloid system. Nano-scale interactions within the catalyst ink (polymer | catalyst, catalyst | solvent, and polymer | solvent) dictate ink macro-properties such as ink stability, rheology, and aggregation (Dixit et al., 2018a). These properties are influenced by catalyst concentration, solvent ratio, and ionomer loading in the catalyst ink, affecting the electrode microstructure formation, packing density, and ionomer distribution.

2.5.1 Formulation

Ultrasonic homogenisation (UH)

Ultrasonic homogenization (UH) involves mechanically mixing the catalyst, ionomer, deionised water, and solvent, which leads to a more uniform distribution of catalyst agglomerates. UH reduces particle diameter, hence increasing catalyst surface area.

There is a correlation between individual particle diameter and total surface area (Figure 2.4). UH reduces particle agglomeration in the suspension during settling and rising, and solid particles have an equivalent rising and settling speed required for homogenisation. The advantages of ultrasonic homogenisation to conventional homogenisation methods are the production of smaller agglomerates with a narrow size distribution, homogenisation of high solid concentrations, production of more stable suspensions, and manipulation of UH parameters (amplitude, time, power, and temperature) to produce more homogeneous mixtures (Hutagalung, 1967).

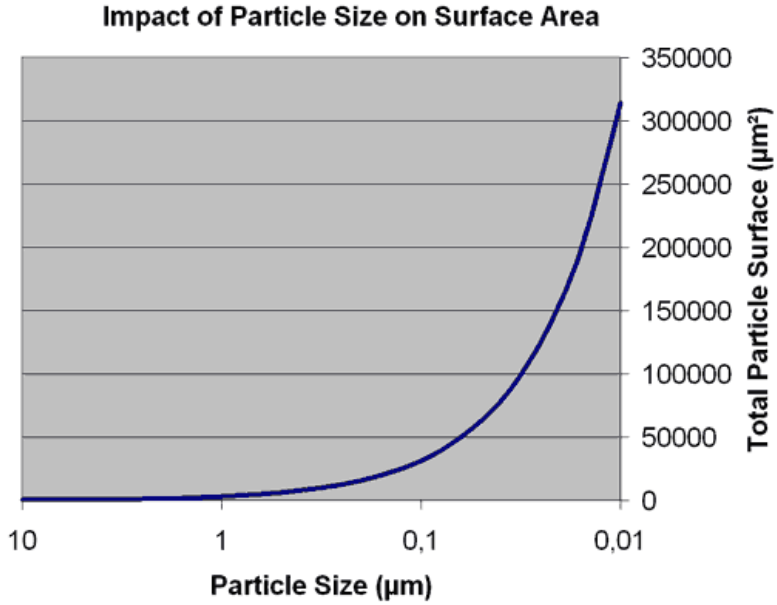

Figure 2.4: Relationship between total particle surface area and particle size effect (Hutagalung, 1967)

Catalyst ink ionomer content

The Nafion® ionomer in the catalyst layer has several functions: conducting protons from the membrane to the catalyst, binding the catalyst, creating sufficient gas channels, and retaining moisture in the catalyst layer (Xu & Scott, 2010). Additionally, catalyst ink ionomer content has a direct influence on CCM performance due to catalyst/ionomer interfacial resistance and catalyst layer resistance (Bernt & Gasteiger, 2016). Gasteiger et al (2016), conducted a study varying Nafion® content ratio between 2.2 wt% - 28 wt%, relative to the electrode weight for electrolyser anodes. They determined the Nafion® content to influence electrode volume fractions of catalyst (V_{cat}), wet ionomer ($V_{ion,\ wet}$), and void (V_{void}). The IrO_2/TiO_2 catalyst loading

(L_{cat}), and electrode thickness (t_{an}) were kept constant for all ionomer variations. The average catalyst density (ρ_{cat}) (86.9 wt% IrO_2 (11.7 $g.cm^{-3}$) and 13.1 wt% TiO_2 (4.23 $g.cm^{-3}$)) was 9.5 $g.cm^{-2}$ and the electrode thickness ranged between 8 – 12 μm. The Figure 2.5 below shows the correlations between the respective volume fractions and ionomer content.

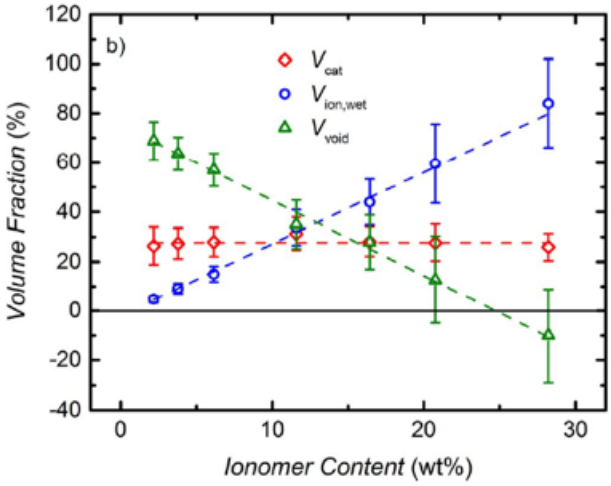

Figure 2.5: Anode electrode volume fractions vs ionomer content for IrO_2/TiO_2 (Umicore) catayst, V_{cat} (red), $V_{ion,wet}$ (blue), V_{void} (green). Determined by measuring deposited electrode weight and thickness (Bernt & Gasteiger, 2016).

From the diagram above, V_{cat} (IrO_2/TiO_2) was consistent for all electrodes at approximately 28%, and the remainder was occupied by wet ionomer or empty pores. The error bars represented standard deviations in measured electrode thicknesses. The wet ionomer volume ratio ranged between 5 – 72% and, 100% pore filling was at 25 wt% ionomer. The ionomer variation influenced the physical characteristics of the catalyst layer microstructure and voltage losses. The highest performing CCM was at 11.6 wt% Nafion, recording 1.57 V at 1 $A.cm^{-2}$, and the catalyst layer had $V_{void} \approx V_{ion,wet} \approx 35\%$ each. Below the optimum ionomer content, the performance decreased due to a limited proton conductivity in the electrode, which led to voltage losses.

Above the optimum Nafion content, ionomer filled the void volume, which increased electron contact resistance and electronic insulation of a fraction of the catalyst particles due to an ionomer film accumulation at the anode electrode/porous transport layer interface, which caused overpotentials and possible flooding of gas transport channels in the CL (cracks and pinholes in the ionomer layer) (Bernt & Gasteiger,

2016)(Xu & Scott, 2010). Alia et al. (2020), performed a similar study, varying the ionomer loading (Nafion ionomer 95.6 µl, 20 wt%, DE2020) between 0.05 and 0.8 $mg_{Nafion}\ mg_{Ir}^{-1}$. The study resulted in a varied overall CCM performance, primarily kinetic changes. The optimum ionomer loading was determined to be 0.2 $mg_{Nafion}\ mg_{Ir}^{-1}$. At low ionomer concentrations (0.05 – 0.3 $mg_{Nafion}\ mg_{Ir}^{-1}$), the CCM performance was minimally influenced, and the results were similar to the optimum ionomer range (0.15 – 0.3 $mg_{Nafion}\ mg_{Ir}^{-1}$). However, at higher ionomer amounts (0.6 – 0.8 $mg_{Nafion}\ mg_{Ir}^{-1}$), the kinetic losses increased, resulting in marginal increases in polarisation resistance and a reduction in capacitance. The slower kinetics and low capacitance were probably caused by limited access to Ir sites due to excess ionomer adsorbing onto Ir surfaces resulting in catalyst isolation (Figure 2.6).

An increase in transport losses at high ionomer content 0.6 – 0.8 $g_{Nafion}.g_{Ir}$ was observed, which could have been caused by excess ionomer inhibiting the oxygen/water diffusion. Additionally, higher ohmic losses were probably caused by the differences in the current distribution in the CL, since reactions occurred near the interfaces. Therefore, the optimal ionomer concentration between 0.15 and 0.3 $mg_{Nafion}\ mg_{Ir}^{-1}$ ensured contact between the catalyst active sites and membrane and reduced catalyst site isolation and blockage (Alia et al., 2020). Additionally, a separate study by Hegge et al (2019), determined excess ionomer deposition can be caused by partial sedimentation of catalyst ink in the syringe and spray coater tubes. In the study, they used thermogravimetric analysis (TGA) and recorded the ionomer in the CL as being approximately five times higher than expected from ink preparation, and therefore they recommended TGA measurements after fabrication for accurate final ionomer composition results (Hegge et al., 2019).

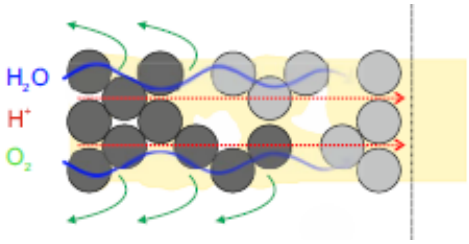

Figure 2.6: Inhomogeneous catalyst layer, with active catalyst particles (dark grey), pores(white) partially filled with ionomer (light brown), and electronically disconnected catalyst particles (light grey), resulting in electron insulation (Babic et al., 2019a)

Catalyst ink solvent

The catalyst ink requires a stable organic solvent in an oxidative environment. Polar protic solvents, methanol, ethanol, and isopropyl alcohol (IPA) are suitable for harsh oxidative environments. They form lowly defined and highly solvated, large ionomer agglomerates (Alcaide et al., 2017). Dixit et al (2018), formulated a catalyst ink without ionomer for IPA, octanol, and methanol, separately, with Vulcan carbon, and determined the IPA ink having the least agglomeration. However, adding Nafion ionomer minimised the solvent's influence on ink dispersibility and stability. Catalyst particles in ink systems without ionomer aggregated due to strong van der Waal forces at small separation distances, and adding ionomer resulted in entropic repulsion, which reduced particle agglomeration and produced a stable catalyst ink (Dixit et al., 2018b). Additionally, the solvent-to-deionised water ratio in the catalyst ink (CI) affects the overall performance of the CCM. Alia et al (2020), studied the influence of solvent ratios, n-propyl alcohol (nPA), at 0, 0.25, 0.33, 0.5, 0.6, 0.75, 1 $ml_{Water}\ ml_{nPA}^{-1}$, and recorded the optimal CCM performance in the 0.25 - 0.5 $ml_{Water}\ ml_{nPA}^{-1}$ range. For water-rich catalyst inks, the CCM performance was low due to a combination of slow kinetics and high ohmic losses (Alia et al., 2020). The ohmic losses were relatively larger, and the measured HFR increased from 121 mΩ for 0.33 $ml_{Water}\ ml_{nPA}^{-1}$ to 139 mΩ for 1 $ml_{Water}\ ml_{nPA}^{-1}$. The solvent ratio also affected the observable catalyst layer morphology, where the water-rich to water-only CIs produced nonuniform CLs due to the catalyst ink not completely drying with each spraying pass. Additionally, the low drying rates in the water-rich inks caused Ir aggregation/flocculation that contributed to the CL non-uniformity (primarily ohmic losses) and poor ionomer distribution (primarily kinetic losses) (Alia et al., 2020).

2.6 Characterisation techniques

2.6.1 Scanning Electron Microscopy (SEM)

SEM physical characterisation is an effective method for understanding the CL thickness, morphology, and overall microstructure properties. Gasteiger et al (2016), conducted SEM physical characterisations on CCM cross-sections (Figure 2.7). From SEM physical characterisation, the study determined catalyst layer thickness, attachment to the membrane, porosity, and homogeneity, as the microstructure

properties that affected proton transport resistance, electron conductivity, and overall CCM performance (Bernt & Gasteiger, 2016).

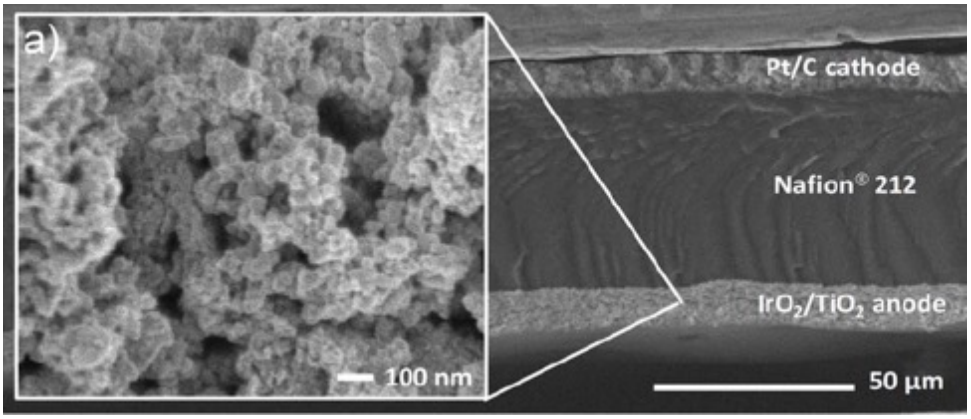

Figure 2.7: SEM image of anode CL cross-section from IrO_2/TiO_2 catalyst (Bernt & Gasteiger, 2016)

In a separate study Shukla et al (2019), utilised a Zeiss Sigma 300 VP field emission scanning electron microscopy (FESEM) to capture cross-sectional images of CLs Figure 2.8. For thickness measurements, they initially calculated the bulk volume (V_{bulk}) of the CL utilising the equation below,

Equation 2.5: V_{bulk} calculation from sample weight in air (S_a), sample weight in non-wetting (S_w), density of deionised water (ρ_{water}), density of octane (ρ_{octane}),

$$V_{bulk} = (\frac{S_a - S_w}{\rho_{water}})$$

After calculating V_{bulk} of the catalyst layer (t), Equation 2.6 below was used to calculate the thickness where (a X b) was the known cross-sectional area.

Equation 2.6: Catalyst layer thickness calculation

$$t = \frac{V_{bulk}}{ab}$$

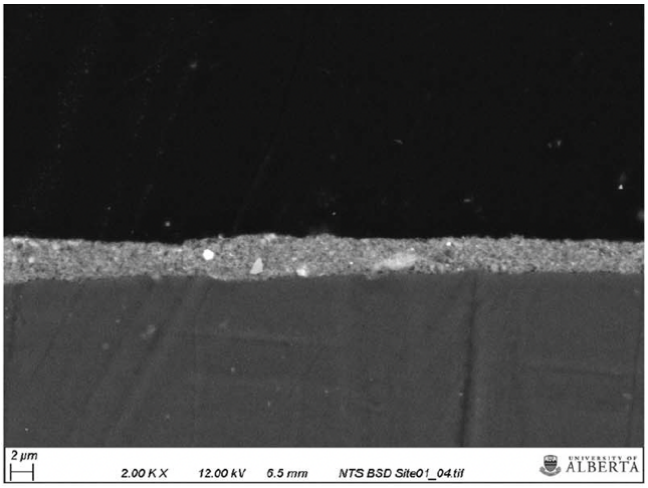

Figure 2.8: SEM CL cross-sectional image for thickness measurements (Shukla et al., 2019)

2.6.2 Energy Dispersive X-Ray Spectroscopy (EDS)

The ionomer and catalyst distribution on the CCM CL surface and cross-section affects the overall electronic and ionic conductivity of the CCM. Scott et al (2010), performed EDS mapping on an anode catalyst surface (75% $Ru_{0.7}Ir_{0.3}O_2$ and 25% Nafion). The EDS mapping for the catalyst layer surfaces showed the presence of Ru and Ir elements within deposited CL. However, fluorine mapping indicated the presence of exposed membrane areas, suggesting non-uniform CL coverage, which influenced active CCM catalyst surface area and its performance (Xu & Scott, 2010).

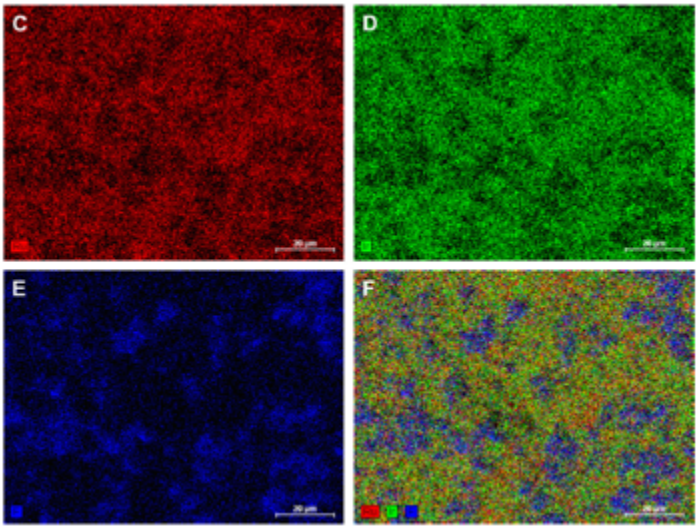

Figure 2.9: (C) Ru (Red) element EDS mapping, (D) Ir (green) element EDS mapping; (E) F (blue) element EDS mapping, (F) Ru, Ir, and F combined EDS mapping (Xu & Scott, 2010)

In a separate study Melo et al (2017), utilised STEM-EDS to map and quantify ionomer in PEMFC cathode CLs. The study involved ionomer mapping and damage quantification from both Scanning Transmission X-ray Microscope (STXM) and scanning transmission electron microscope (STEM). The mapping and damage quantification was conducted by F K-α fluorescence mapping, utilising a high-performance EDS detector in the STEM-EDS microscope. The EDS software controlled the exposure time of the electron beam at each point ranging between 2μs to 5 ms, and this resulted in an accurate EDS map acquisition duration. The maps acquired from the study are shown in Figure 2.10 below.

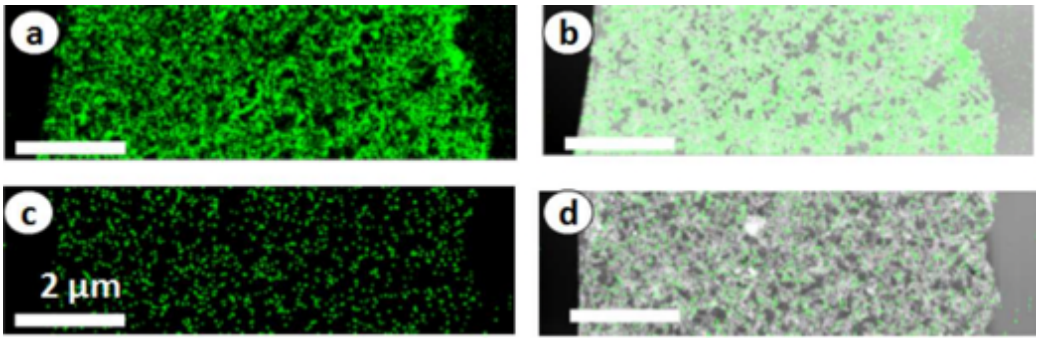

Figure 2.10: (a) and (c) are F Kα STEM-EDS single maps of fluorine in the cathode CLs. (b) and (d) are F Kα maps overlaid on high angle angular dark field (HAADF) images of the same areas (G. A. Melo et al., 2017)

The observations from the study show the STEM-EDS method produced high-quality image maps at low beam exposure and spatial resolution resulting in negligible F-loss whereas high-quality EDS maps required higher beam energy, and spatial area resulting in significant F-loss.

2.7 In situ performance testing

In-situ CCM performance testing in a single-cell electrolyser helps conclude current CCM performance and optimisation. However, literature has excessive variations in in-situ performance results due to a large variety of materials, cell or stack components, catalyst loadings, surface treatments, testing methods, and equipment frameworks (operating conditions, operating procedures, and test station configurations), which make CCM performance comparisons across laboratories

difficult (Bender et al., 2019). They conducted a round-robin test across five laboratories utilising; identical test articles, materials, test protocols, and minimum defined test station requirements (Figure 2.11). The objective of the study was to establish a straightforward method for evaluating baseline or state-of-art materials for PEMWE and validating with accurate performance comparisons (Bender et al., 2019). The polarisation curves from the in-situ testing at 60°C and 80°C cell temperatures at the five laboratories were recorded for comparison (Figure 2.12). The polarisation curves presented a general agreement in performance results from the five laboratories with a 27.0 mV maximum deviation at 60°C at 1 A.cm^2 and 20.0 mV at 80°C. These results presented a higher reproducibility between laboratories at 80°C compared to 60°C, which suggests more sensitive parameters at 60°C. The critical parameters determined were the completeness of cell conditioning and temperature control accuracy. The round-robin test results at 80°C were approximately ten times smaller in variation than the literature results, indicating an improved control of testing parameters and a more reliable CCM performance testing protocol.

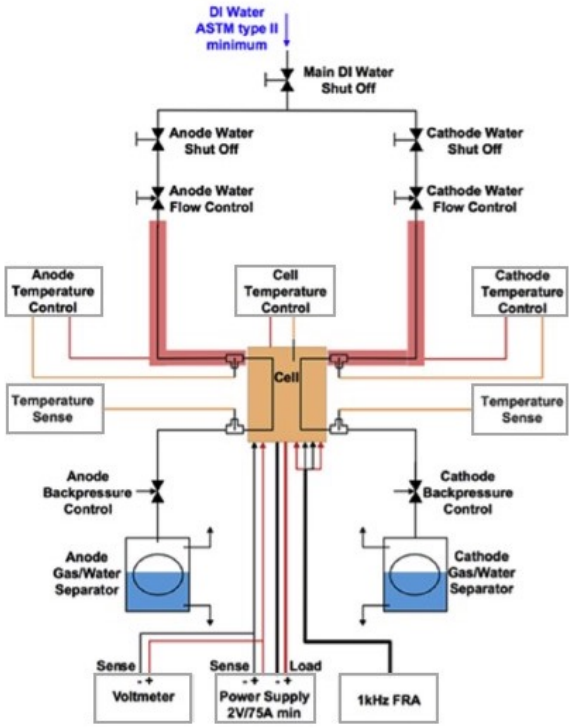

Figure 2.11: Key components required for the test station to meet minimum requirements for the round robin test procedure (Bender et al., 2019).

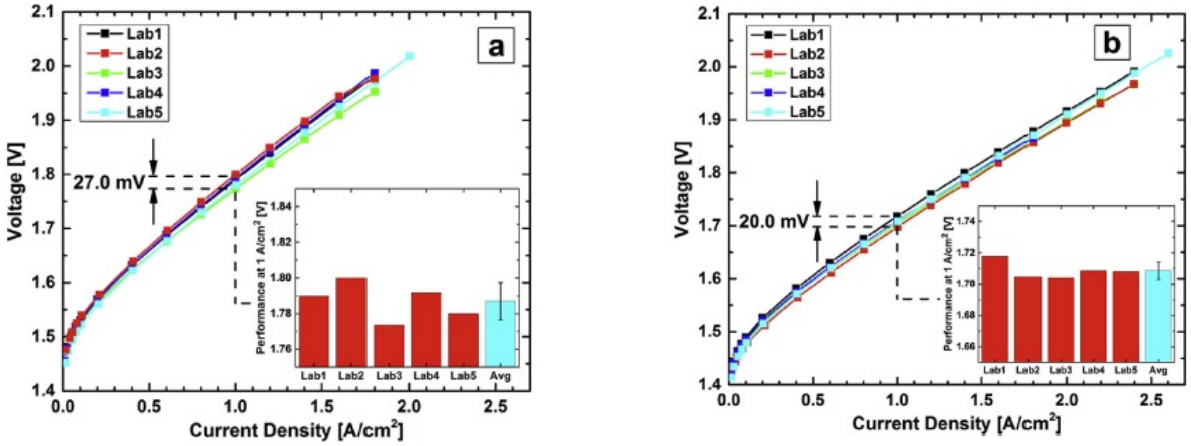

Figure 2.12: (a) Polarisation curves set at 60ºC (b) set at 80ºC, for comparison tests (Bender et al., 2019)

The overall cell voltage (E_{cell}) shown in Figure 2.12 was composed of reversible cell voltage (E_{rev}), kinetic (η_{act}), ohmic (η_{Ω}), and mass-transport (η_{mtx}) overpotentials (Equation 2.7).

Equation 2.7: Electrolyser cell voltage (E_{cell}) breakdown (Carmo & Fritz, 2013)

$$E_{cell} = E_{rev} + \eta_{act} + \eta_{\Omega} + \eta_{mtx} = E_{rev} + \eta_{act} + i.(R_{PEM} + R_{el}) + i.R_{CLa}^{H+} + \eta_{mtx-rest}$$

Reversible cell voltage (E_{rev}) is the theoretical voltage required by an electrolyser neglecting losses (Carmo & Fritz, 2013). Ohmic overpotential (η_{Ω}) losses are a sum of proton transport resistance losses in the membrane (R_{PEM}) and electron flow resistances through the current collectors and separator plates(R_{el}). Ohmic overpotential losses are determined when correcting the polarisation curve with the high-frequency resistance (HFR). Kinetic overpotential is energy loss from water electrolysis initiation, which includes the sluggish oxygen evolution reaction (OER) (Carmo & Fritz, 2013). Mass-transport overpotential occurs at higher current densities, and the causes are proton and material transport resistance in the catalyst layer. Electrochemical impedance spectroscopy (EIS) records the resistances, which include material flow restriction to the catalyst sites and gas bubbles from the active sites (Carmo & Fritz, 2013)(Babic et al., 2019b). They, conducted an overpotential breakdown when studying the anode catalyst loading effect on electrolyser performance and the magnitude orders (Figure 2.13).

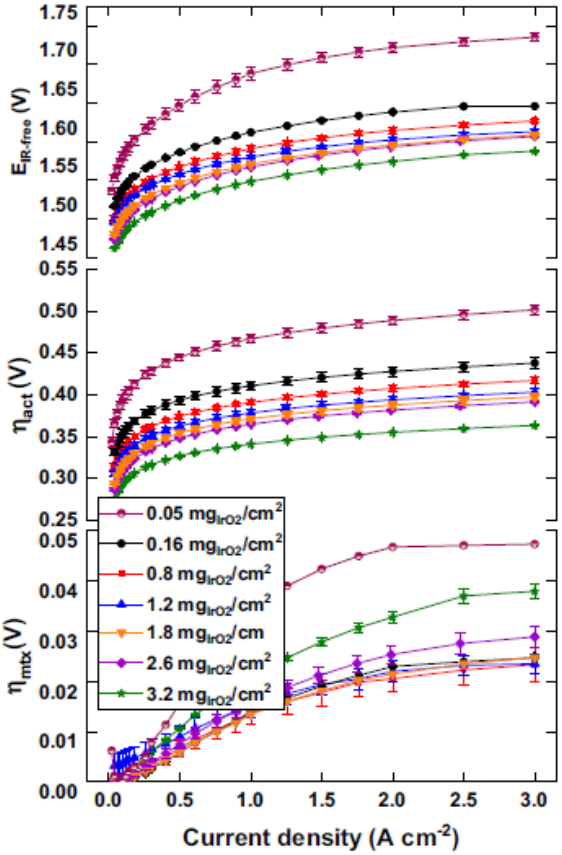

Figure 2.13: $E_{iR\text{-}free}$, η_{act} and η_{mtx} for anode loadings (IrO_2). Results were obtained by iR-correcting and polarisation curves using High Frequency Resistance (HFR) at 10kHz, 60°C cell temperature and atmospheric pressure (Babic et al., 2019b)

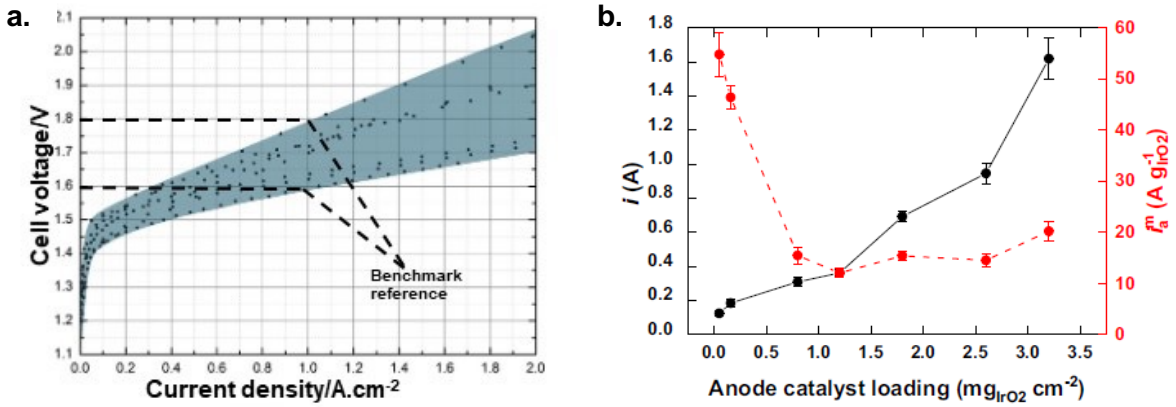

Figure 2.14: (a) PEM electrolysis single cell performance range, operating with Ir anode, Pt cathode and Nafion membrane, polarisation curves between 2010 and 2012, (b) Catalyst activity measured in current form at a fixed iR-free potential of 1.47 V (black) and the activity normalised to the IrO_2 loading (mass activity, red) (Carmo & Fritz, 2013)(Babic et al., 2019b)

Carmo et al (2013), have summarised published PEMWE results between 2010 and 2012 for CCMs with different physical properties (Figure 2.14 a). The published CCM performance show values range between 1.6 V and 1.8 V at 1 A.cm^{-2} current density (Carmo & Fritz, 2013). Babic et al (2019), conducted a different performance testing process, recording the current density, (i), at a fixed free potential ($\boldsymbol{E_{iR-free}}$) of 1.47 V. The anode catalyst loadings (CL_a) were between 0.8 and 3.2 mgIrO_2.cm^{-2}, and Figure 2.14b exhibits the recorded mass activity, $\boldsymbol{i_a^m}$, which is the current density per catalyst loading, against the anode loadings. The graph indicates the negative influence of non-homogenous catalyst layers on catalyst utilisation at high CL loadings. It is suggested that the low catalyst utilisation at higher anode loadings was caused by insufficient in- and through-plane electronic conductivity of the CL, which can be improved by optimising the CL morphology by adapting the fabrication method.

3 Experimental Methods

This section outlines the steps followed for catalyst ink formulation, catalyst layer fabrication at varied conditions, physical characterisation of anode CLs, and performance testing of CCMs.

3.1 Introduction

In this study, the ultrasonic spray coating method was applied to coat CLs. The nozzle height (NH) and speed (NS), as well as anode catalyst loading (AL) were varied. The fabrication conditions were expected to influence CCM CL microstructures, including components distribution, pore size (P_d), pore volume (P_v), and overall porosity fractions (P_O). The CLs thickness, microstructure, elemental composition and distribution were studied using scanning electron microscopy (SEM) and scanning transmission electron microscopy (STEM) in combination with energy X-ray dispersive spectroscopy (EDS). For performance testing, polarisation curves of the respective CCMs were recorded operating a 4cm^2 cell developed by Fraunhofer ISE on an electrolyser testing station from Greenlight Innovation at fixed conditions.

3.1.1 Membrane Pre-treatment and Catalyst ink formulation

To properly prepare CCMs it is essential to first follow a pre-treatment protocol for proton exchange membranes to have them at a well-defined reference state and ensure that the SO_3^- groups got acidified with an H^+ counter-ion. New membranes occasionally have a faint brown colour caused by adsorbing impurities when in contact with air (Maldonado, 2019). The pre-treatment cleaning protocol previously developed in our research group was followed in this study. Initially, eleven membrane samples (Nafion 115, 127 μm thickness, supplied by DuPont de Nemours, Inc.) were cut to 10 cm X 10 cm segment size. The membranes were then immersed in a preboiled acidic solution, composed of 50:50 vol% of 18 MΩ deionised (DI) water and 1M nitric acid, and boiled for an additional hour. Thereafter, the membranes were rinsed five times with DI water and dried for 24 hours at room temperature.

For the nozzle speed and height studies, the anode ink formulations were prepared by weighing 2.76 g IrO_2/TiO_2 (75 wt.% Ir) catalyst 1 from undisclosed supplier 1, 26.42 g of Isopropanol (IPA) from Fisher Scientific, 26.42 g DI water, and 1.61 g 20 wt% Nafion™ D2020 ionomer solution from Fuel Cell Store separately. The ionomer, IPA, and approximately half of the water volume were added in a single beaker and sonicated for 30 minutes at 25°C, 200W, and 20 kHz, in a Scientech Ultrasonic mixer (Figure 3.1a). The catalyst and the remaining water were added to a separate beaker and sonicated for 30 minutes. After sonication, the respective beaker contents were mixed and magnetically stirred at 500 rpm for 30 min in ice conditions before the catalyst ink was ready for CCM fabrication (Figure 3.1b&c).

For the anode loading study, 2.45 g IrO_x powder catalyst 2 from an undisclosed supplier 2, 1.67 g 20 wt% Nafion™ D2020 ionomer solution, 26.42 g of Isopropanol (IPA), and 26.42 g DI water were used for CI preparation. To mix and stir the ingredients for the ink preparation, a similar procedure was followed for nozzle speed and height study.

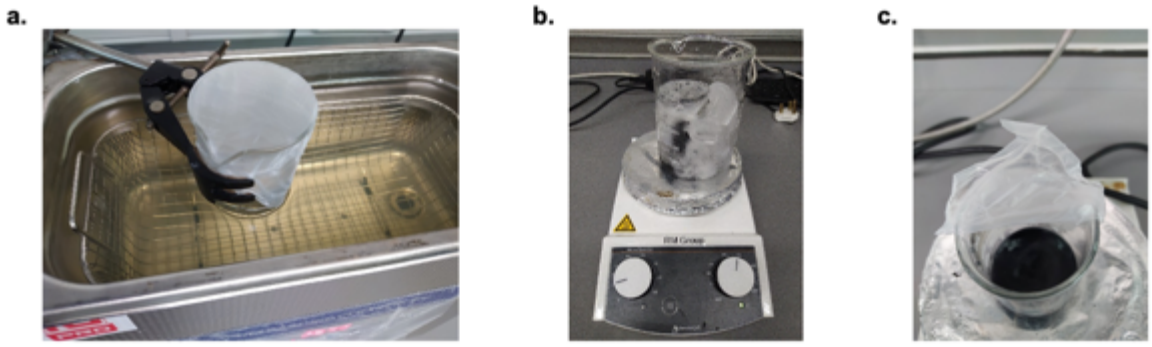

Figure 3.1: (a) Ultrasonic mixing, (b) anode catalyst ink mixing immersed in ice and (c) catalyst ink ready for ultrasonic fabrication

3.1.2 CCM preparation

The ultrasonic spraying machine (USM) PRISM Ultra-coat 300 system manufactured by Ultrasonic Systems Inc. was used to coat the anode CI on pre-treated membranes. The fabrication surface (a pre-treated membrane) was placed under a vacuum and heated to 80^{o}C to increase the evaporation rate of the solvent from the ink upon CI spraying. The heated vacuum plate also enabled the production of wrinkle-free, uniform CCMs (5 cm X 5 cm active area) (Figure 3.2a). The CI was introduced into a syringe connected to the USM and then fed to the liquid applicator (LA) at a controlled flow rate by a positive Precision Metering Pump (PMP). The CI was then dispensed in the form of a spray, as the ultrasonic vibrations from the spraying tip broke up the CI into small drops from the LA. The air director produced air streams that shaped and accelerated the ultrasonically-sprayed CI onto the membrane (Figure 3.2b).

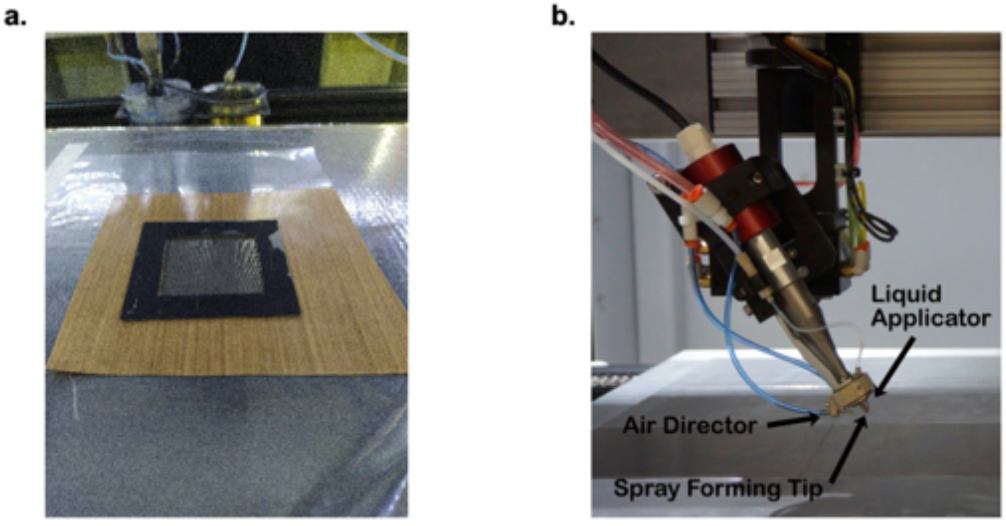

Figure 3.2: (a) Membrane under spraying mask on vacuum plate and (b) ultrasonic sprayer schematic

The ultrasonic spraying parameters such as the spraying height (NH) and the spraying speed can be varied during the coating process. The height (H) is measured as the distance between the nozzle tip and the membrane, while the spraying nozzle speed (NS) is expressed as the distance the nozzle passes in mm per second. To investigate the effect of each parameter independently, anode catalyst layers were prepared using twelve fixed spray passes.

The benchmark spraying parameters were NH = 70 mm, NS= 60 $mm.s^{-1}$, and T = 80 ^{o}C. The investigated ultrasonic spraying parameters for nozzle height were, 48 mm, 70 mm, and 100 mm, and nozzle speed of 40 $mm.s^{-1}$, 60 $mm.s^{-1}$, and 80 $mm.s^{-1}$. The coating system consisted of an X-Y-Z-Ø gantry system for motion and positioning of the nozzle head, and all the parameters were controlled on the USM platform software and control system. The nozzle motion path used for the parameter study is shown below (Figure 3.3a).

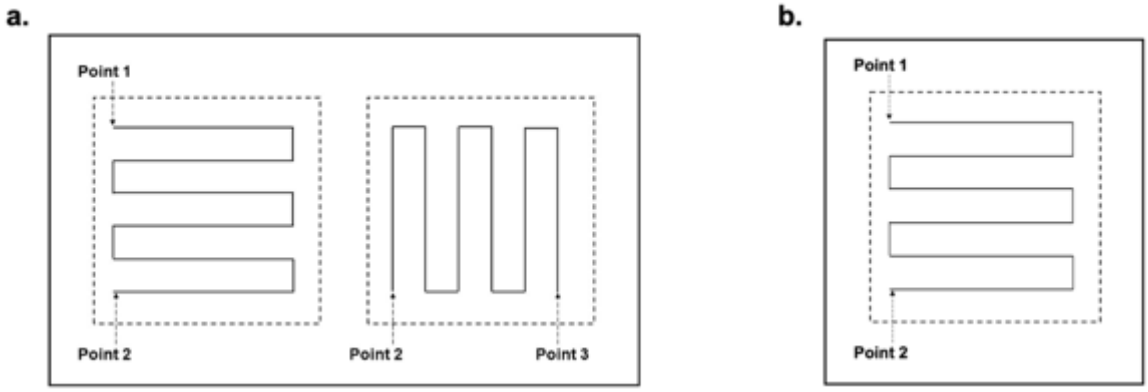

Figure 3.3: (a) Ultrasonic spraying pattern for parameter study and (b) ultrasonic spraying for catalyst loading pattern

Half CCMs (containing just the anode catalyst layer) for the anode catalyst loading study were fabricated with a target of; 0.5, 1, 2, 4, and 6 mg $Ir.cm^{-2}$ by varying the number of spraying passes. The spraying pattern followed is shown above in Figure 3.3b. After anode fabrication, each half CCM was cut into four segments of 2 cm X 2 cm. Three of the four segments were combined and aligned with a 0.5 mg $Pt.cm^{-2}$ (60% Platinum on Vulcan) on a Sigracet 22BB carbon paper commercial cathode GDE from Fuel Cells Etc store to form full CCMs. The fourth segment was left to be used for physical characterisation, thereafter, the full CCMs

were each sandwiched between five pieces of paper and one matte piece and hot pressed at 130 ^{o}C and 1 tonne.m^{-2} for two minutes. After hot-pressing, the final step was sealing the CCM between a 6 cm X 12 cm polyethylene terephthalate (PET) sheet segmented into two sections of 6 cm X 6 cm, with each side having a 4 cm^2 cut-out section in the middle. The CCM was placed between the PET sections and aligned with the cut-out 4 cm^2 section, and sealed at 100^{o}C and 1 tonne.m^{-2}. The hot-pressing and sealing procedures were repeated for all eleven samples before they were ready for performance testing.

3.1.3 Commercial CCM

A commercial CCM from an undisclosed supplier 3 with an anode loading of 2 mg Ir .cm^{-2} was used to benchmark the performance of the ultrasonic sprayed CCMs with a comparable loading from the study. The commercial manufacturer reported the anode fabrication method as screen printing.

3.2 Characterisation methods

3.2.1 Scanning Electron Microscopy (SEM)

Scanning Electron Microscopy (SEM) physical characterisation is essential for understanding the CCM microstructure. SEM produces images by scanning the surface of a sample with an electron beam in a rasterring pattern. The electrons that form the electron beam are emitted from an electron gun which typically utilises a thin tungsten filament (~ 0.1mm). When the filament is heated to a high temperature of approximately 2800K, it emits electrons which get attracted to the positively charged (1 to 30kV) metallic anode (Weiss, 1983). The anode has a central hole with a diameter of 15 – 20 μm from which the electron beam flows through and is then further guided by the system of magnetic lenses to the sample. The sample is stationed in the SEM chamber under a vacuum (≈ 1 x 10^{-5} mbar) (Figure 3.4a).

When the electron beam lands on the conductive sample, it penetrates it creating the interaction volume of 100 nm to approximately 5 μm depending on the beam energy. From this region, several types of signals are emitted and used for image formation and elemental analysis. These are secondary electrons (SEs), back-scattered electrons (BSEs), auger electrons, transmitted electrons, characteristic X-rays, cathodoluminescence, and continuum X-rays (Figure 3.4b). SEs are a result of

inelastic interactions between the beam electrons and sample atoms, where valence electrons of the sample atoms are emitted and referred to as SEs. These SEs have low energy, below 50 eV, and only those produced from near-surface sample atoms (a few nanometres deep), are detected while those generated deeper within the sample are re-absorbed. Therefore, SEs primarily provide information on sample surface topography and are commonly detected by the Everhart-Thornley detector (ETD), a collector-scintillator-photomultiplier system located in the SEM at an angle to the sample (Everhart & Thornley, 1960).

For detection, SEs get attracted by a positively charged electrical grid at about +400V and further accelerated towards the scintillator at about +2 000V. The accelerated SEs cause the scintillator to emit light flashes to the photomultiplier outside the SEM column. The amplified electrical signal is then converted from analogue to digital producing a digital image. Images produced from SEs show a contrast difference due to the surface morphology, where edges of elevated sample features appear brighter, capturing the well-defined three-dimensional structure.

BSEs have higher energy and originate from elastic interactions between the electron beam and deeper sample atoms. The elastic interactions are when the electrons are back-scattered or reflected out of the sample interaction volume. The BSEs have an energy range between 50eV and the beam energy (up to 30kV), and atoms with a higher atomic number (Z) reflect the incident electrons more compared to those with a lower atomic number. Therefore, SEM images that are produced by the detection of BSEs show contrast difference that is dependent on sample composition. Regions containing heavier elements appear brighter compared to those containing lighter elements. These images, therefore, provide qualitative information such as the understanding of the high Z vs. low Z elemental distribution within the sample. For maximising BSEs collection, the backscatter detector is positioned directly above the sample and concentric with the beam.

If the studied sample is partially-conductive, a charging effect occurs as the incident electron beam on the sample causes an accumulation of negative charge because the electron beam current is higher than the sum of the outgoing secondary and backscatter currents. This effect creates a repulsive force causing the electron beam

to be deflected which produces distorted images (Weiss, 1983). The charging effect can be reduced by carbon coating the sample during sample preparation which will be described further in the method development section. Characteristic X-rays get formed when the electrons in the inner shells of a sample's atoms get emitted from the irradiation of the beam electrons. The vacant shells then get filled with the outer-shell electrons, and simultaneously characteristic X-rays corresponding to the energy difference are emitted. They are referred to as characteristic X-rays because their wavelengths correspond to the difference in energy between the higher energy shell and lower energy shell for distinct elements. Analysis of these X-rays provides information on sample elemental composition and element distribution. Other signals emitted from the sample such as Cathodoluminescence, is an optical and electromagnetic process in which the beam electrons excite the sample atoms causing them to emit photons with wavelengths in the visible spectrum as they return to their ground state, have low significance in this study.

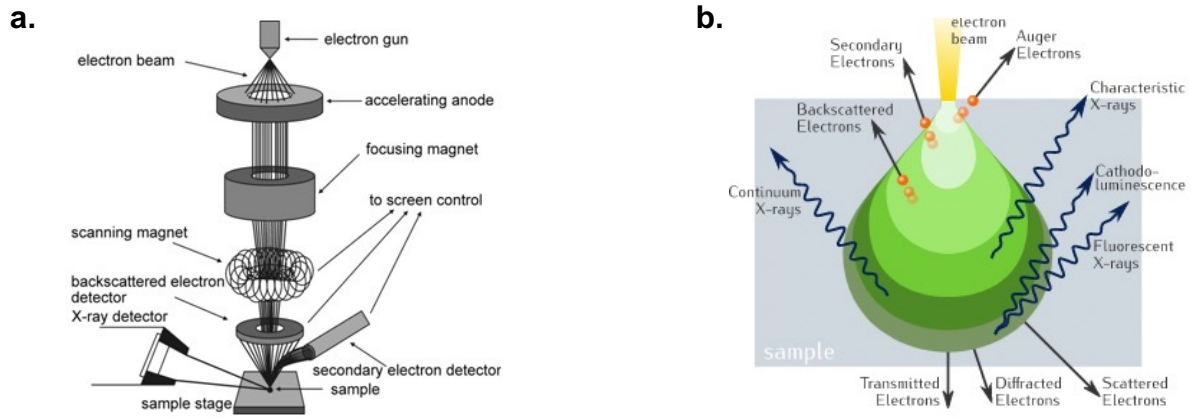

Figure 3.4: (a) SEM imaging equipment schematic , (b) Signals emitted from electron beam-sample interaction volume (Havancsak, 2019)

For this study, the FEI NovaNano 230 SEM was used (Figure 3.5 a&b). Images using secondary electrons detected by the ETD were used to study the CCM surface morphology and evaluate catalyst dispersion/coverage on the membrane. The images recorded in a BSEs mode were used for the CL cross-sectional analysis, (i.e. observation of delamination of CL from the membrane and cracking), CL thickness measurement, and EDS analysis. The beam conditions for surface imaging were a landing energy of 20.0 keV and a spot size of 4.0. For each sample, images were captured at different magnifications, 500X, 1 000X, 5 000X, and 20 000X for both

surface and cross-sectional analysis. For the measurement of CL thickness, five BSE images were captured at 5 000X magnification for each sample at random locations.

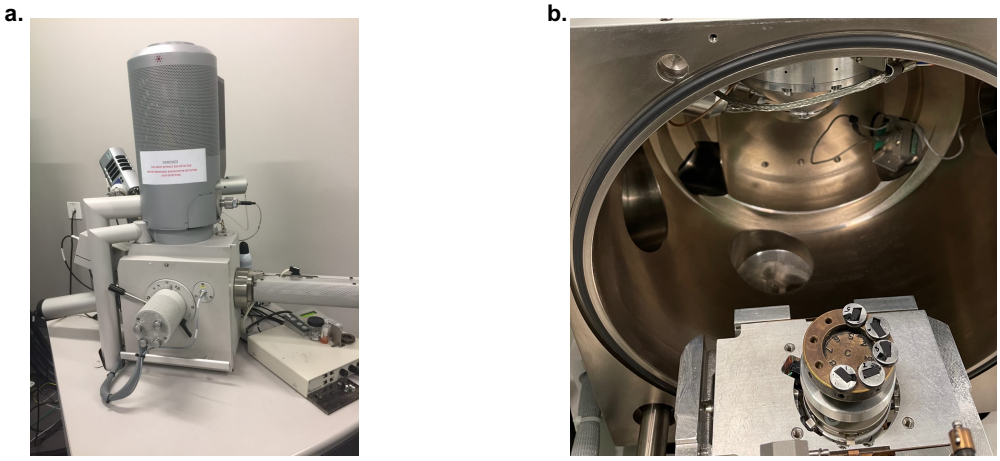

Figure 3.5: (a) FEI NovaNano 230 SEM, (b) mounted CCM surface samples.

3.2.2 Energy Dispersive X-Ray Spectroscopy (EDS)

EDS is an analytical technique utilised in microscopy for elemental analysis. As explained in Section 3.2.1, the characteristic X-rays emitted during the electron beam and sample interaction corresponds to the orbital structure of a distinct element. This technique is non-destructive and it enables a quick, and effective analysis of the sample's elemental composition. In commercial instruments silicon drift detectors (SDD) are used for X-ray detection. Emitted X-rays enter the semiconductor detector where electron-hole pairs are generated corresponding to X-ray energies. An example of an EDS spectrum is shown in Figure 3.6a (Efremenko et al., 2020). The EDS can determine the presence of chemical elements and quantify their relative abundance, providing that for each element, a standard material is measured as well. However, a standardless approach is typically applied in modern systems, where the quantification is enabled via software which applies various correction factors. EDS has several analysis modes: point analysis, where a spectrum is obtained from a point irradiated by the electron beam, line analysis, determines the elemental distribution across a specified line, area analysis, where the signal is averaged from the selected area of interest and mapping, where the elemental distribution is mapped from a defined 2-dimensional area.

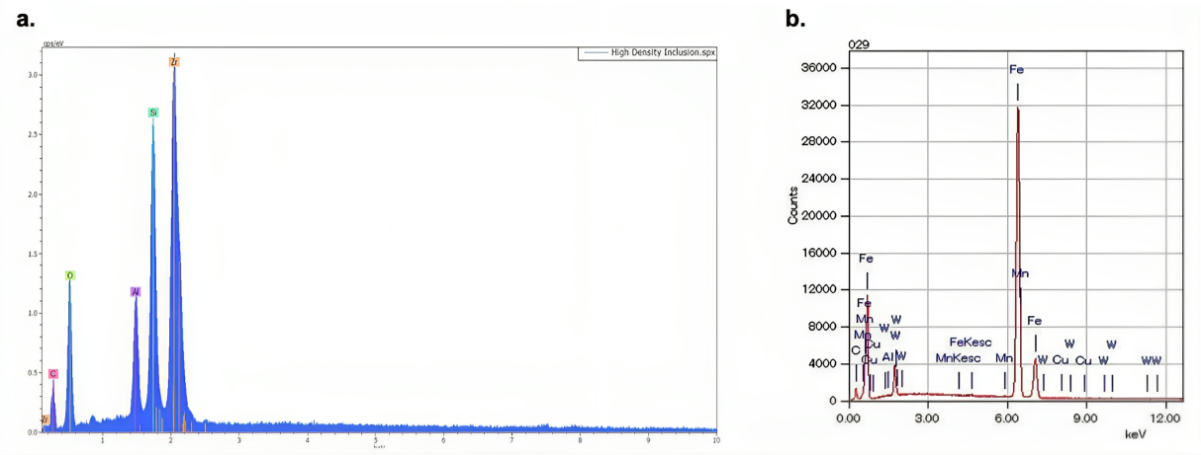

Figure 3.6: EDS spectrum (Efremenko et al., 2020)(Advanced MicroAnalytical, 2021)

In this work, EDS area analysis was used to obtain elemental maps for Ir, O and F distributions in various CLs.

3.2.3 Scanning Transmission Electron Microscopy (STEM)

For selected samples, the microstructure and composition were also evaluated by scanning transmission electron microscopy with energy dispersive spectroscopy (STEM-EDS). This technique was selected due to its ability to produce high-resolution images of CLs using high angle annular dark field (HAADF) detector (Thermo Fisher Scientific, 2021) (Ponce, Mejía-rosales & José-yacamán, 2012). Ultramicrotomy was used to prepare samples for STEM imaging and EDS mapping. A small piece of the catalyst-coated membrane was cut and embedded in a 1:1 mixture of trimethylolpropane triglycidyl ether resin (Sigma-Aldrich, USA) and 4,4′-Methylenebis (2-methylcyclohexylamine, Sigma-Aldrich, USA) hardener. The embedded sample blocks were left in an oven overnight to polymerize at 60°C. Ultramicrotome thin sections (approximately 100 nm) were cut by Leica UCT ultramicrotome setup (Germany) equipped with an Ultra 45°DiATOME knife, USA. The sections were then placed onto 200 mesh Cu grids. To obtain information on catalyst layer microstructure and distribution of elements, a Talos F200X scanning transmission electron microscope (STEM, Thermo Fisher Scientific, USA) equipped with Super-X four silicon drift detectors of energy dispersive spectrometry (Super-X SSD EDS, EDAX, USA) at a solid angle of 0.9 steradians with electron accelerating voltage of 200 kV was utilised. Super-X detectors enabled the collection of EDS maps from selected CL areas within minutes. The distribution of iridium,

titanium, fluorine, and oxygen was mapped, and color composite images were created to aid the understanding of the CL structures and component distributions.

3.3 CCM Performance testing

The in-situ CCM electrolyser performance testing procedure outlined by Bender et al (2019), was followed in this study. CCMs were placed in a Fraunhofer ISE cell (Figure 3.7 a) that was connected to a Greenlight Innovation electrolyser test station (Bender et al., 2019). The cell hardware featured a single-cell design with thick endplates for compression, gold-plated copper current collectors, and flow fields with distributed inlet and outlet flow. Both cathode and anode flow fields had platinum/gold-plated titanium and platinum coatings. The overall flow field dimensions were 50 mm X 50 mm with an active area of 20 mm X 20 mm. The CCM performance testing procedure recorded polarisation curves for each CCM for comparison. The testing process involved preconditioning each CCM by washing it in 0.1 M H_2SO_4 for 1 hour and rinsing it in deionised water for at least 2 hours, ensuring the removal of sulphate radicals on the CL surface and hydrating the CCM. The CCM was then sandwiched between two Ti PTLs and assembled at 1 kN torque to prevent water from leaking from the cell (Figure 3.7 b). After cell assembly, DI water was circulated through the cell from the anode at 0.1 $L.min^{-1}$ flowrate and 60^{o}C and monitored by thermocouples inserted in the current collectors. For activation, a stable current density of 0.2 $A.cm^{-2}$ was applied to the cell for 30 minutes and subsequently increased to 1.0 $A.cm^{-2}$ for 30 minutes. The cell voltage was held at 1.7 V for at least 2 hours until the cell current variation decreased to under 1% per hour. Performance curves were then recorded at 5-minute steps starting from the open-circuit voltage (OCV). The current density was increased by 20 $mA.cm^{-2}$ increments up to 100 $mA.cm^{-2}$, then 200 $mA.cm^{-2}$ increments until a maximum cell voltage of 2.0V was reached. The process was reversed following the same current density step intervals and, the open-circuit voltage (OCV) was recorded after the last decrement. Unfortunately, due to equipment constraints, no EIS measurements were conducted. Therefore, for performance comparison, only the overall polarisation curve data was analysed and the results discussed in relation to the CCM microstructure and physical characterisation. As a convention, the CCM performance was compared by the overall cell voltage required to reach 1 $A.cm^{-2}$, where lower cell voltages indicated better overall CCM performance.

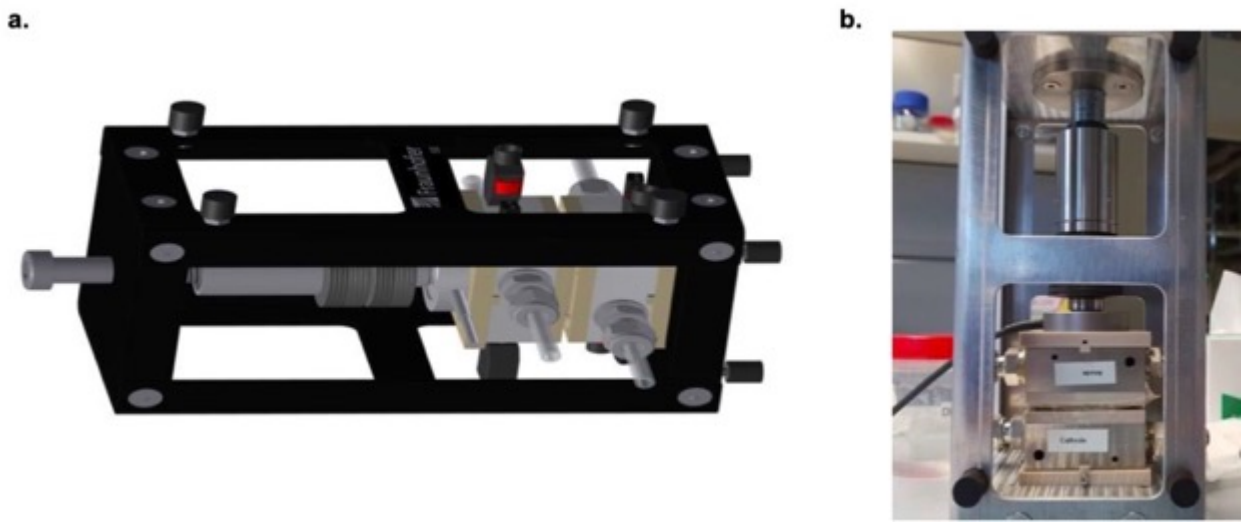

Figure 3.7: (a) Fraunhofer PEM cell schematic, (b) cell assembled in study (anode on top and the cathode on the bottom)

4 Catalyst Layer Thickness Measurement - Method Development

This Chapter explains the method developed to enable reliable and statistically relevant measurement of the CCM catalyst layer thickness. The method consists of sample preparation (epoxy embedding), polishing, imaging and image analysis.

4.1 Catalyst layer embedding in Epofix

The CCM sample preparation for cross-sectional analysis and catalyst layer thickness measurement is essential to ensure stable and charge-free image capturing. For this study, two approaches were considered to cross-section the CCM. These were: (1) cutting the CCM with a razor blade and placing it in a specially prepared aluminium foil holder for imaging and (2) embedding the pre-cut CCMs in epoxy followed by polishing (epoxy method). A fresh razor blade was used for each CCM to get as clean as possible a CL cross-section cut, avoiding CL damaging or membrane smearing. The razor blade method is fast, but it has drawbacks due to the sample, bending, and curling in a holder, which prevents proper imaging of CL cross-section and makes it difficult to perform an EDS analysis. It also results in increased charging and occasionally CL detachment from the membrane as shown in Figure 4.1a.

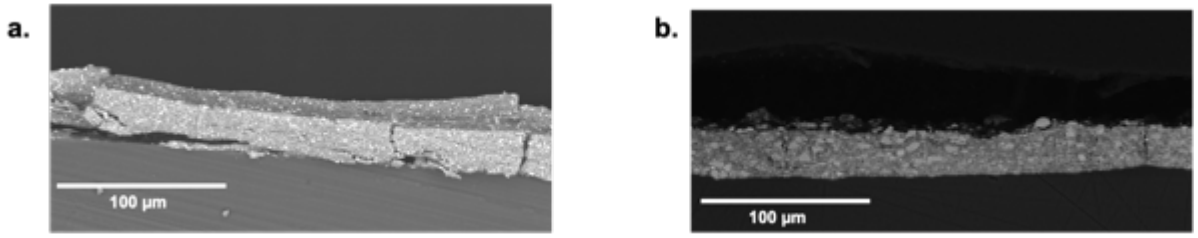

Figure 4.1:(a) CCM prepared by razor blade method and (b) CCM cross-section prepared by epoxy method.

Therefore, an epoxy method was developed and adopted in this study, to enable the examination of larger CCM cross-sectional areas, the generation of images for catalyst layer thickness measurement, and more precise EDX compositional analysis. For this work, Epofix (Struers) epoxy was used. It is a cold-setting resin composed of two fluid epoxy components, a resin, and a hardener. Embedding the CCMs is effective because Epofix polymerises at room temperature which limits polymerisation damage and preserves physical structures of irregularly shaped porous specimens (Luft, John (University of Washington, 1961). This is achieved by the specimen having a low shrinkage and high mechanical stability in the cured state. The components required for the CCM embedding were half CCMs (anodes), polyvinyl acetate (PA), gas diffusion layers (GDLs), resin, hardener, disposable plastic cups, wooden spatulas, and specimen holders. The CCMs, PAs, and GDLs were cut into segments of approximately 2 cm^2 and stacked together in alternating order. Each CCM was sandwiched by a GDL and PA in the order shown in Figure 4.2a (partial stack). The stack of CCM cuts was held together by the plastic holders as shown in Figure 4.2b (full stack with 5 CCMs). Sandwiching the CCMs with GDL is beneficial as it reduces the charging during the imaging. Separating each GDL/CCM/GDL structure with a PA assisted in locating and distinguishing the respective CL under SEM since contrast differences between PA and CL were easily recognisable. To aid CCM recognition, stacking order was established in such a way that the first CCM would be placed next to double PA layers, followed by a PA layer and a second CCM, etc. Typically, two stacks each containing two to three CCM samples were placed in a Vaseline-lubricated plastic mold for subsequent epoxy addition (Figure 4.2c).

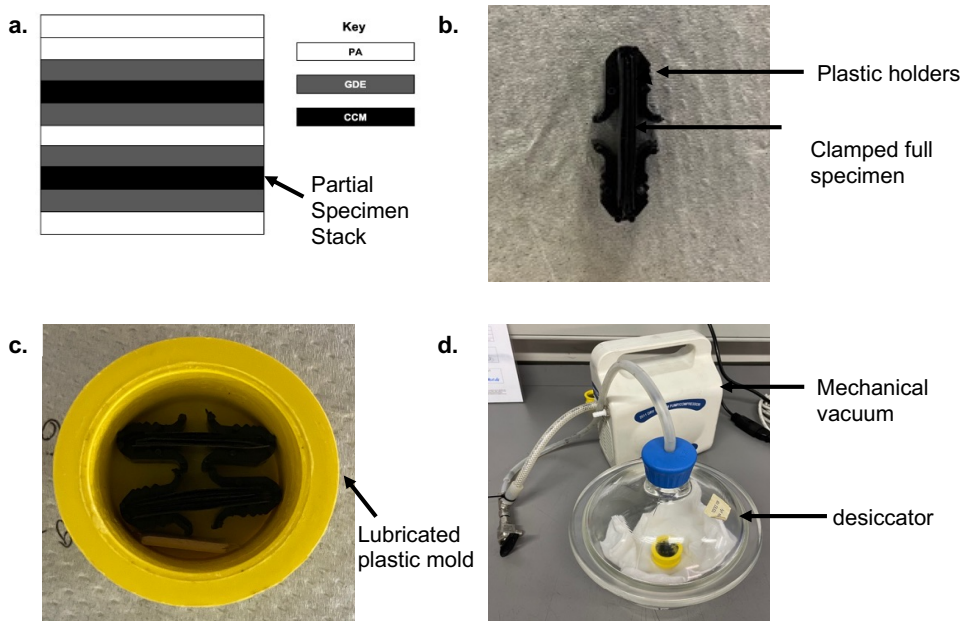

Figure 4.2: (a) Schematic of a partial specimen stack and (b) a full specimen stack clamped with the plastic holders, (c) two full specimens placed in a Vaseline lubricated plastic mold, (d) the mold placed in the desiccator connected to a mechanical vacuum pump

An Epofix mixture for immersing the CCM stack was made by following the supplier-suggested recipe of mixing approximately 15 parts of resin with 2 parts of hardener by volume. The mixture was stirred smoothly and thoroughly with a wooden spatula to minimise bubbles formation and carefully poured over the CCM stack. To ensure full epoxy penetration in the CCM stack and to remove the air bubbles formed during the stirring and pouring of epoxy, molds were placed in a desiccator connected to the mechanical vacuum pump (Figure 4.2d). The desiccator was then evacuated to vacuum levels of ~ 1 x 10^{-3} mbar 3-4 times for 2-minute intervals to promote epoxy penetration into the CCM stack and to extract air bubbles. Bubble removal is necessary to limit their negative effect on epoxy penetration into the samples, which would distort SEM characterization. Subsequently, the samples were left in a fume hood to cure at room temperature for 24 hours. The following step involved polishing using a Struer Tegramin machine (Figure 4.3a) To reach a satisfactory polishing finish, the polishing recipe was developed to include four different sized silicon carbide abrasive grinding paper of: 25.8 microns, 15.3 microns, 6.5 microns, and 2.5 microns. After the polishing process, the epoxy pucks were dried overnight after which their surfaces were carbon-coated with a Balzers PV935 carbon coater module. The carbon coating deposits a thin (~ 10-30 nm) conductive carbon layer on the puck's surface,

which makes it conductive and prevents sample charging and beam damage during SEM imaging. The carbon coating process involved placing the epoxy puck in a chamber under a vacuum (1 X 10^{-4} mbar) which had a carbon rod mounted between two high-current electrical terminals. When the carbon rod got heated and reached its evaporation temperature, a fine carbon stream was deposited on the epoxy puck (Figure 4.3b)

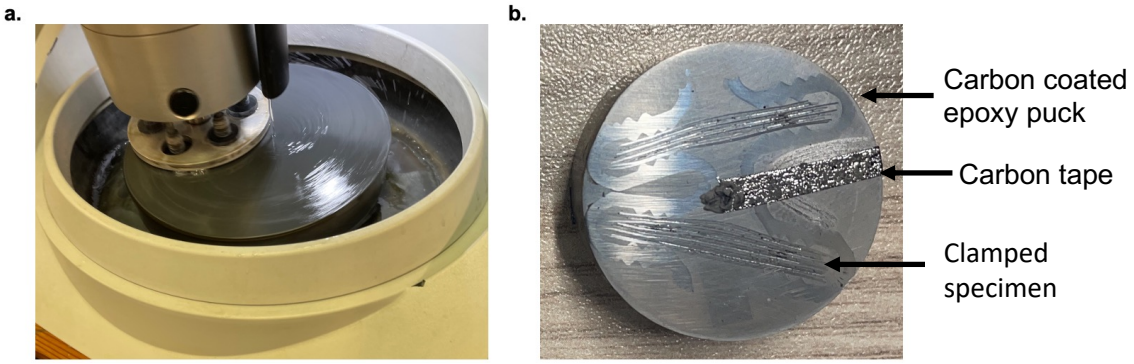

Figure 4.3: (a) Epoxy puck polishing and (b) carbon coated epoxy puck ready for SEM characterisation

After carbon coating, the pucks were placed in an SEM and CCM CLs were imaged in back-scattered mode. Typical imaging conditions were discussed in Chapter 3.

4.2 Image analysis

The analysis of catalyst layer (CL) thickness involved the utilization of the image processing software, Image J, to process scanning electron microscope (SEM) images captured at 5,000x magnification. To ensure comprehensive representation of the CL cross-section, five distinct images were systematically selected from diverse CL locations for each sample. Each image was uploaded into ImageJ, and a pixel/mm scale was set and recorded using the analyser tool. After recording the scale, the image was cropped to reduce the background pixels and then re-opened with a Trainable Weka Segmentation Plugin provided by ImageJ software. The plugin enabled training a classifier to separate CL pixels from the background (epoxy and GDL) and membrane pixels (Figure 4.4 a&b). The classifier training involved annotating the CL and background pixels and repeating the process until it could accurately classify the differences.

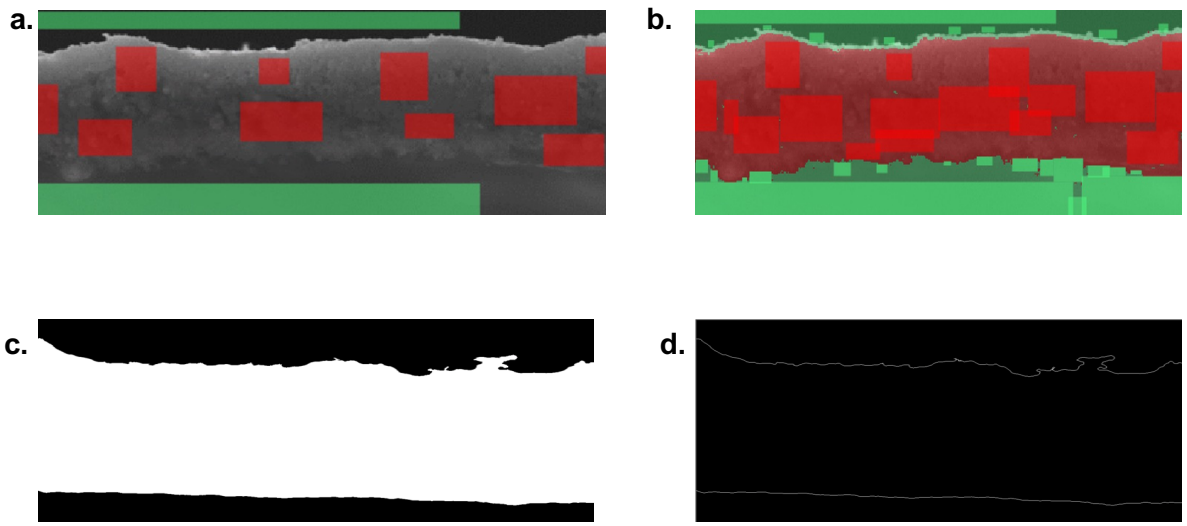

Figure 4.4: (a) Annotating the CL (red) and background (green) pixels, (b) classified CL and background, (c) classified CL binary and (d) CL skeleton

Figure 4.4b was then binarised to black (background) and white (CL) (Figure 4.4c) and then skeletonized to distinguish the CL edges (Figure 4.4d). The CL edges had corresponding X and Y coordinates which were saved and exported to excel. These X and Y coordinates were recorded at each point along the bottom and top, CL edges were plotted on a graph and gave a detailed CL representation. Differences in Y-coordinate pixel values were subsequently converted into precise CL thickness measurements, employing the pixel/µm scale, with the computation of a standard deviation for data assessment. The procedure was repeated for all studied samples.

5 Results and Discussion

This chapter summarises the results of the effect of the ultrasonic spraying method coating parameters and Ir loading on the nature and performance of electrolyser CCMs. The ultrasonic sprayer nozzle height and speed were varied in this study. CCM physical characterisation and performance results are summarised. A comparison was made against the commercial MEA for those CCMS with equivalent Ir loadings.

The naming convention for the samples studied throughout this chapter for the nozzle height, speed and anode loadings is outlined in Table 5.1 below.

Table 5.1: Naming convention for the nozzle height and speed study samples

Sample name	**Abbreviation**	**Spraying Height, H (mm)**	**Spraying Speed, S ($mm.s^{-1}$)**
Nozzle height 1 & Nozzle speed 2	NH1 / NS2	48	60
Nozzle height 2	NH2	70	60
Nozzle height 3	NH3	100	60
Nozzle speed 1	NS1	48	40
Nozzle speed 3	NS3	48	80

5.1 Nozzle height and speed study

The influence of the nozzle height and speed on the CCM anode microstructure and overall electrolyser performance was conducted by preparing 5 CCMs with 0.5 mg Pt/cm^2 (60% Platinum on Vulcan) on commercial carbon paper (Sigracet 22BB) cathode GDEs from Fuel Cells Etc, Nafion 115 membranes, and anode CLs of IrO_2/TiO_2 (75 wt% Ir) catalyst from undisclosed supplier 1. Fabrication of the anodes for the nozzle height study samples was conducted at 48mm, 70mm, and 100mm (NH1, NH2, NH3) at a fixed nozzle speed of 60 $mm.s^{-1}$ forming full CCMs. For the nozzle speed study, the CCMs were sprayed at 40 $mm.s^{-1}$, 60 $mm.s^{-1}$, and 80 $mm.s^{-1}$ (NS1, NS2, NS3) at a fixed nozzle height of 48 mm. The spraying nozzle conditions for samples NH1 and NS2 were the same therefore sample NH1 fabricated from the height study was referenced as NS2 and the CCM was referred to as NH1/NS2. The full CCMs were then physically characterised utilising SEM, EDS, STEM, and single-cell electrolyser polarisation curves to evaluate the overall performance. Initially for physical characterisation the anode surface morphologies of the CCMs were examined using SEM to evaluate surface uniformity, the presence of cracks, and observe catalyst agglomerate sizes. The results obtained are shown in Figure 5.1 and Figure 5.2 below.

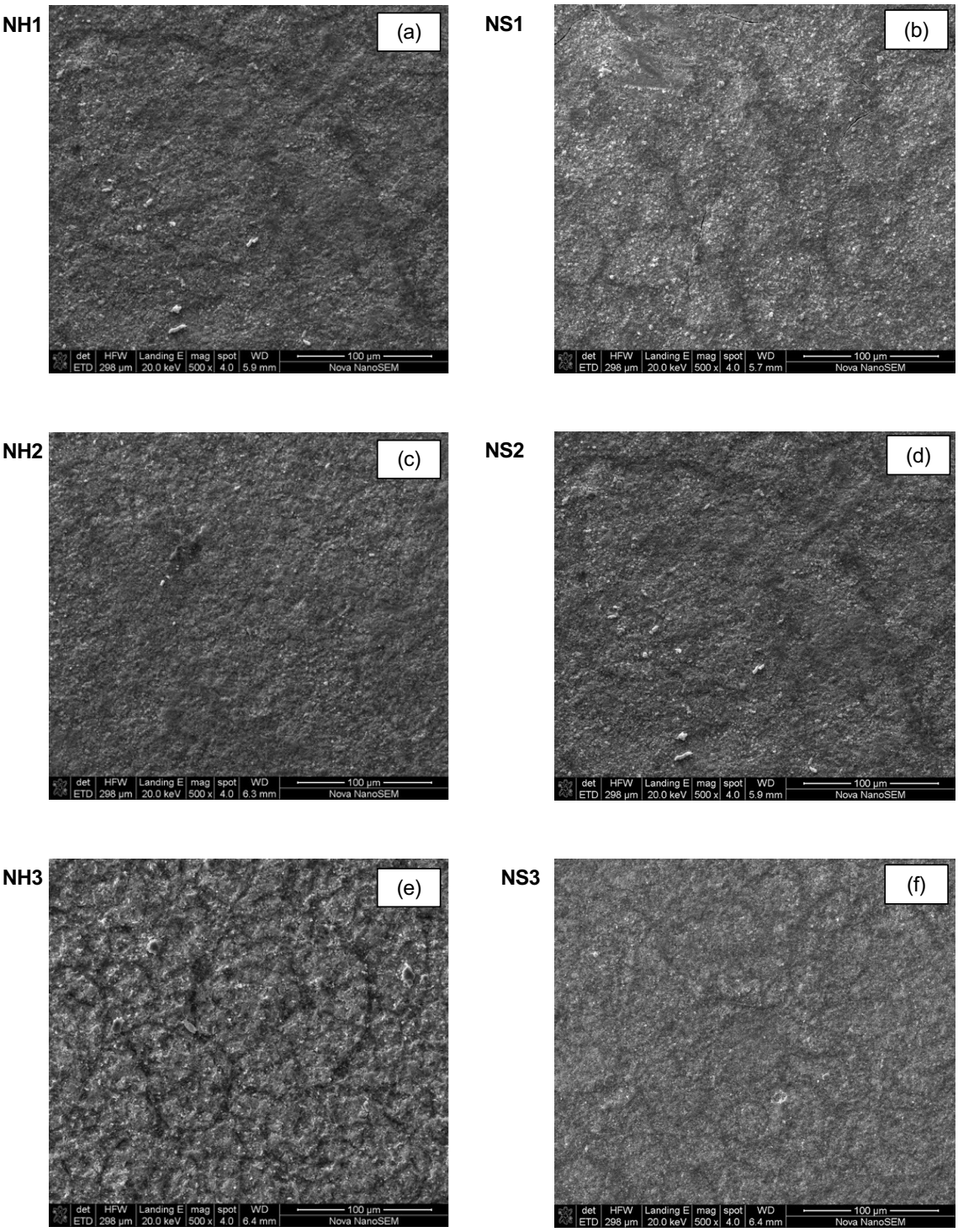

Figure 5.1: SEM low magnification (X500) surface images of nozzle height study anode CLs (a,c,e), and (b,d,f) for the nozzle speed CLs

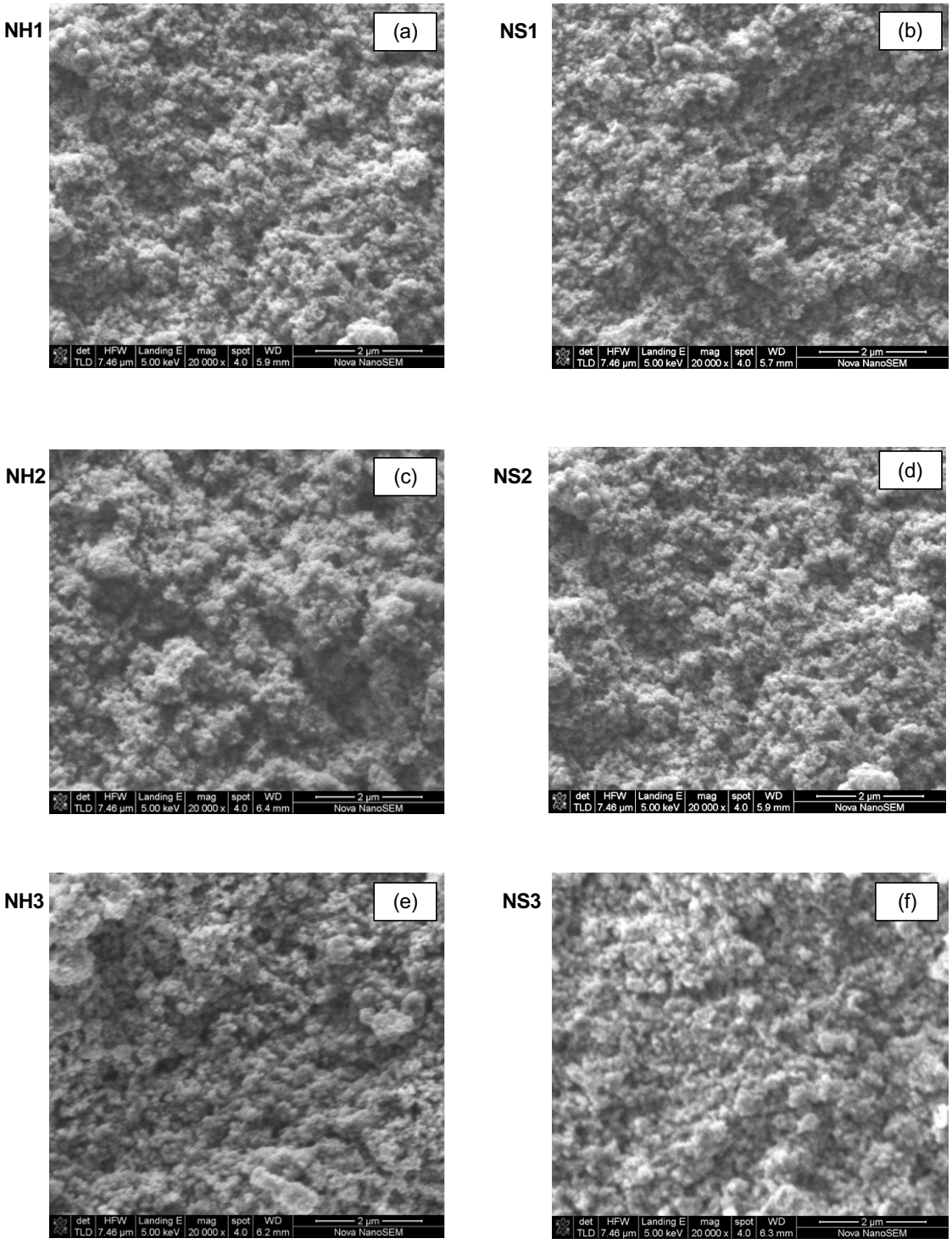

Figure 5.2: SEM high magnification (X20 000) surface images of the nozzle height study samples (a,c,e) and (b,d,f) for the nozzle speed surface images

From the low-magnification surface images obtained from SEM, there appears to be no visible difference between the CLs from the nozzle height and speed studies. The surfaces at low magnification, show high-quality crack-free coatings, where full catalyst coverage of the membranes was achieved. At higher magnification, the CL

surface morphology for all samples appears homogenous and the catalyst agglomerates appear laterally well interconnected, which potentially indicates uniform ionomer dispersion within each of the CLs. This observation is ideal for the formation of triple-phase boundaries and could have a positive effect on reducing through-plane proton transport resistance in agreement with observations and results obtained by Babic et al (2019), in their respective study on the effect of anode catalyst loading on proton transportation in the CL.

Cross section images

Cross-sectional imaging of the anode CL is effective for analysing CL cracks, overall morphology and for measuring the CL thickness from the imaged region. The images for the study were obtained at a lower magnification (X5 000) to obtain a wider coverage of the CL, which enhances the evaluation of the presence of cracks, connectivity within the membrane, and thickness uniformity. The higher magnification (X10 000) cross-section images recorded outlined the catalyst agglomerate formation and CL overall morphology. Figure 5.3 cross sections and Figure 5.4 shows a higher magnification of sample NS1 which has the highest loading amongst the studied samples.

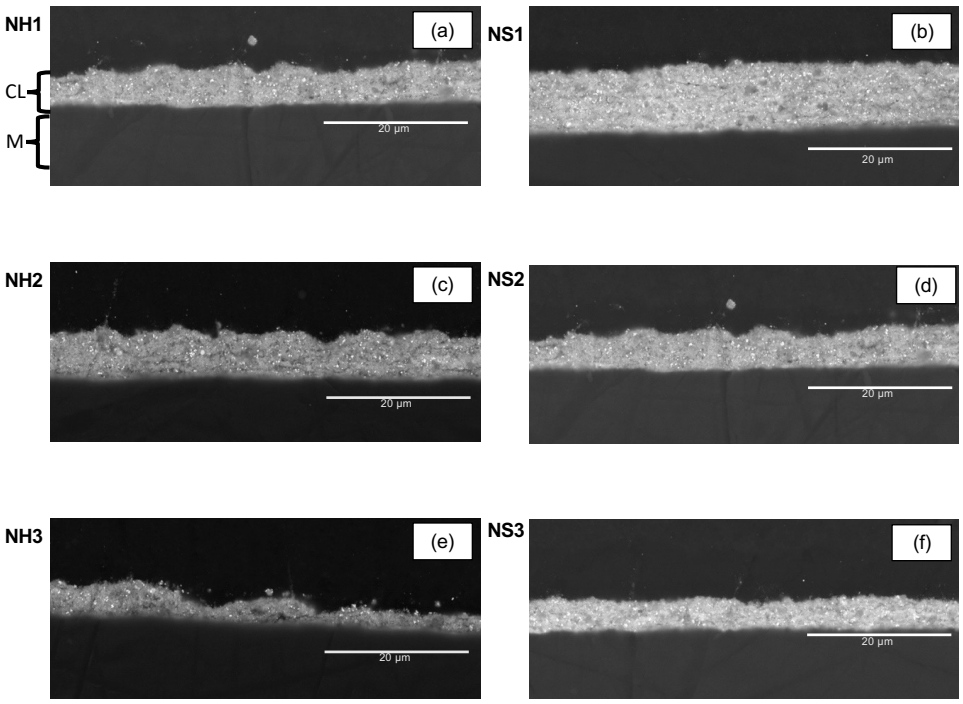

Figure 5.3: Cross section SEM images of the nozzle height study samples (a,c,e) and (b,d,f) for the nozzle speed study samples at a X5 000 magnification using the SEM backscatter detector

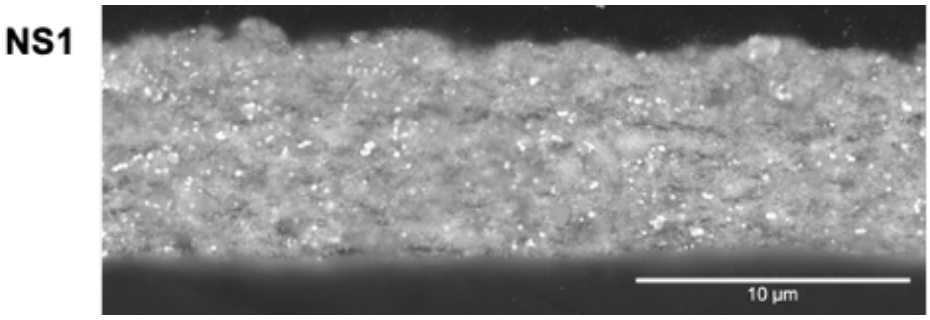

Figure 5.4: A higher magnification (X10 000) cross section image of NS1 from the SEM backscatter detector

The low CL magnification cross-section images at different nozzle heights and speeds suggest no cracks in the CL. Figure 5.3a shows the labelled segmentation of the catalyst layer and membrane which can be inferred for the other samples. The presence of very bright uniformly distributed particles was observed through all CLs. The SEM images of the CLs at the different nozzle heights and speeds show full adhesion of the CLs to the membranes, with no tearing or delamination observed, which is required for low ohmic losses and good CCM performance. The higher magnification of sample NS1 with the highest catalyst loading Figure 5.4, provides more insight into a CL morphology, showing a dense CL with regions of distinct contrast difference.

The overall CL agglomerates are laterally interconnected which could decrease the negative effect of in-plane proton transport resistance on the CCM overall performance as observed by Gasteiger et al (2016), in their study for understanding the influence of ionomer content in IrO_2/TiO_2 electrodes on PEMWE performance. Evenly distributed high-contrast particles approximately 0.05 μm in diameter indicate that their composition is different from the rest of the CL. In back-scattering imaging mode, high contrast is achieved from material regions containing high atomic number elements. Considering that CLs were made using Ir, Ti, and O containing catalyst, it can be speculated that the high contrast particles contain the element with the highest atomic number which is Ir. Overall, no significant visual change in CL microstructure can be observed in the cross-section images from changes in the nozzle height and speed.

Catalyst layer thickness and loading: influence of nozzle height and speed

Table 5.2 plots the correlation graphs of the anode thickness and loading versus nozzle spraying height and speed. The anode catalyst loading and thickness for each CCM were determined following the procedures described in Chapter 3.1.2 and 4.2.

Table 5.2: The CL loadings and cross section thicknesses, for the nozzle height and speed study samples

Sample	Nozzle Height (mm)	Nozzle Speed ($mm.s^{-1}$)	Ir loading ($mg.cm^{-2}$)	CL Thickness (µm)
NH1	48	60	1.87	4.4 ± 1.1
NH2	70	60	1.61	5.7 ± 1.0
NH3	100	60	1.27	3.1 ± 1.2
NS1	48	40	2.84	8.5 ± 1.0
NS2	48	60	1.87	4.5 ± 1.1
NS3	48	80	1.42	5.5 ± 0.5

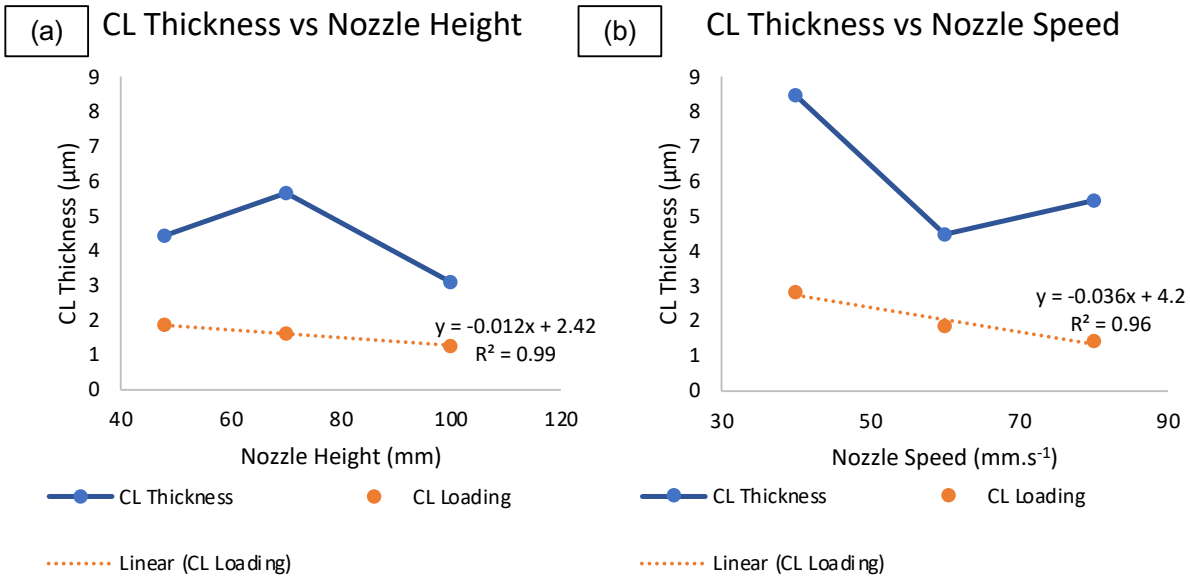

Figure 5.5: The CL thicknesses and loadings of the (a) nozzle height and (b) nozzle speed study samples

As the nozzle height increased from 48 mm to 100 mm, the deposited iridium loading decreased linearly as shown in Figure 5.5a. The decrease was expected as the increase in nozzle height led to an increase in the overspray margin, and less catalyst was deposited onto the membrane. The CL thickness does not show a linear correlation with the nozzle height. The data indicate that average thickness values may not be statistically different due to large standard deviations. This agrees with a previous study performed by Boisen et al (2013), where a detailed study on the influence of various spray coating parameters was performed on polymer films including the distance between the nozzle and the substrate. After these authors performed a statistical analysis, they identified the nozzle height as having no role in influencing the sprayed film thickness (Bose, Keller & Boisen, 2013b). When referring to an assumption made by Peng et al (2016) of considering a fabricated CL as an electrode sheet, sample NH3 has the lowest thickness, therefore it probably has the lowest through-plane transport resistance since it has the shortest proton transport path, which could increase overall CCM performance. Babic et al (2019), in a separate study of understanding the influence of anode catalyst loading on the proton transportation in CLs, recorded the proton transport resistance and double layer capacitance of the CL by collecting electrochemical impedance spectra from H_2/N_2 regime using transmission line model. They obtained similar results suggesting that an increase in CL thickness increased the proton and mass transport overpotentials (Babic et al., 2019b).

For the nozzle speed study samples, the Ir loading decreased linearly with increasing nozzle speed from 40 to 80 $mm.s^{-1}$. This is expected since the amount of catalyst deposited on the membrane per unit of time decreases with increasing nozzle speed. However, changing the nozzle speed appears to induce larger loss in CL loading with increasing the speed compared to changing the nozzle height. In addition, the change in CL thickness also appears non-linear with a change in the nozzle speed. CL thickness sharply decreases with increasing nozzle speed but then levels off when maximum speed is achieved. Sample NS2 had the lowest thickness, 4.5 ± 1.1 μm, despite having a higher Ir loading than sample NS3, and this result suggests sample NS2 has a denser CL.

The results recorded suggest that the nozzle height and speed have an influence on the catalyst loading deposited on the membrane.

Catalyst layer volume fraction: influence of nozzle height and speed

To investigate and understand how the CL microstructure is affected by the changing nozzle parameters, a procedure for calculating the volume fractions of catalyst, ionomer, and void was adopted from a study conducted by Gasteiger et al (2016). The volume fractions were determined using the equation below,

Equation 5.1. Volume fraction, *(catalyst or dry ionomer respectively) (Bernt & Gasteiger, 2016)

$$V_* = \frac{L_*}{\rho_* \times t_*}$$

The loading (L_*) , density (ρ_*), and electrode thickness (t_*) of the catalyst and ionomer respectively were required to calculate the volume fractions for each CL. The catalyst loading (L_{cat}) was determined by weighing as described previously in Chapter 3.1.2 and the average catalyst density (ρ_{cat}) for catalyst 1 with weight percentages of 86.9 wt% IrO_2 (density = 11.7 g.cm^{-3}) and 13.1 wt% TiO_2 (density = 4.23 g.cm^{-3})) was calculated as $\rho_{cat} = 10.7$ g.cm^{-3} . The electrode thickness (t_*) was determined from the SEM image analysis using a method described in Chapter 4.2. For the ionomer volume fraction calculation, the loading (L_{ion}) was 11,6 wt% of the total electrode weight, and the density (ρ_{ion}) was 2.1 g.cm^{-3}. According to previous studies, during electrolysis at 80^{o}C, the ionomer swells by a factor of X1.8 from the dry ionomer volume ($V_{ion\ dry}$), and this was recorded as the ionomer volume fraction ($V_{ion\ wet}$) (Liu et al., 2011). This study adopted the same approach and the total anode volume was determined using the equation below;

Equation 5.2: Total electrode volume fractions

$$V_{tot} = V_{cat} + V_{pore} + V_{ion\ wet}$$

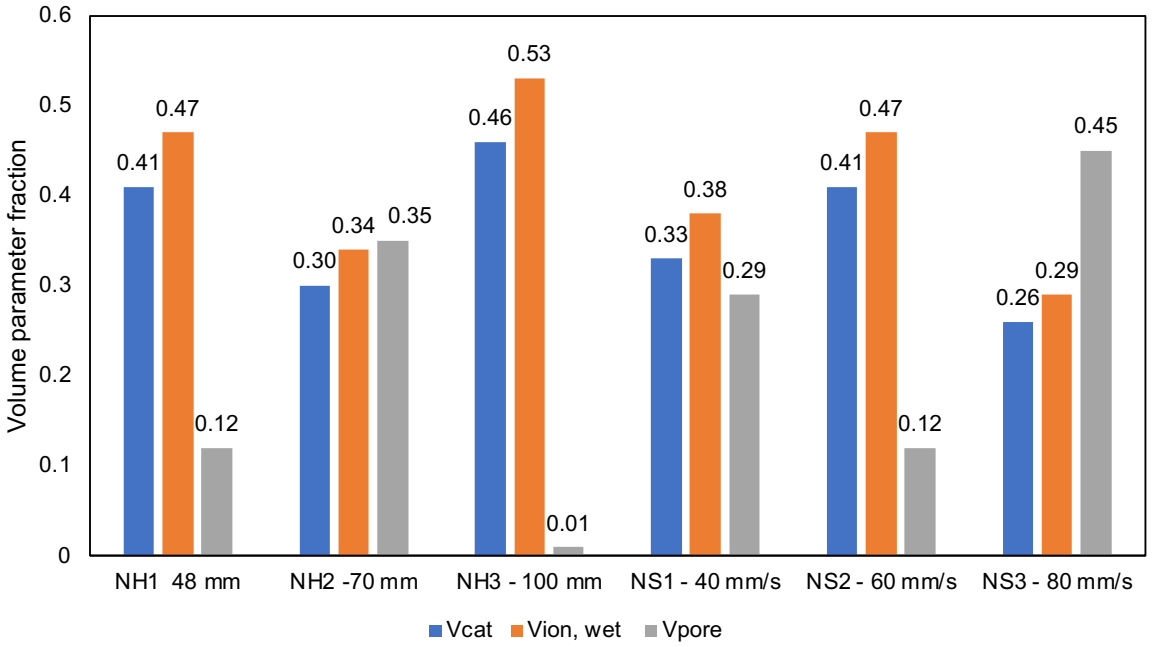

Figure 5.6: The CLs volume fractions summary for the nozzle height and speed study samples

For the nozzle height study, sample NH2 had the highest pore volume, 0.35, among all NH samples. This indicates that there is more porosity for reactants and products to be transmitted which could decrease mass transport resistance in the CL. Sample NH3 had the highest ionomer volume fraction, suggesting a high ionomer network, and that could increase the interconnection between catalyst agglomerates and positively influence the electronic and ionic conductivity of the CL, and improve overall CCM performance. Sample NS3 amongst the nozzle speed study samples exhibits the highest CL pore volume fraction, 0.45, and sample NS2 has the lowest 0.14. Samples NH2 and NS1 indicate the most balanced CL volume fractions among all studied samples. The balance could have a positive effect on overall CCM performance and catalyst utilisation as observed in a separate study by Babic et al (2019)

STEM – EDS analysis of anode CL cross-sections

Selected samples from nozzle height and nozzle speed studies were chosen for the STEM-EDS mapping to provide more information on CL compositions and microstructure. The HAADF image of sample NH1 is shown in Figure 5.7 (a) below.

From this section of the CL, STEM EDX maps of the independent elements Ir, F, O, and their combination were recorded and are shown below.

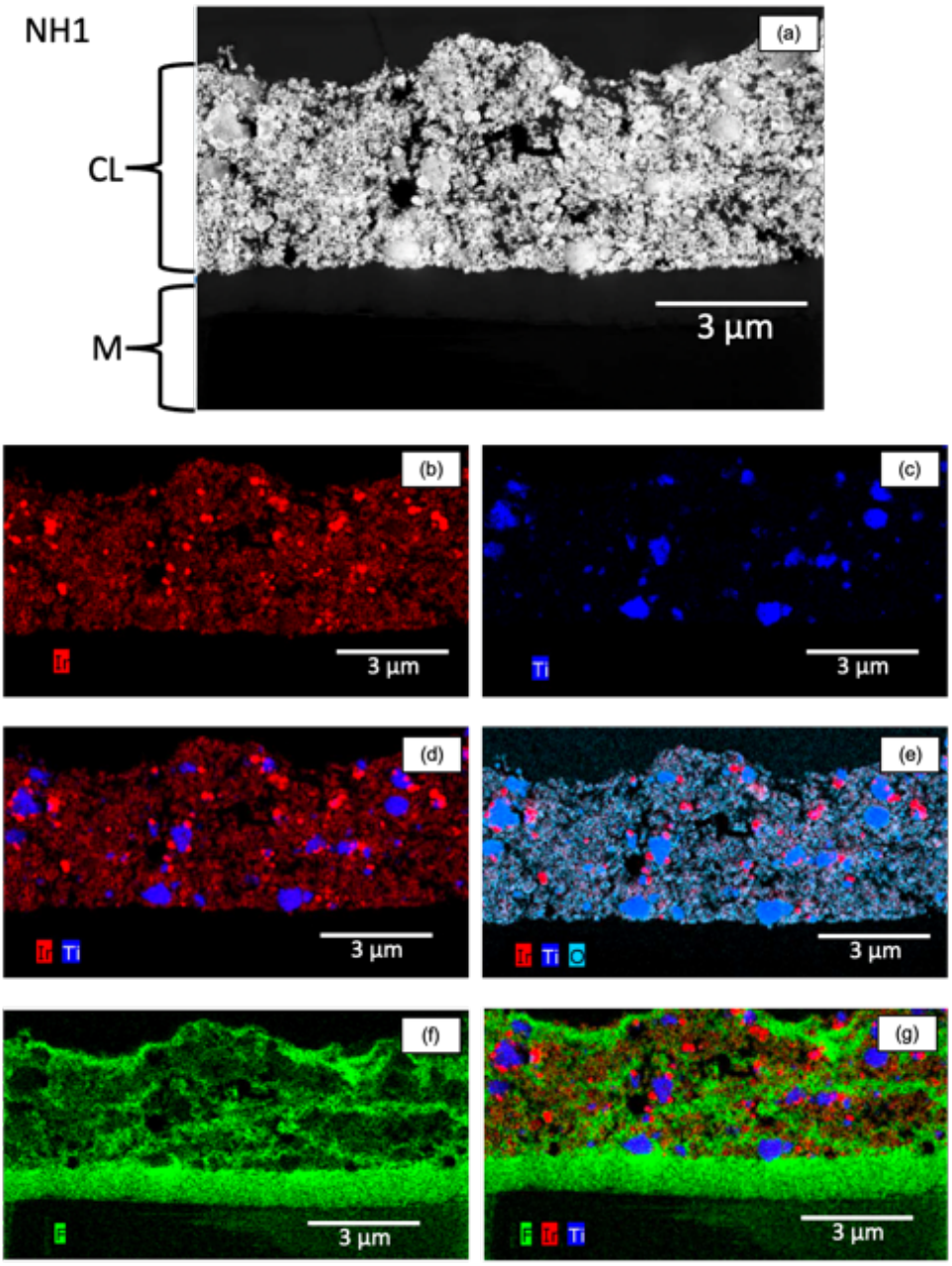

Figure 5.7: HAADF image and STEM/EDS maps image of NH1 sample outlining (a) the catalyst layer and a membrane, (b) Iridium distribution, (c) Titanium distribution, (d) Iridium and Titanium signal overlap, (e) Iridium, Titanium and Oxygen signal overlap, (f) Fluorine distribution, and (g) Iridium, Fluorine and Titanium signal overlap.

The HAADF image of sample NH1 shows differentiation between the CL (top bright region) and the membrane (bottom dark region). Within the CL there are contrast differences, with visible bright agglomerates of various sizes and distributed dark

sections signifying pores. This suggests the CL is non-uniform with unevenly distributed elements. Figure 5.7b is an independent Ir map and shows the presence of Ir-containing species across the whole CL cross-section.

However, certain regions contain particles from which a higher intensity red-coloured Ir signal was obtained indicating a larger local Ir concentration compared to the rest of the CL. These bright red spots appear uniformly distributed across the layer compared to the titanium agglomerates shown in Figure 5.7c. Such appearance is consistent with high contrast particles seen in Figure 5.8 . The Ir/Ti EDX map shows some Ir agglomerates attached to Ti agglomerates which were expected from catalyst 1 properties (IrOx supported on titania), but the majority of Ir signal is not in direct contact with Ti-containing particles. Figure 5.7e gives a better understanding of the catalyst species distribution and agglomeration. The overlap of the Ir, Ti, and O signals provides information on where oxide components are distributed within the CL. Oxygen signal is present in all regions where Ti-containing particles show, proving the presence of TiO_2 support. Regarding the Ir phase, oxygen signal distribution overlaps only with lower-intensity Ir regions, indicating the presence of IrOx agglomerates. However, the oxygen map does not confirm the signal overlap with high -intensity larger red particles. This suggests that those particles are composed of Ir metal and not IrOx.

The fluorine elemental EDX map in Figure 5.7f shows the intense green section at the bottom is fluorine present in the membrane. Within the CL the F map indicates the distribution of the ionomer network which is notably absent from areas occupied by catalyst agglomerates or pores. Figure 5.7g which combines all the EDX maps shows a complex CL composition, consisting of the IrOx phase, titania phase, and metallic Ir phase. Some metallic Ir particles are in contact with titania agglomerates while others are isolated. Ionomer appears mostly distributed between CL agglomerates. There are unevenly distributed dark sections that suggest non-uniform porosity within the CL. Higher magnification HAADAF and STEM EDX maps(Ir/Ti, Ir/Ti/O, and Ir/Ti/F) were recorded at 79 000X magnification to understand the agglomerate formation and elemental distribution and are shown in Figure 5.8 below.

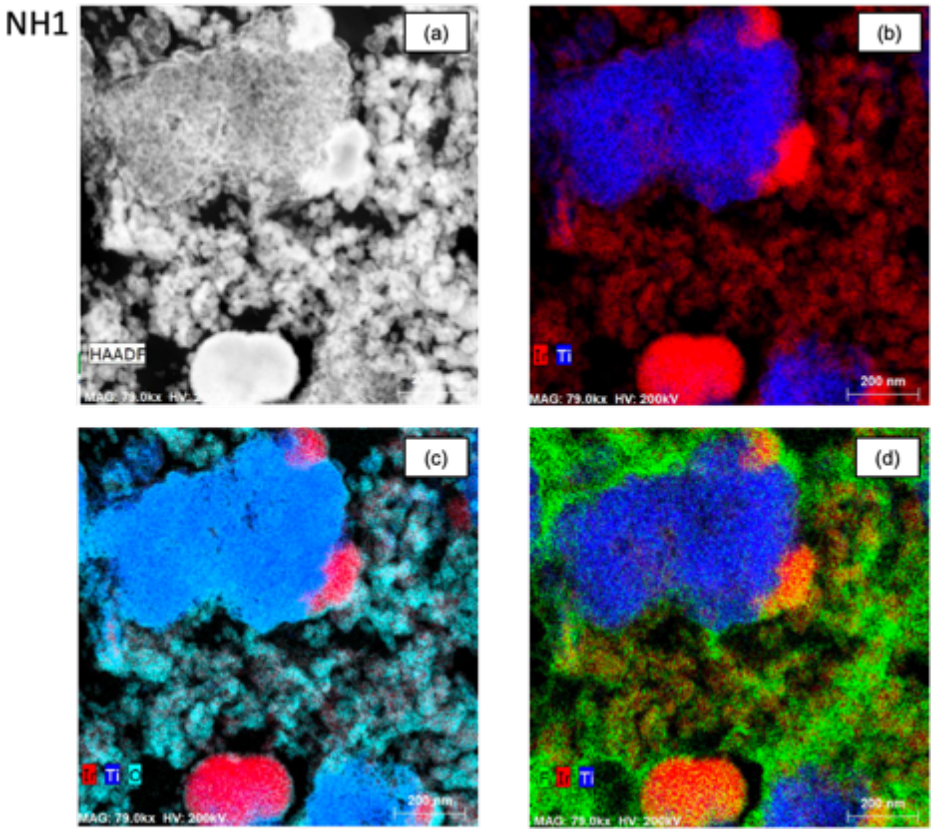

Figure 5.8: High magnification HAADF (a) and (b, c ,d) STEM EDX maps (Ir/Ti, Ir/Ti/O, Ir/Ti/F) for sample NH1

Figure 5.8a shows the different-sized agglomerates formed in the NH1 CL. The high in-contrast agglomerates suggest the presence of a high atomic number of elements which is consistent with the presence of Ir metal. The dark in contrast sections between the particles are the pores between the agglomerates in the CL. The Ir/Ti EDX map (Figure 5.8b) and Ir/Ti/O map (Figure 5.8c) show large 100 – 200 nm in diameter Ir particles that are either isolated or attached to the 600 nm TiOx substrate particle while a porous IrOx phase composed from smaller agglomerates (~50 nm) occupies the space in between. Figure 5.8d shows that ionomer film covers titania agglomerate, while its distribution in the IrOx phase is uneven with regions of high and low ionomer coverage. The dark in contrast sections in CL are CL pores. HAADF and STEM – EDX plots were then recorded for NH3 and NS1 to understand the influence of nozzle height and speed on CL microstructure and element distribution. Comparisons of NH1 and NH3 CL structures are expected to contribute to the understanding of the nozzle height effect, while those between NS1 and NH1/NS2 to the nozzle speed.

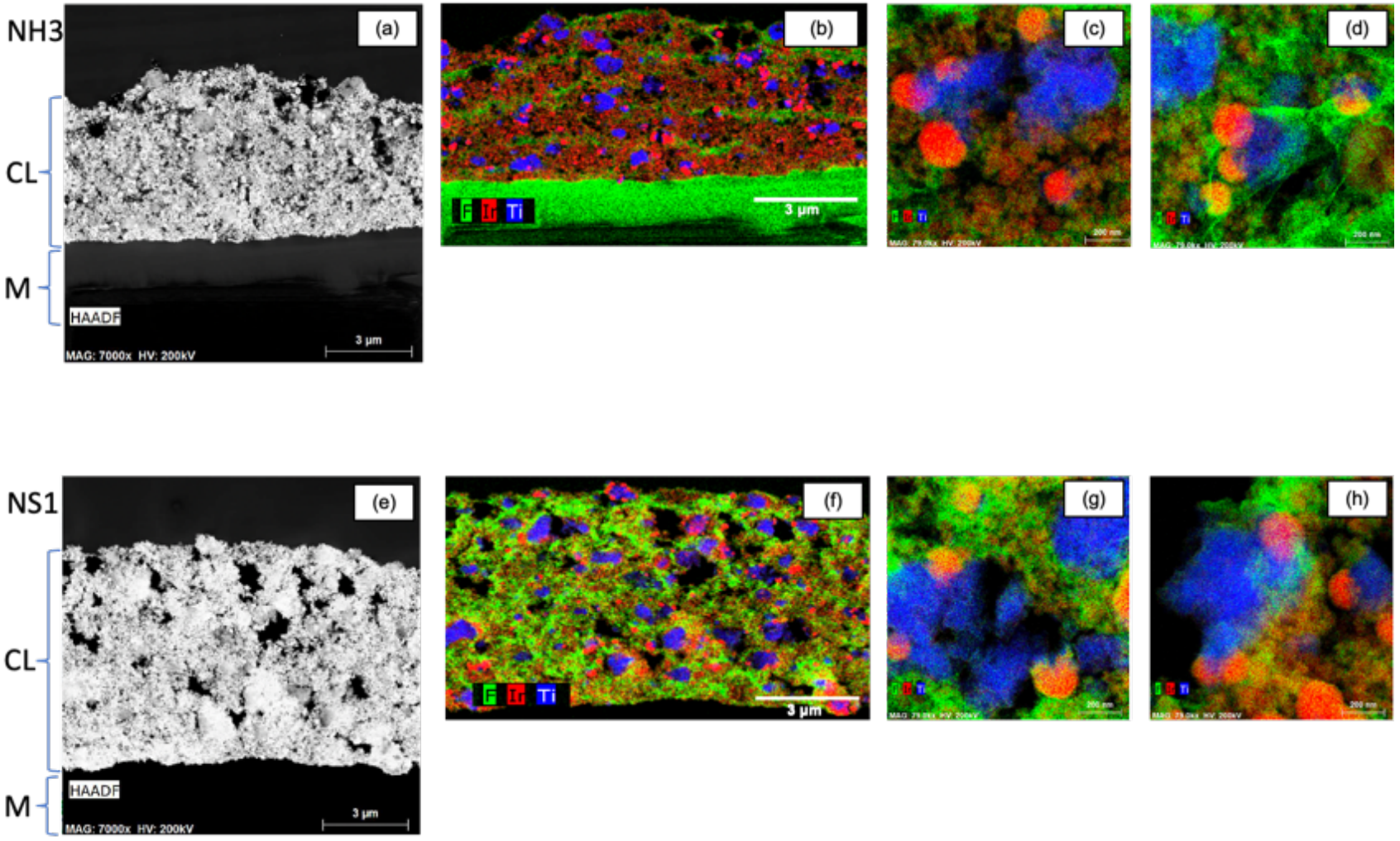

Figure 5.9: A HAADF and STEM - EDX elemental maps of NH3 anode catalyst layer (a, b, c, d) and (e, f, g, h) for NS1.

The HAADF images for NH3 and NS1 indicate that sample NS1's image appears brighter in contrast suggesting denser, agglomerates and this agrees with the higher catalyst loading in NS1. There are bigger and more visible pores in NS1 which supports the conclusions from calculated pore volume fractions (Figure 5.6). The increased pore volume in NS1 could positively impact the mass transportation of reactants and products to and from the active sites and increase performance as was concluded by Lopata et al (2020) in their study on the effects of the transport/catalyst layer and catalyst loading on mass and charge transport phenomena in PEMWE devices.(Lopata et al., 2020)

Analysing the ionomer distribution further, it's evident that in sample NS1, the ionomer, represented by the measured F signal (green color), forms a consistently even distribution across the CL cross-section, resulting in a well-connected network (Figure 5.9f). In contrast, as observed in NH3 (Figure 5.9b), the ionomer network exhibits variations. This homogeneous distribution of ionomer across the CL, exemplified by NS1, is crucial for enhancing proton conductivity and capacitance, both of which play pivotal roles in significantly improving the overall performance of the CCM. Conversely, in NH3, there is a noticeable lack of significant contact between the IrO_x phase and the ionomer phase (Figure 5.9b,c), contributing to the uneven spread of the ionomer network.

Areas where ionomer is concentrated (Figure 5.9 b,d) are narrow and appear to have a layered structure where ionomer regions are laterally connected while through plane connectivity is not apparent. The lower ionomer distribution penetration in NH3 could decrease ionic conductivity within the layer and hinder overall CCM performance. In contrast, NH3's CL cross-section reveals a more even distribution of Ir particles compared to NS1, indicating potentially greater contact between Ir and IrO_x phases. This contact could enhance electronic conductivity and likely contribute to overall CCM performance, aligning with findings from prior studies (Lopata et al., 2020). Both NH3 and NS1 EDS maps show evenly distributed large Ti substrate particles in isolated sections of the CLs which could increase local electronic insulation and hinder performance.

For the height study, the EDS maps of samples NH1 and NH3 show a layered ionomer distribution, stripes (green), between the catalyst agglomerates which were caused by the multiple spray passes. However, sample NH1 (lower height) shows a higher ionomer through plane connectivity compared to sample NH3. A balance of the ionomer through plane connectivity is required to achieve high ionic and electronic conductivity which influences the overall performance of the CCM. For the speed study, the EDS maps for sample NS1 and NH1/NS2 do not show a significant difference in through plane ionomer connectivity.

Electrolysis performance: influence of nozzle height and speed

The overall CCM performance of the 3 CCMs were measured using the protocol described in section 3.3. Polarisation curves stating the overall performance and catalyst utilisation of the nozzle study CCMs are shown in Figure 5.10 below.

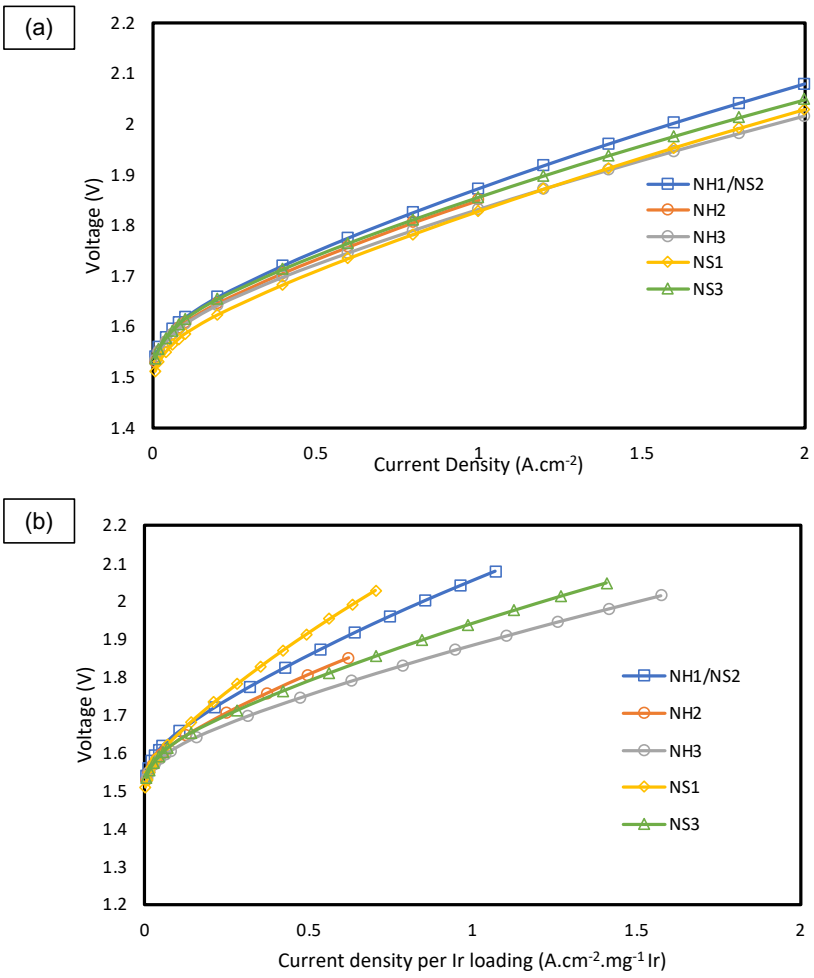

Figure 5.10: Overall performance polarisation curves for CCMs fabricated at different nozzle heights and speed (a), and (b) catalyst utilisation performance curves of the nozzle height and speed samples

For the nozzle height study, the overall CCM performance at 1 $A.cm^{-2}$ with an increase in nozzle height. Sample NH3 exhibited the best performance, with the lowest cell voltage of 1.83V required to reach $1A.cm^{-2}$, and the worst performing was sample NH1 with a cell voltage of 1.87 V at $1A.cm^{-2}$. To assess and compare the overall performance of the various CCM configurations, only the call voltage required to reach $1A.cm^{-2}$ was considered. Ideally, this should be accompanied with voltage loss breakdown analysis, obtained from EIS measurement. As the respective voltage loss analysis from EIS measurements were not possible in this study, the improved performance exhibited by sample NH3 is assumed to be due to reduced ohmic losses caused by a combination of a higher electronic and ionic conductivity observed from the more even ionomer distribution within NH3 CL compared to NH1. This was indicated by the STEM-EDS elemental maps.

From the nozzle speed samples, sample NS1 performed the best overall, recording a cell voltage of 1.83V at $1A.cm^{-2}$ and the lowest performing sample was NS2 at 1.88V at $1A.cm^{-2}$. The high performance from NS1 was likely caused by a combination of high CL loading of 2.84 mg $Ir.cm^{-2}$ and a more homogenous CL microstructure in terms of Vion, Vcat, and Vpore volume fractions ranging between 0.31 and 0.38 and an evenly distributed ionomer as shown in the EDS maps. These properties enhanced the CL microstructure by increasing the triple phase boundary, optimising the catalyst utilisation, and reducing the mass transport resistance of reactants and products to and from the active sites which have been observed in previous studies (Bernt & Gasteiger, 2016).

Sample NH1/NS2 had the lowest overall performance despite having the second-highest catalyst loading of 1.87 mg $Ir.cm^{-2}$. This could partially be attributed to its unevenly distributed ionomer observed in STEM EDS maps (Figure 5.7). The catalyst ink pooling on the membrane after spraying for NH1 was more pronounced since the nozzle was the shortest distance from the membrane, and the catalyst ink had the least time to dry from the nozzle tip to deposition on the membrane. A previous study by Alia et al (2020) made a similar observation when studying the effect of ultrasonic spray parameters on the catalyst layer's properties, electrolyser performance, and durability. They observed increased catalyst ink wet/pooling at a high spray rate which

formed less uniform CLs resulting in increased high transport and ohmic losses (Seeberger et al., 2021).

Comparing all nozzle study data, it is interesting to note that up to 2 $A.cm^{-2}$, a very similar performance was obtained from NH3 and NS1 samples despite NH3 having 50% lower Ir loading compared to NS1. The catalyst utilisation graph (Figure 5.10b) shows NH3 obtaining the highest current density per mg Ir at 1.8V of 0.63 $A.cm^{-2}.mg^{-1}$Ir. The volume fraction graphs indicate that this sample had the lowest CL thickness with the highest catalyst and ionomer fractions among all nozzle height and speed samples of 0.46 and 0.53 respectively. The lower loading likely decreased mass transport resistance while the high Vcat and Vion volume fractions probably increased the electronic and ionic conductivity within the CL increasing catalyst utilisation.

5.2 Anode loading study

To understand the influence of changes in the anode loading on the CL microstructure, 5 CCMs with different anode loadings ranging between 0.54 and 6.42 mg Ir.cm^{-2} with a constant cathode (0.5 mg Pt/C) were produced. The anode surface images obtained from SEM are shown in Figure 5.11 below;|

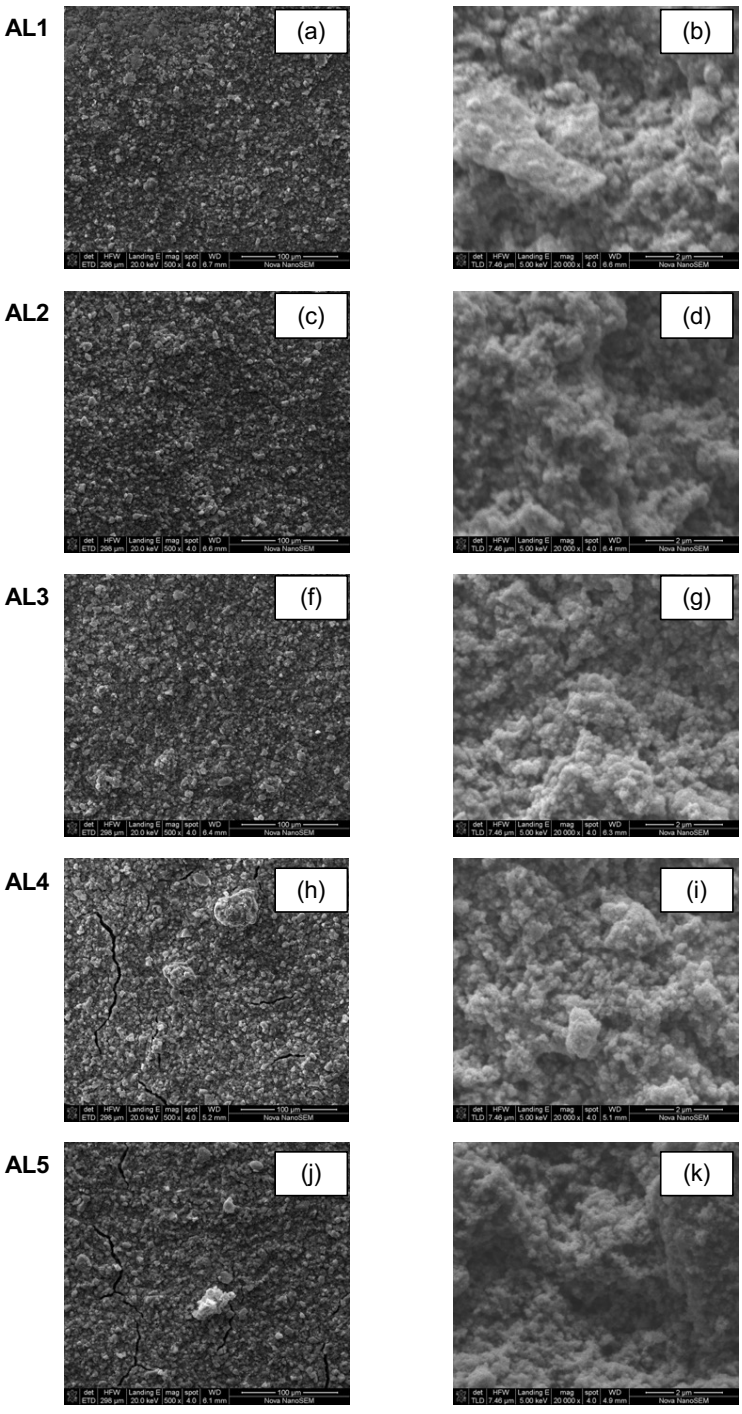

Figure 5.11: Surface images of the anode loading study samples (a,c e,g,i) low magnification (X500) and (b,d,f,h,j) high magnification (X20 000)

The low magnification surface images show full catalyst coverage of the membrane and more visible surface cracks for sample AL4 and sample AL5. These cracks appear shallow and, on the surface, and may have been caused by an increase in the evaporation rate of the solvents (IPA and water), as more catalyst ink was deposited on the membrane to meet the CCM loading specification. This is consistent with observations made by Sassin et al (2017) in a separate study of fabricating laboratory-scale high-performance membrane electrode assemblies for fuel cells. In their case the CLs sprayed at a lower height, 3.5cm contained surface cracks caused by the excess solvent in the ink that also triggered membrane deformation compared to higher spraying heights of 5 and 6.4 cm (Sassin et al., 2017b). The surface cracks could reduce mass transport resistance and water management difficulty during performance testing. The surface morphology at the high magnification for all the samples appears uniform, with laterally inter-connected catalyst agglomerates and there are visible bright sparsely distributed big catalyst agglomerates ($\approx$ 20 μm) on AL4 and AL5 surfaces. The overall morphology at the different loadings does not show visible changes.

Cross section images

To identify the differences in the CL microstructure, thickness, and attachment to the membrane at the different loadings, cross-section images using the SEM backscatter detector were obtained and are shown in Figure 5.12 below. The CL cross-section images show with increasing loading, catalyst layer thickness increases, which is expected. In addition, the catalyst layer microstructure shows the formation of large catalyst agglomerates (higher contrast regions) that are immersed within a matrix containing smaller particles and ionomer. These agglomerates appear more defined at higher loadings. The CL is attached to the membrane in all the samples. The CL microstructure differences can be observed from the variances in agglomerate sizes within the CL.

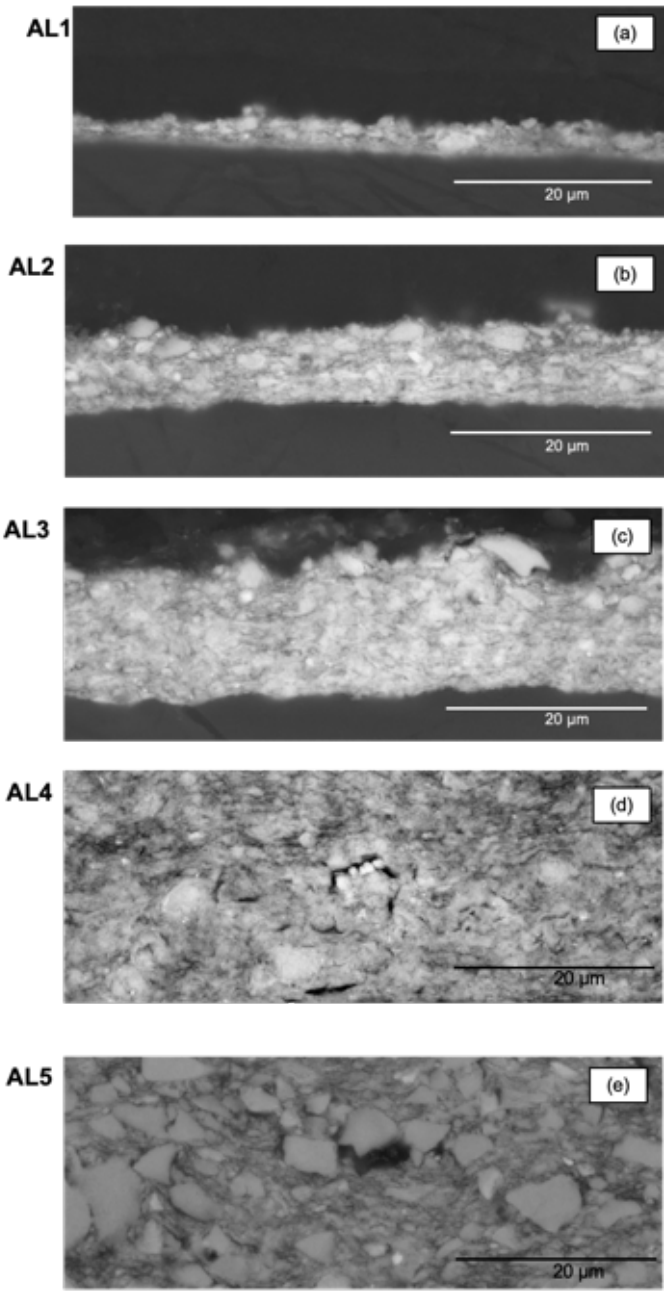

Figure 5.12: Cross section images of the anode loading study samples at X5 000 magnification

For this study AL2 and AL5 samples were selected and 20 widely spaced agglomerates from each sample were measured. The measured agglomerates for each sample were used to calculate and plot size distribution curves shown in Figure 5.13 below.

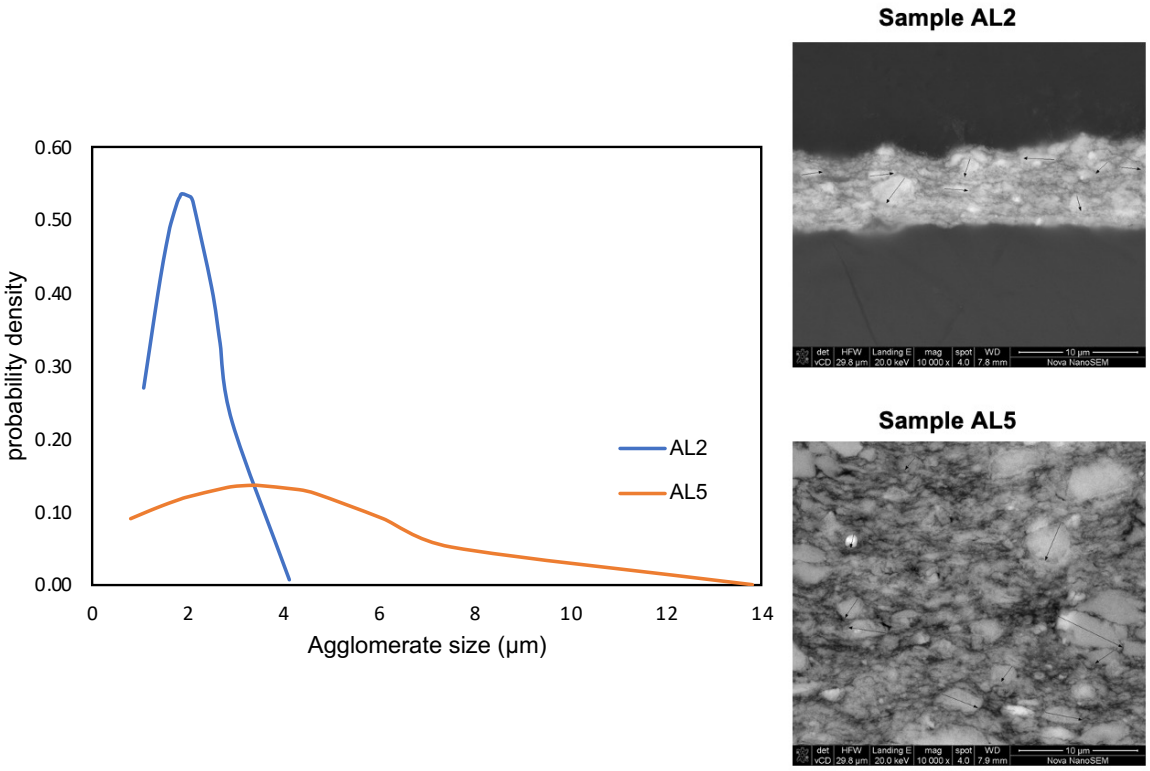

Figure 5.13: CL agglomerate size distribution chart and SEM cross-section images for sample AL2 and sample AL5

For each sample, two images from the backscatter detector at X10 000 magnification were selected, and ten evenly distributed agglomerates were measured from each image. The agglomerate sizes for sample AL5 were relatively bigger with a higher agglomerate size distribution than sample AL2 as shown in Figure 5.13. Sample AL5 recorded an average agglomerate size of 3.44 µm compared to 1.93 µm for sample AL2. This agglomerate size difference suggests a difference in the CL microstructure as the anode loading is varied, with more catalyst agglomeration at higher loadings which could have been caused by higher solvent evaporation rates (Bose, Keller & Boisen, 2013b). The anode catalyst loading and CL thickness was determined following the same procedure described in Chapter 4.2 and the results are summarised in Table 5.3 and Figure 5.14.

Table 5.3: The CL cross section thicknesses for the anode loading study samples

Sample	Ir loading ($mg.cm^{-2}$)	Anode Cross Section Thickness (µm)
AL1	0.54	4.8 ± 0.7
AL2	0.97	8.0 ± 1.0
AL3	2.06	12.9 ± 1.2
AL4	3.99	26.1 ± 5.4
AL5	6.42	34.6 ± 11.9

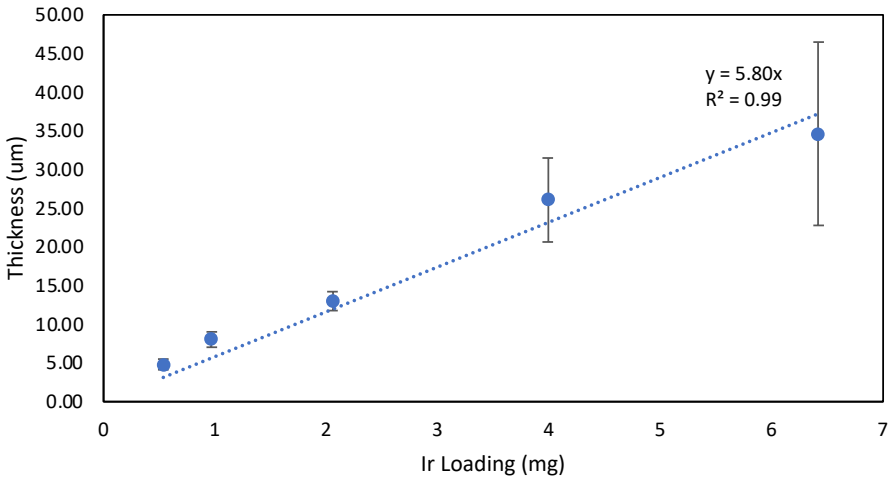

Figure 5.14: The CL thicknesses for the anode loading study samples

As expected, the CL thicknesses in all samples increased with an increase in Ir loading and exhibited a linearly correlated relationship, recording an R^2 of 0.99. The CLs at higher anode loadings have higher standard deviations which suggests a high CL variance caused by non-uniform and rough CLs. This agrees with the surface, cross section images and agglomerate sizes shown above, where at higher loadings isolated big catalyst agglomerates can be observed on the CL surfaces and the wide range of catalyst agglomerate sizes exhibited by AL5 ranging between 0.8 to 13.8 µm.

Catalyst layer volume fraction: influence of anode loading

The CL volume fractions comprising of catalyst, ionomer and pores were calculated for each CCM to understand the influence of catalyst loading on the fabricated CL microstructure and the results are summarised in Figure 5.15 below.

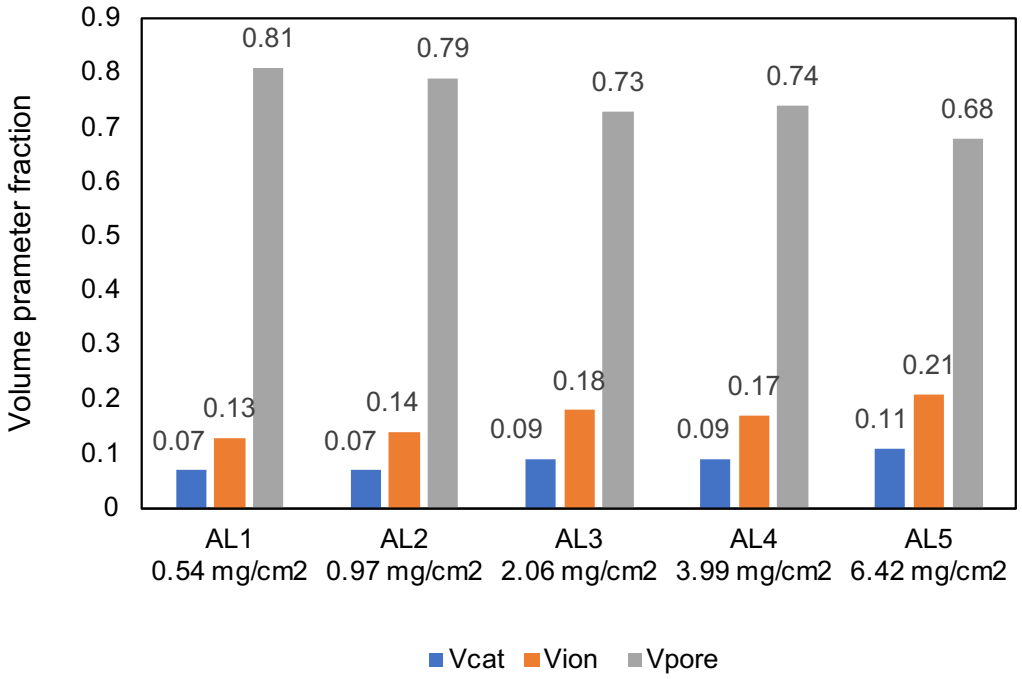

Figure 5.15: The CLs volume fractions summary for the anode loading study samples

The pore volume fractions in all samples are relatively high > 0.65 with samples AL1 and AL2 having the highest. However, sample AL5 has the lowest V_{pore}, 0.68, and the highest $V_{ion,}$ 0.21, and $V_{cat,}$ 0.11. Sample AL5 had a slightly higher ionomer volume fraction compared to the other samples and this could positively influence ionic conductivity and overall CCM performance as observed in a previous study by Alia et al (2020).(Alia et al., 2020) Overall, the CLs exhibit high pore volume fractions which are influenced by the type of catalyst.

STEM – EDS analysis of anode CL cross-section

Three samples (AL1, AL3, AL4) from the anode loading study were selected for the EDS measurements to help understand the microstructure differences caused by loading changes. The recorded EDS maps showing the distribution of Ir and F X-ray signals are shown in Figure 5.16 below;

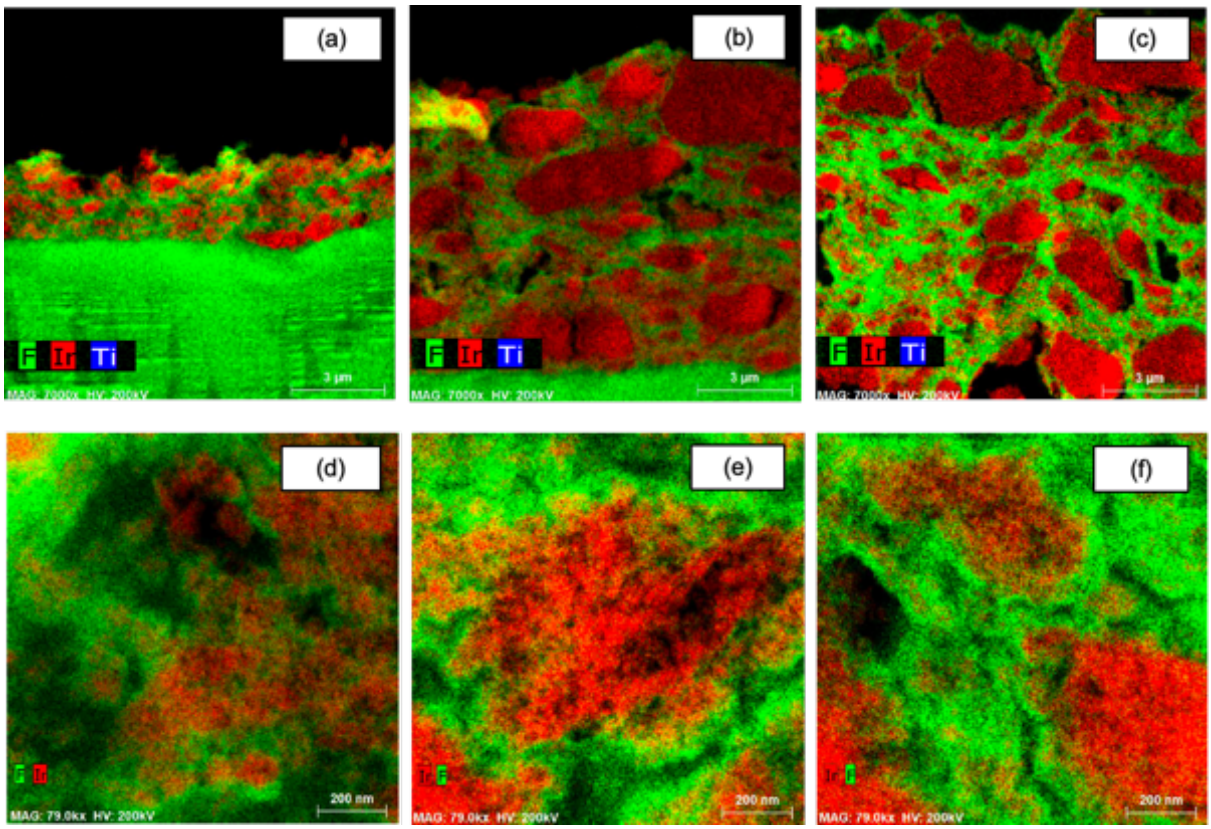

Figure 5.16: AL1 (a,d), AL3 (b,e) and AL4 (c,f) colour coded iridium and fluorine signal overlap EDX maps. The a,b and c maps are obtained at 7000x magnification while d, e and f maps were recorded at 79000x magnification after zooming in catalyst layer agglomerate regions.

All catalyst layers indicate that the ionomer network is distributed in between Ir agglomerates, although for the lowest loading sample AL1, ionomer appears to penetrate the agglomerate structure. Ir agglomerates increase in size with increasing loading and they also appear more porous within AL1 and AL3 catalyst layers compared to AL4 (Figure 5.16 d,e). AL3 shows the presence of large Ir agglomerates across the whole catalyst layer cross-section. These agglomerates are well connected within the ionomer matrix which could have a negative influence on the catalyst surface area but a positive on electronic conductivity in the CL. Figure 5.16c shows sample AL4 having unevenly sized agglomerates ranging between less than 1 micron to greater than 3 microns and an uneven ionomer distribution which suggests a higher degree of CL non-uniformity. Larger agglomerates are distributed at the outer regions of the catalyst layer (surface and interface with the membrane) while smaller

agglomerates are within the central region. Higher magnification maps (Figure 5.16 e,f) indicate that although Ir agglomerates are porous, ionomer penetration appears less compared to AL1. In addition, Figure 5.16f shows a higher presence of ionomer surrounding the iridium agglomerates which could enhance ionic conductivity increasing CCM performance or introduce electronic insulation within the CL decreasing the overall CCM performance. As expected, the EDS maps for the CLs from the anode loading study show different microstructure compared to CLs from the nozzle height and speed study primarily due to the differences in utilised catalyst.

Electrolysis performance: influence of anode loading

For performance comparisons polarisation curves were recorded for all 5 samples and their respective catalyst utilisation results calculated. The obtained results are shown in Figure 5.17 (a,b) below;

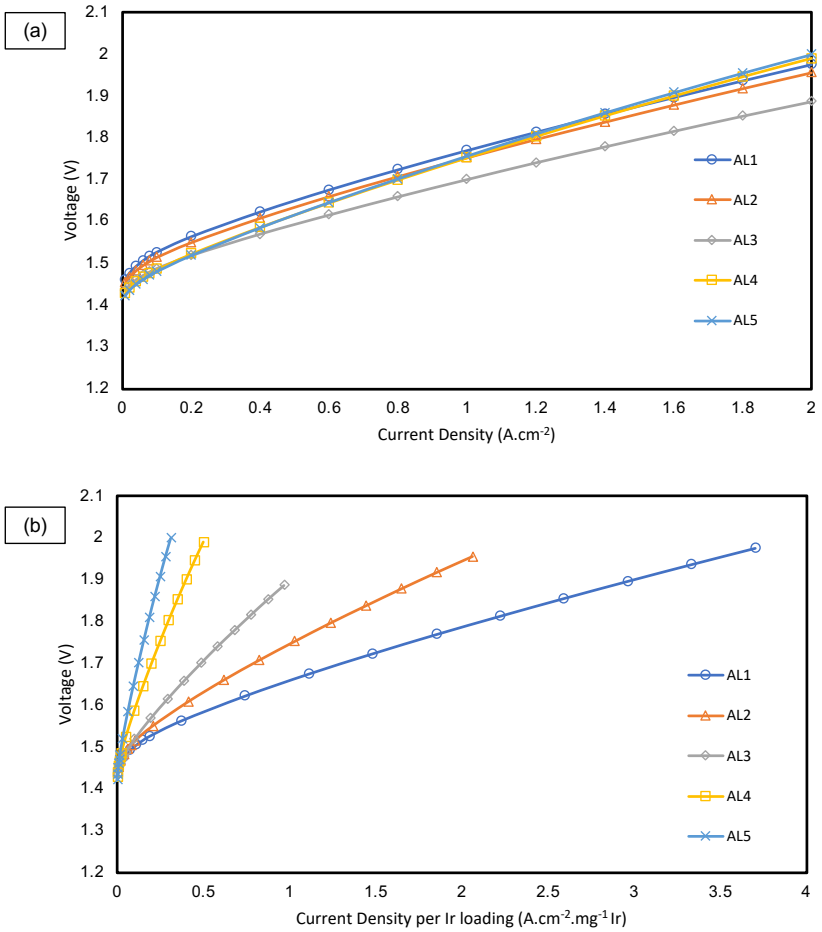

Figure 5.17: Polarisation curves for AL1 – AL5 (a), catalyst utilisation performance curves (b) at a fixed nozzle speed, 80 mm.s^{-1}, and height 55 mm.

The overall performance of the samples is relatively similar ranging between 1,75 – 1.77V at 1 $A.cm^{-2}$, except for Sample AL3. Sample AL3 shows the highest overall performance recording of 1,69V at 1 $A.cm^{-2}$ which was influenced by having a CL that had well-defined in-plane and through-plane connected catalyst agglomerates observed in the EDS maps (Figure 5.16b). These results show the importance of a catalyst layer microstructure (agglomerate size and distribution, ionomer, and pore network) in optimising the in and through-plane ionic and electronic conductivity. Sample AL1 exhibits the highest catalyst utilisation by recording the highest current density at 1.8V of 3.33 $A.cm^{-2}.mg^{-1}$Ir. The high catalyst utilisation in AL1 is influenced by its lowest CL thickness and the highest porosity of all anode-loading samples, which decreased the mass transport losses to and from its catalyst active sites. EDS maps indicate that AL1 has a more homogenous CL microstructure with smaller porous catalyst agglomerates where the ionomer is penetrating through rather than enveloping the agglomerate structures (Figure 5.16d vs. Figure 5.16e). This allows for improved proton conductivity at a low Ir loading. Overall, the recorded results show a correlation between the catalyst loading, the formed CL microstructure, and the overall CCM performance.

5.3 Comparison to commercial CCM benchmark

Samples NH1 and AL3 fabricated from the nozzle height and anode loading studies were compared to a commercial CCM (CM) to understand their relative CL microstructure and overall performance differences considering that all had similar Ir loadings. Initially, the CL surfaces were compared which are shown in Figure 5.18 below. Compared to the NH1 and AL3 samples, the CM has visible surface cracks which could influence the mass transportation of reactants and products to and from the catalyst's active sites. The surface variances were expected and could be partially explained by the differences in catalyst types, NH1 was fabricated from catalyst 1, AL3 from catalyst 2, and CM from catalyst 3, all from different undisclosed suppliers. Additionally, the fabrication methods were different, NH1 and AL3 were from ultrasonic spraying whereas CM was from screen printing.

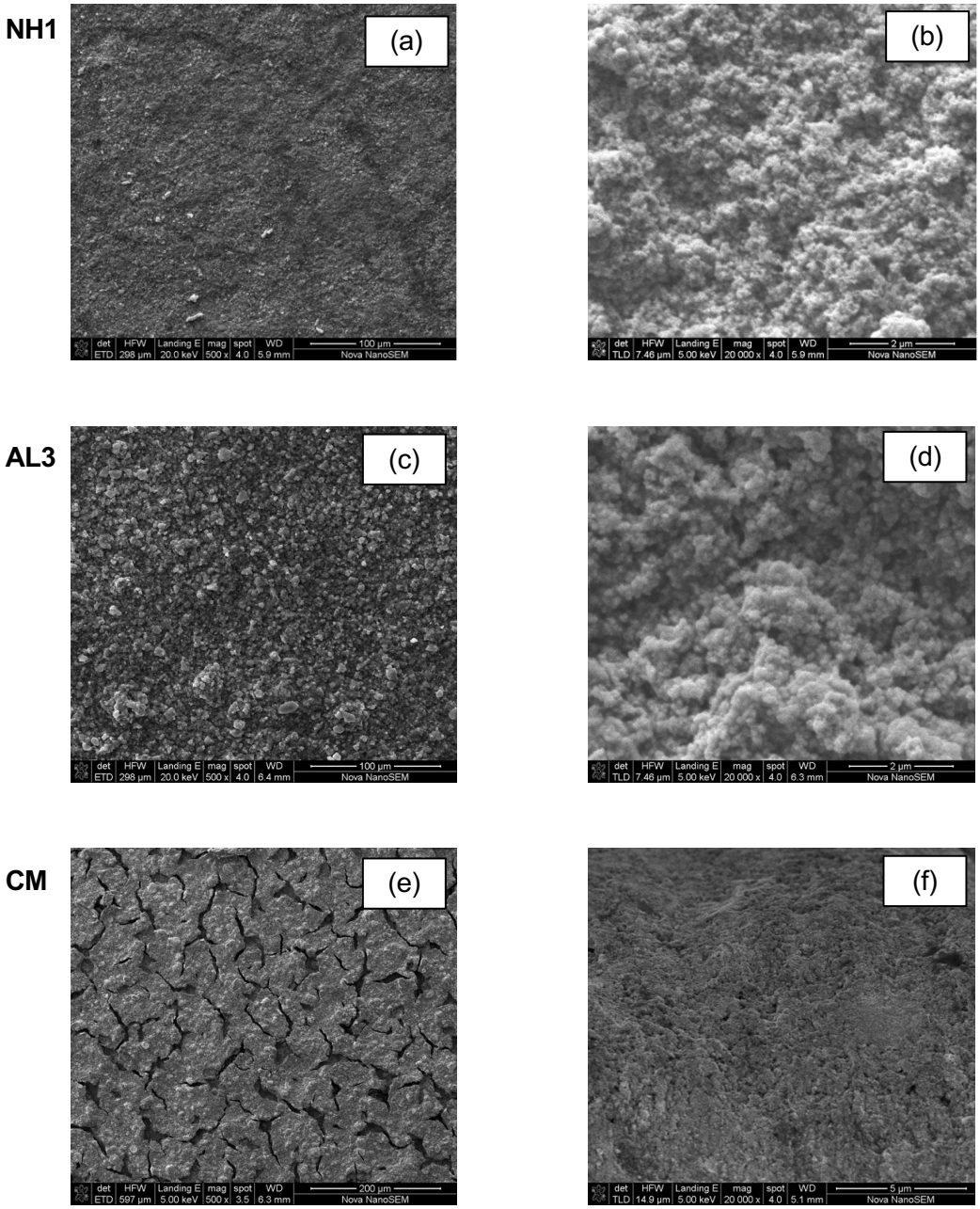

Figure 5.18: SEM surface images of sample NH1 (a,b), AL3 (c,d) , and CM (e,f), low magnification (X500) on the left and high magnification (X20 000) on the right

At a higher magnification, CM shows smaller agglomerates suggesting a finely textured surface as shown in Figure 5.19 below.

Cross section images

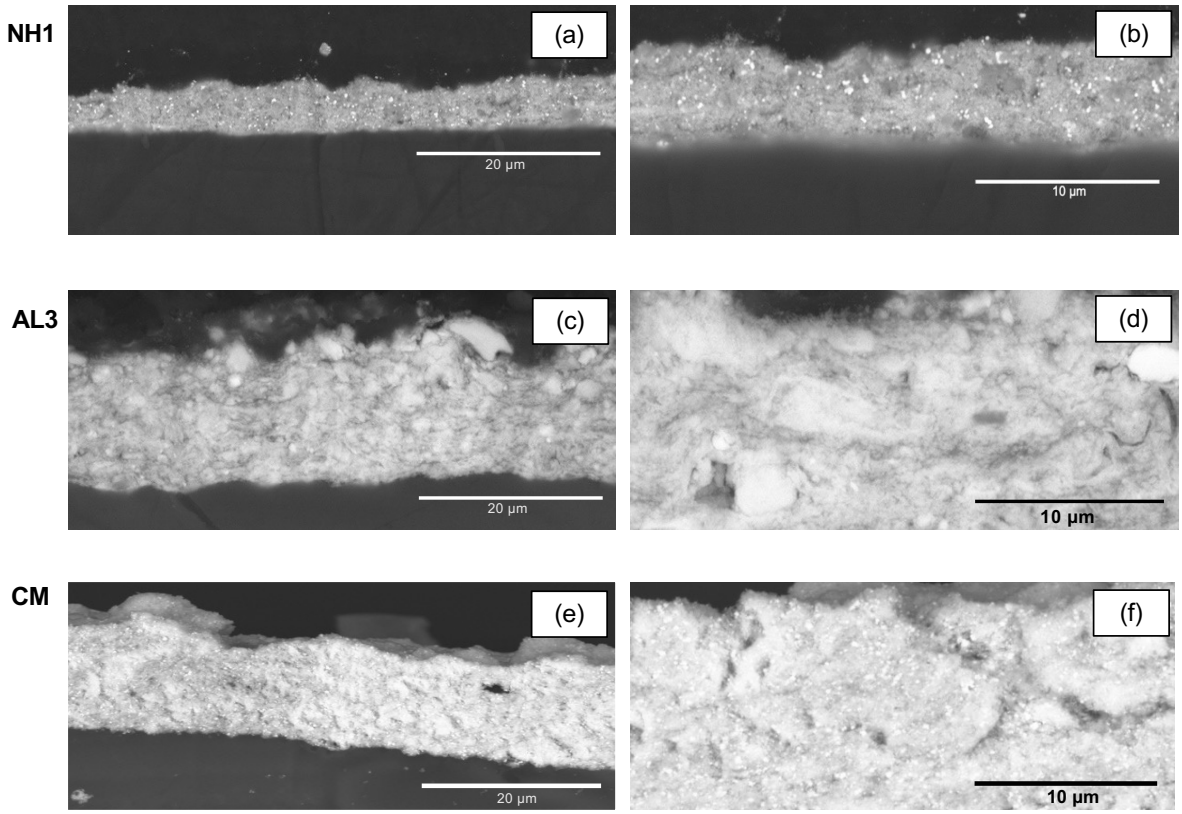

Figure 5.19: Cross section images of sample NH1 (a,b), AL3 (c,d), and CM (e,f) at low magnification (X5 000) on the left, and high magnification (X10 000) on the right

The CL cross-sections for all samples show the catalyst layer attached to the membrane, with AL3 and CM having relatively higher thicknesses compared to NH1. Additionally, differences in morphology can be observed for each CL cross-section due to different catalysts and fabrication method used. Images taken at higher magnification, indicate that AL3 and CM appear have higher porosity compared to NH1. The cross-section thicknesses for each CL are recorded in Table 5.4 below.

Table 5.4: The CL cross section thicknesses for the benchmark study samples

Sample	**Ir loading** **(mg.cm^{-2})**	**Anode Cross Section Thickness** **(µm)**
NH1	1.87	4.8 ± 1.0
AL3	2.06	12.9 + 1.2
CM	2.00	17.3 ± 3.9

The CL thickness calculations determined NH1 having the lowest thickness which agreed with the observations in SEM images in Figure 5.19. Sample CM had the CL thickness more comparable to sample AL3's when considering the thickness variation outlined by the standard deviations. The recorded CL thicknesses were used to calculate the volume fractions for each respective CL and the results are shown in Figure 5.20 below.

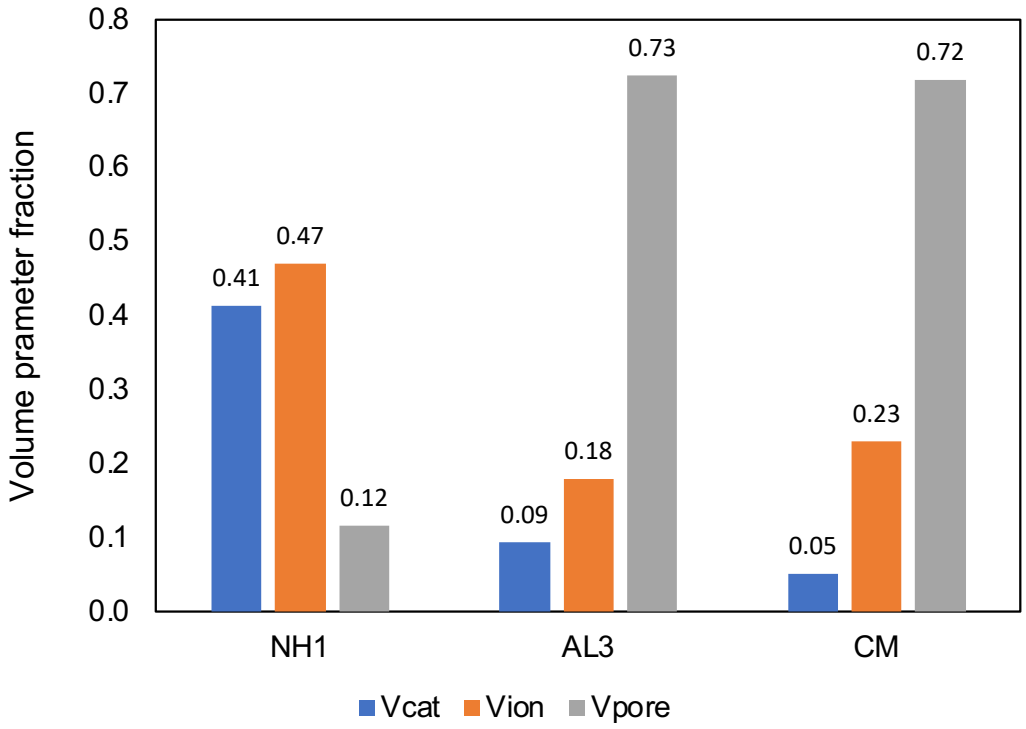

Figure 5.20: The CL volume fractions summary for the samples in the benchmark study

The volume fraction results show that samples AL3 and CM have comparab
le CL volume fractions in contrast to NH1 indicating differences in the ionic conductivity and mass transport of reactants and products across the three CLs.

Electrolysis performance:

The overall performance and catalyst utilisation results measured for each CCM are summarised in Figure 5.21 below.

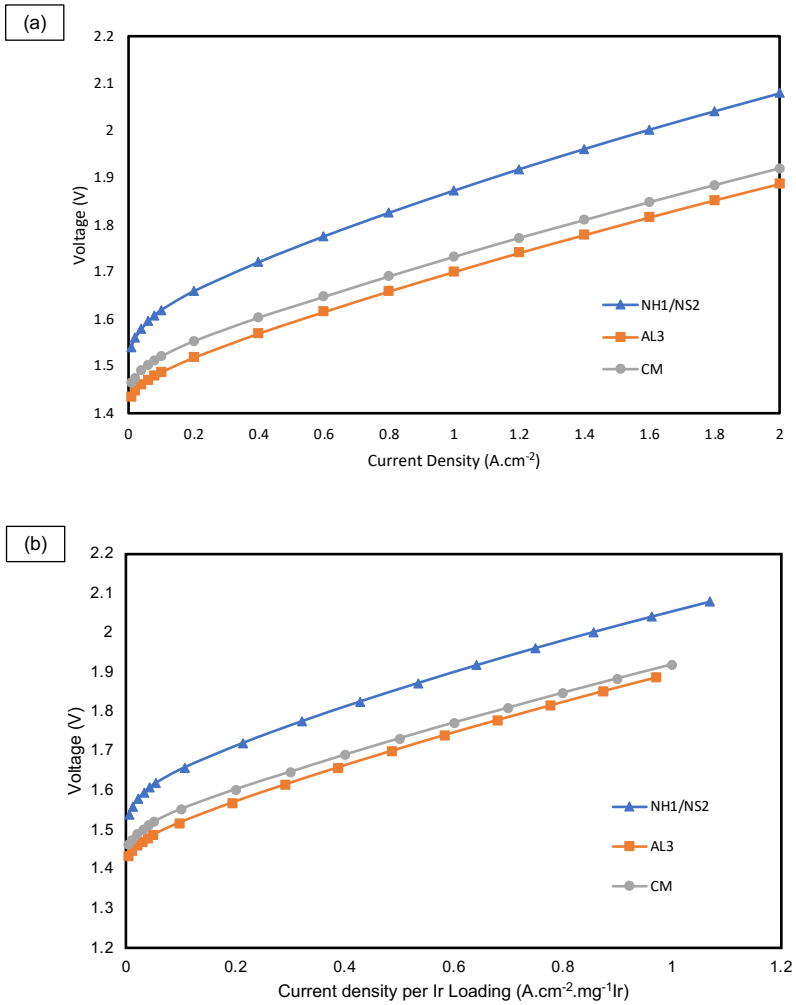

Figure 5.21: Polarisation curves for NH1/NS2, AL3, and CM (a), and catalyst utilisation performance curves (b) at comparable anode loadings (NH1/NS2 – 1.87 Ir mg, AL3 – 2.06 Ir mg, and CM – 2 Ir mg)

The highest overall performance at 1 A.cm^{-2} was recorded by sample AL3 of 1.7V and the lowest performance by NH1 of 1.87V. This indicates that considering similar Ir loadings, but different catalysts applied, lower mass transportation losses in the AL3 CL may be having a dominant contribution towards the overall performance. Additionally, sample AL3 exhibited the highest catalyst utilisation recording the highest current density per iridium mass loading of 0.74 A.cm^{-2}.mg^{-1}Ir at 1.8V. The high catalyst utilisation was possibly caused by the same reason of AL3 having a high pore volume fraction, this could have increased the mass transportation of reactants and products to and from the catalyst active sites which positively influenced catalyst utilisation.

6 Conclusions and recommendations

In this study, the influence of ultrasonic spraying parameters (nozzle height and nozzle speed) and anode loading were investigated to understand their influence on the anode catalyst layer microstructure (homogeneity and porosity), overall CCM performance, and catalyst utilisation. A process outlining the sequential steps for catalyst layer characterisation and catalyst layer thickness measurements was developed and performed using SEM, EDS, and STEM. For an increase in the nozzle height (48 mm – 100 mm), the catalyst layer loadings decreased. An inverse relationship was determined for the nozzle speed study where the deposited catalyst loading decreased with an increase in nozzle speed (40 $mm.s^{-1}$ – 80 $mm.s^{-1}$). Sample NH2 (H – 70mm, S – 60 $mm.s^{-1}$) and NS1 (H – 48 mm, S – 40 $mm.s^{-1}$) for the nozzle parameter study produced more balanced catalyst layer volume fractions, ranging between 0.29 and 0.38.

The STEM-EDS cross-section results of the nozzle height and speed study revealed non-homogeneous catalyst layers, which showed a combination of isolated Ir particles and Ir particles in contact with titania, and unevenly distributed pores. The STEM-EDS cross-section maps from the anode loading study showed a wider range of agglomerate sizes as the catalyst layer loading increased, resulting in more non-uniform catalyst layers. The commercial CCM SEM catalyst layer cross-section appeared to have more equally sized catalyst agglomerates and evenly distributed pores, suggesting a more homogeneous catalyst layer compared to the nozzle height, speed, and anode loading samples. A more homogenous catalyst layer for the commercial CCM likely increased the catalyst layer's ionic and electronic conduction and reduced mass transport losses.

For the anode loading study, as expected, the catalyst layer thickness increased linearly with an increase in the catalyst loading. The pore volume fractions for the anode loading study samples were relatively higher compared to the nozzle speed and height study, with Vpore ranging between 0.68 – 0.81 vs. range of 0.01 – 0.45 for the change in nozzle parameters. This was most likely due to the change in catalyst 1

(IrO_2/TiO_2) to catalyst 2 (IrO_x), and these results were supported by the differences in catalyst layer microstructures observed in the STEM-EDS maps. Among the anode loading samples, AL3 (2.06 mgIr.cm-2) performed the highest overall recording 1,69V at 1 $A.cm^{-2}$, and AL1 (0.54 $mgIr.cm^{-2}$) had the highest catalyst utilisation of 2.22 $A.cm^{-2}.mg^{-1}Ir$ at 1.8V due to a uniform catalyst layer with a high degree of homogeneity which might have reduced the CCM overpotentials.

Samples NH1 and AL3 with anode loadings of 1.87 and 2.06 $mgIr.cm^{-2}$ from catalyst 1 and catalyst 2 respectively, were benchmarked to a commercial CCM with a comparable anode loading of 2 $mgIr.cm^{-2}$. Sample AL3 exhibited similar volume fractions when compared to the commercial CCM suggesting similar CL porosity properties and ultimately, comparable catalyst attributes. The highest overall performance and catalyst utilisation from the comparison study results were achieved by AL3 recording 1.7V at 1 $A.cm^{-2}$ and a catalyst utilisation of 0.74 $A.cm^{-2}.mg^{-1}Ir$ at 1.8V. These results were partially caused by differences in catalyst types and a slightly higher anode loading for AL3.

This study demonstrated the influence of the ultrasonic spraying parameters (nozzle speed, nozzle height) and anode loading on the overall CCM performance and anode catalyst utilisation. This aligns with the initial research objective of investigating how ultrasonic spraying nozzle parameters influence anode catalyst layer microstructure and properties. A systematic method was developed to physically characterise the catalyst layer, to understand its microstructure, and elemental distribution which gave insights into the potential electronic, ionic conduction, and mass transport losses. In a further study to understand the influence of ultrasonic spraying parameters and variations in the anode loading, mercury intrusion porosimetry tests can be conducted to quantitively measure catalyst layer porosity and electrochemical impedance spectroscopy to effectively measure catalyst layer activity trends measuring charge transfer resistances to give more insights on the electrochemical characteristics of the catalyst, catalyst coating, and interfaces involved in the water electrolysis reaction. This could provide additional insights to address the initial research question regarding the effect of anode catalyst loading on catalyst layer morphology and electrolyser performance.To build on this work, future studies should consider the following:

1. Conduct triplicate spraying trials for statistical validation
2. Utilise mercury intrusion porosimetry to quantify pore structure trends
3. Conduct electrochemical impedance spectroscopy to explore how losses relate to the microstructure of the catalyst layer.
4. Test durability of optimised CCMs under high current densities
5. Investigate interactions between variables through design of experiments
6. Assess the economic viability of adopting ultrasonic spraying in PEMWE manufacturing.

This study set out to indicate the influence of ultrasonic spraying parameters and the anode loading on the catalyst layer microstructure, overall CCM performance, anode catalyst utilisation, and performance benchmark selected samples with a comparable commercial CCM. The results show that further optimisation of these parameters could lead to low-loaded homogenous anode catalyst layers, higher overall CCM performances, and anode catalyst utilisation. This supports the hypothesis that optimised ultrasonic spraying can produce comparable low-loaded catalyst layers to assist PEMWE adoption, though further optimisation is still needed.

REFERENCE LIST

Abderezzak, B. 2018. Introduction to Hydrogen Technology. *Introduction to Transfer Phenomena in PEM Fuel Cell*. (January, 1):1–51. DOI: 10.1016/B978-1-78548-291-5.50001-9.

Advanced MicroAnalytical. 2021. *No Title*. Available: https://www.advancedmicroanalytical.com/AMAServices.aspx?mode=tech&ID=7.

Alcaide, F., Álvarez, G., Cabot, P.L., Genova-koleva, R., Grande, H. & Miguel, O. 2017. Electrochimica Acta Effect of the solvent in the catalyst ink preparation on the properties and performance of unsupported PtRu catalyst layers in direct methanol fuel cells. *Electrochimica Acta*. 231:529–538. DOI: 10.1016/j.electacta.2017.02.127.

Alia, S.M., Reeves, K.S., Baxter, J.S. & Cullen, D.A. 2020. The Impact of Ink and Spray Variables on Catalyst Layer Properties, Electrolyzer Performance, and Electrolyzer Durability. *Journal of The Electrochemical Society*. 167(14):144512. DOI: 10.1149/1945-7111/abc746.

Antonio Scipioni, Alessandro Manzardo & Jingzheng Ren. 2019. *Hydrogen Economy Supply Chain, Life Cycle Analysis and Energy Transition for Sustainability*. V. 1.

Article, R. 2017. Review of characterization and modeling of polymer electro- lyte fuel cell catalyst layer : The blessing and curse of ionomer. 11(3):334–364. DOI: 10.1007/s11708-017-0490-6.

Ayers, K., Danilovic, N., Ouimet, R., Carmo, M., Pivovar, B. & Bornstein, M. 2019. Perspectives on Low-Temperature Electrolysis and Potential for Renewable Hydrogen at Scale.

Babic, U., Suermann, M., Felix, N.B., Gubler, L. & Schmidt, T.J. 2017. Review — Identifying Critical Gaps for Polymer Electrolyte Water. 164(4):387–399. DOI: 10.1149/2.1441704jes.

Babic, U., Nilsson, E., Alexandra, P. & Schmidt, T.J. 2019a. Proton Transport in Catalyst Layers of a Polymer Electrolyte Water Electrolyzer : Effect of the Anode Catalyst Loading. 166(4):214–220. DOI: 10.1149/2.0341904jes.

Babic, U., Nilsson, E., Alexandra, P. & Schmidt, T.J. 2019b. Proton Transport in Catalyst Layers of a Polymer Electrolyte Water Electrolyzer : Effect of the Anode Catalyst Loading. 166(4):214–220. DOI: 10.1149/2.0341904jes.

Bender, G., Carmo, M., Smolinka, T., Gago, A., Danilovic, N., Mueller, M., Ganci, F., Fallisch, A., et al. 2019. ScienceDirect Initial approaches in benchmarking and round

robin testing for proton exchange membrane water electrolyzers. *International Journal of Hydrogen Energy*. 44(18):9174–9187. DOI: 10.1016/j.ijhydene.2019.02.074.

Bernt, M. & Gasteiger, H.A. 2016. FOR I NCREASED Influence of Ionomer Content in IrO 2 / TiO 2 Electrodes on PEM Water Electrolyzer Performance. 163(11):3179–3189. DOI: 10.1149/2.0231611jes.

Bose, S., Keller, S.S. & Boisen, A. 2013a. Process Optimization of Ultrasonic Spray Coating of Polymer Films. DOI: 10.1021/la4010246.

Bose, S., Keller, S.S. & Boisen, A. 2013b. Process Optimization of Ultrasonic Spray Coating of Polymer Films. DOI: 10.1021/la4010246.

Carmo, M. & Fritz, D.L. 2013. A comprehensive review on PEM water electrolysis. 8(1). DOI: 10.1016/j.ijhydene.2013.01.151.

Dixit, M.B., Soc, J.E., Dixit, M.B., Harkey, B.A., Shen, F. & Hatzell, K.B. 2018a. Catalyst Layer Ink Interactions That Affect Coatability. DOI: 10.1149/2.0191805jes.

Dixit, M.B., Soc, J.E., Dixit, M.B., Harkey, B.A., Shen, F. & Hatzell, K.B. 2018b. Catalyst Layer Ink Interactions That Affect Coatability. DOI: 10.1149/2.0191805jes.

Efremenko, V.G., Tsvetkova, E. V, Dzherenova, A. V & Zurnadzhy, V.I. 2020. Секція: фізика. 266–267.

Endoo, S., Pruksathorn, K. & Piumsomboon, P. 2010. Identification of the key variables in membrane electrode preparation for PEM fuel cells by a factorial design. *Renewable Energy*. 35(4):807–813. DOI: 10.1016/j.renene.2009.10.013.

Everhart, T.E. & Thornley, R.F.M. 1960. Wide-band detector for micro-microampere low-energy electron currents. *Journal of Scientific Instruments*. 37(7):246–248. DOI: 10.1088/0950-7671/37/7/307.

G. A. Melo, L., Hitchcock, A.P., Jankovic, J., Stumper, J., Susac, D. & Berejnov, V. 2017. Quantitative Mapping of Ionomer in Catalyst Layers by Electron and X-ray Spectromicroscopy. *ECS Transactions*. 80(8):275–282. DOI: 10.1149/08008.0275ecst.

Grigoriev, S.A., Porembsky, V.I. & Fateev, V.N. 2006. Pure hydrogen production by PEM electrolysis for hydrogen energy. 31:171–175. DOI: 10.1016/j.ijhydene.2005.04.038.

Havancsak, K. 2019. *No Title*. Available: http://www.technoorg.hu/news-and-events/articles/high-resolution-scanning-electron-microscopy-1/.

Hegge, F., Holzapfel, P., Bierling, M. & Suermann, M. 2019. Optimization of anodic porous transport electrodes for proton exchange membrane water electrolyzers. 1(Ccm):26984–26995. DOI: 10.1039/c9ta08396k.

Hutagalung, A. 1967. *済無No Title No Title No Title*.

Laguna-Bercero, M. 2012. Recent advances in high temperature electrolysis using Solid Oxide Fuel Cells : A review. 1–54.

Laguna-Bercero, M. n.d. Recent advances in high temperature electrolysis using Solid Oxide Fuel Cells : A review. 1–54.

De las Heras, A., Vivas, F.J., Segura, F. & Andújar, J.M. 2018. DOI: 10.1016/j.rser.2018.07.036.

Liu, Y., Ji, C., Gu, W., Jorne, J. & Gasteiger, H.A. 2011. Effects of Catalyst Carbon Support on Proton Conduction and Cathode Performance in PEM Fuel Cells Effects of Catalyst Carbon Support on Proton Conduction and Cathode Performance in PEM Fuel Cells. DOI: 10.1149/1.3562945.

Lopata, J., Kang, Z., Young, J., Bender, G., Weidner, J.W. & Shimpalee, S. 2020. Effects of the Transport/Catalyst Layer Interface and Catalyst Loading on Mass and Charge Transport Phenomena in Polymer Electrolyte Membrane Water Electrolysis Devices. *Journal of The Electrochemical Society*. 167(6):064507. DOI: 10.1149/1945-7111/ab7f87.

Luft, John (University of Washington, S. 1961. Improvements Embedding in Epoxy Resin Methods. *The Journal Of Biophysical and Biochemical Cytology*. 409–414.

Ma, L., Sui, S. & Zhai, Y. 2009. Investigations on high performance proton exchange membrane water electrolyzer. *International Journal of Hydrogen Energy*. 34(2):678–684. DOI: 10.1016/j.ijhydene.2008.11.022.

Maldonado, L. 2019. Experimental characterization of water sorption and transport properties of polymer electrolyte membranes for fuel cells Libeth Maldonado Sánchez To cite this version : HAL Id : tel-02074195 soutenance et mis à disposition de l ' ensemble de la Contact : .

Manco, J. & Niedzwiecki, M. 2010. Research Advances Towards Low Cost, High Efficiency PEM Electrolysis. 33(1):3–15.

Mohammadi, A. & Mehrpooya, M. 2018. A comprehensive review on coupling different types of electrolyzer to renewable energy sources. *Energy*. 158:632–655. DOI: 10.1016/j.energy.2018.06.073.

Naimi, Y. & Antar, A. 2018. Hydrogen Generation by Water Electrolysis. *Advances In Hydrogen Generation Technologies*. 1–18. DOI: 10.5772/intechopen.76814.

Orfanidi, A., Rheinländer, P.J., Schulte, N. & Gasteiger, H.A. 2018. Ink Solvent Dependence of the Ionomer Distribution in the Catalyst Layer of a PEMFC. *Journal of The Electrochemical Society*. 165(14):F1254–F1263. DOI: 10.1149/2.1251814jes.

Peng, X., Omasta, T., Rigdon, W. & Mustain, W.E. 2016. Fabrication of High Performing PEMFC Catalyst-Coated Membranes with a Low Cost Air-Assisted Cylindrical Liquid Jets Spraying System. *Journal of The Electrochemical Society*. 163(14):E407–E413. DOI: 10.1149/2.0981614jes.

Pettersson, J., Ramsey, B. & Harrison, D. 2006. A review of the latest developments in electrodes for unitised regenerative polymer electrolyte fuel cells. 157:28–34. DOI: 10.1016/j.jpowsour.2006.01.059.

Pham, C. Van, Escalera-López, D., Mayrhofer, K., Cherevko, S. & Thiele, S. 2021. DOI: 10.1002/aenm.202101998.

Ponce, A., Mejía-rosales, S. & José-yacamán, M. 2012. Chapter 37 for the Analysis of Nanoparticles. 906:453–471. DOI: 10.1007/978-1-61779-953-2.

Quaino, P., Juarez, F., Santos, E. & Schmickler, W. 2014. Volcano plots in hydrogen electrocatalysis-uses and abuses. *Beilstein Journal of Nanotechnology*. 5(1):846–854. DOI: 10.3762/bjnano.5.96.

Ramachandran, R. & Menont, R.K. 1998. *AN OVERVIEW OF INDUSTRIAL USES OF HYDROGEN*.

Rashid, M., Mesfer, M.K. Al, Naseem, H. & Danish, M. 2015. Hydrogen Production by Water Electrolysis : A Review of Alkaline Water Electrolysis , PEM Water Electrolysis and High Temperature Water Electrolysis. (3):80–93.

Reier, T., Oezaslan, M. & Strasser, P. 2012a. Electrocatalytic Oxygen Evolution Reaction (OER) on Ru , Ir , and Pt Catalysts : A Comparative Study of Nanoparticles and Bulk Materials. DOI: 10.1021/cs3003098.

Reier, T., Oezaslan, M. & Strasser, P. 2012b. Electrocatalytic Oxygen Evolution Reaction (OER) on Ru , Ir , and Pt Catalysts : A Comparative Study of Nanoparticles and Bulk Materials. DOI: 10.1021/cs3003098.

Sassin, M.B., Garsany, Y., Gould, B.D. & Swider-lyons, K.E. 2017a. Fabrication Method for Laboratory-Scale High-Performance Membrane Electrode Assemblies for Fuel Cells. DOI: 10.1021/acs.analchem.6b03005.

Sassin, M.B., Garsany, Y., Gould, B.D. & Swider-lyons, K.E. 2017b. Fabrication Method for Laboratory-Scale High-Performance Membrane Electrode Assemblies for Fuel Cells. DOI: 10.1021/acs.analchem.6b03005.

Sci, C. 2014a. Catalysis Science & Technology Developments and perspectives of oxide-based. *Catalysis Science & Technology*. 4:3800–3821. DOI: 10.1039/C4CY00669K.

Sci, C. 2014b. Catalysis Science & Technology Developments and perspectives of oxide-based. *Catalysis Science & Technology*. 4:3800–3821. DOI: 10.1039/C4CY00669K.

Sci, C. 2014c. Catalysis Science & Technology Developments and perspectives of oxide-based. 3800–3821. DOI: 10.1039/c4cy00669k.

Seeberger, D., Hauenstein, P., Hartert, A. & Thiele, S. 2021. The influence of the anion exchange membrane on mass-transport limiting phenomena in bipolar interface fuel cells with Fe-N/C based cathode catalyst layers. *RSC Advances*. 11(50):31477–31486. DOI: 10.1039/d1ra05010a.

Shiva Kumar, S. & Himabindu, V. 2019. DOI: 10.1016/j.mset.2019.03.002.

Shukla, S., Wei, F., Mandal, M., Zhou, J., Saha, M.S., Stumper, J. & Secanell, M. 2019. Determination of PEFC Gas Diffusion Layer and Catalyst Layer Porosity Utilizing Archimedes Principle. *Journal of The Electrochemical Society*. 166(15):F1142–F1147. DOI: 10.1149/2.0251915jes.

Spöri, C., Briois, P., Nong, H.N., Reier, T., Billard, A., Kühl, S., Teschner, D. & Strasser, P. 2019. Experimental Activity Descriptors for Iridium-Based Catalysts for the Electrochemical Oxygen Evolution Reaction (OER). *ACS Catalysis*. 9(8):6653–6663. DOI: 10.1021/acscatal.9b00648.

Tang, Y.L., Karlsson, A.M. & Cleghorn, S. 2006. An Experimental Investigation of Humidity and Temperature Effects on the Mechanical Properties of Persfluorosulfonic Acid Membrane. 2006:297–304.

Thermo Fisher Scientific. 2021. *No Title*. Available: https://www.fei.com/introduction-to-electron-microscopy/stem/#gsc.tab=0 [2021, September 03].

Trasatti, S. 1972. Work function, electronegativity, and electrochemical behaviour of metals: III. Electrolytic hydrogen evolution in acid solutions. *Journal of Electroanalytical Chemistry and Interfacial Electrochemistry*. 39(1):163–184. DOI: 10.1016/S0022-0728(72)80485-6.

UNFCCC. 2015. Convention on Climate Change: Climate Agreement of Paris. 1–25. Available: https://unfccc.int/process-and-meetings/the-paris-agreement/the-paris-agreement.

Weiss, A.D. 1983. Scanning Electron Microscopes. *Semiconductor International*. 6(10):90–94. DOI: 10.1016/s0026-0576(03)90123-1.

Whiteman Adrian, Akande Dennis, Elhassan Nazik, Escamilla Gerardo, Lebedys Arvydas & Arkhipova Iana. 2021. *RENEWABLE CAPACITY STATISTICS 2021 STATISTIQUES DE CAPACITÉ RENOUVELABLE 2021 ESTADÍSTICAS DE CAPACIDAD RENOVABLE 2021*. Available: www.irena.org.

Xie, M., Chu, T., Wang, T., Wan, K., Yang, D., Li, B., Ming, P. & Zhang, C. 2021. Preparation, performance and challenges of catalyst layer for proton exchange membrane fuel cell. *Membranes*. 11(11). DOI: 10.3390/membranes11110879.

Xu, W. & Scott, K. 2010. The effects of ionomer content on PEM water electrolyser membrane electrode assembly performance. *International Journal of Hydrogen Energy*. 35(21):12029–12037. DOI: 10.1016/j.ijhydene.2010.08.055.

7 APPENDICES

7.1 Appendix A

Table 7.1 provides a detailed breakdown of the ink calculations conducted as part of this research study. This data presents a comprehensive overview of the ink formulation, quantity, and other relevant parameters.

Table 7.1: Ink calculations

Fixed parameters				MEA characterisitics			
Desired ink volume	60	ml		Loading	3,02871	mg/cm^2	
Solvent choice	IPA			Active area	25	cm^2/MEA	
				Approximate sprayer efficiency	0,39063		
Ink composition				Number of MEAs required	12	MEA	
Solids	0,050	wt. frac.					
Ionomer content in solids	0,116	wt. frac.					
Catalyst content in solids	0,884	wt. frac.					
Solvent	0,475	wt. frac.					
Water	0,475	wt. frac.			Density		
				Methanol	0,792	g/ml	
Calculated parameters				Ethanol	0,789	g/ml	
Mass of water	26,42	g		Isopropanol	0,786	g/ml	
Mass of solvent	26,42	g		Water	1	g/ml	
Volume of water	26,42	ml					
Volume of solvent	33,48	ml		density = m/v			
Total ink volume	59,90	ml					
Total ink mass	52,83	g					
Mass of dry ionomer	0,32	g					
Mass of Nafion D2020 ionomer solution	1,61	g					
Mass of carbon	0,70	g					
Mass of catalyst	2,46	g					
Summary of materials needed							
Nafion D2021 ionomer solution	1,61	g					
Catalyst	2,46	g					
Mass of water	26,42	g					
Mass of solvent	26,42	g					
Sprayer							
Sprayer height	4,8	cm					
Spraying pattern	horizontal and vertical						
Spraying velocity							
Ink volume per pass	0,634	ml					
Catalyst content per pass	25,9750813	mg					
Catalyst content that reaches active area	10,14651613	mg					
Catalyst loading attained per pass	0,405860645	mg/cm^2					
Approximate number of passes needed	7						

7.2 Appendix B

In Figure 7.1 SEM images are presented showcasing agglomerates used for measuring the average agglomerate size in samples AL2 and AL5. The SEM images show a visual representation of the agglomerate structures. Accompanying these SEM images is a detailed Table 7.2 that outlines the measuring lengths.

AL2/µm

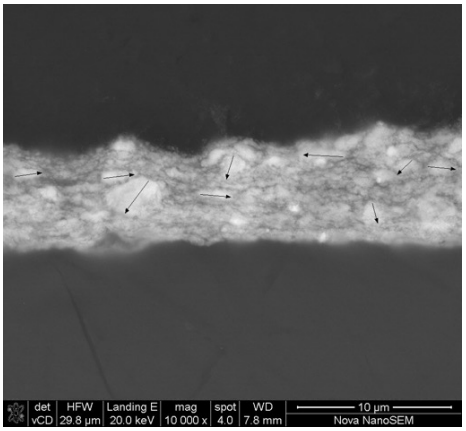

AL5/µm

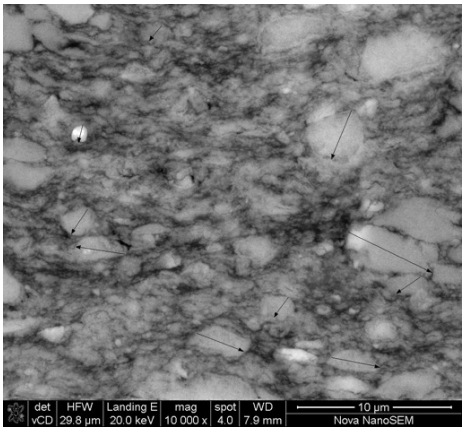

Figure 7.1: SEM Images of Agglomerates in Samples AL2 and AL5

Table 7.2: Measuring Lengths for Agglomerates in Samples AL2 and AL5

	AL2/um	Z distribution AL2			AL5/um	Z distribution AL5
AG1	1,06	0,27		AG1	0,80	0,09077124
AG2	1,18	0,32		AG2	1,18	0,101271644
AG3	1,24	0,35		AG3	1,25	0,103323138
AG4	1,29	0,37		AG4	1,32	0,105004293
AG5	1,36	0,40		AG5	1,47	0,108947862
AG6	1,37	0,40		AG6	1,58	0,111689041
AG7	1,47	0,44		AG7	1,59	0,111810325
AG8	1,58	0,48		AG8	1,86	0,118087738
AG9	1,63	0,50		AG9	1,93	0,119654849
AG10	1,77	0,53		AG10	2,82	0,133564166
AG11	1,81	0,53		AG11	3,21	0,136207257
AG12	1,87	0,54		AG12	3,21	0,13621443
AG13	2,04	0,53		AG13	3,28	0,136410391
AG14	2,05	0,53		AG14	3,42	0,136611951
AG15	2,09	0,53		AG15	3,43	0,136613801
AG16	2,48	0,41		AG16	4,31	0,130651172
AG17	2,64	0,34		AG17	4,70	0,124481385
AG18	2,66	0,33		AG18	6,08	0,090774051
AG19	2,91	0,22		AG19	7,50	0,051885343
AG20	4,11	0,01		AG20	13,80	0,000251254
Average	1,93			Average	3,44	
Std	0,74			Std	2,92	

7.3 Appendix C

In this section, a series of EDS maps are presented for samples NH1/NS2, NH2, NH3, NS3, and NS1.

NH1/NS2

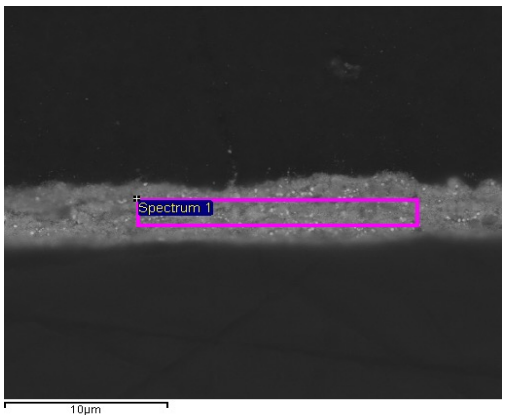

NH2

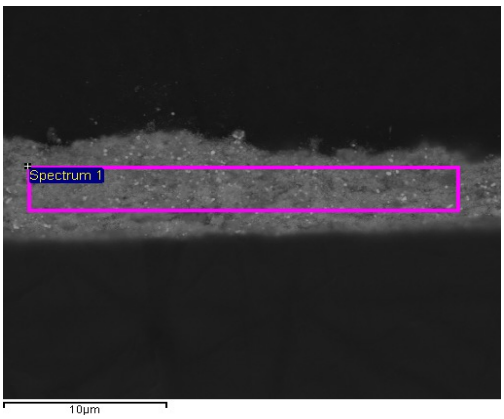

NH3

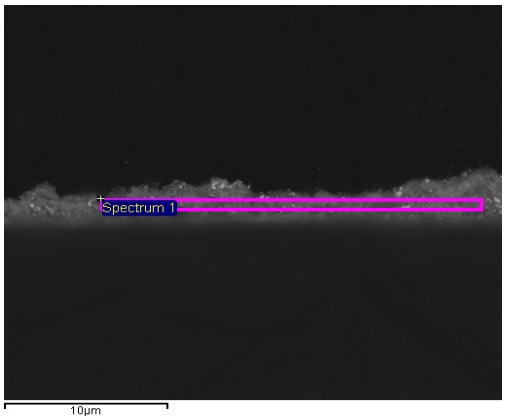

NS3

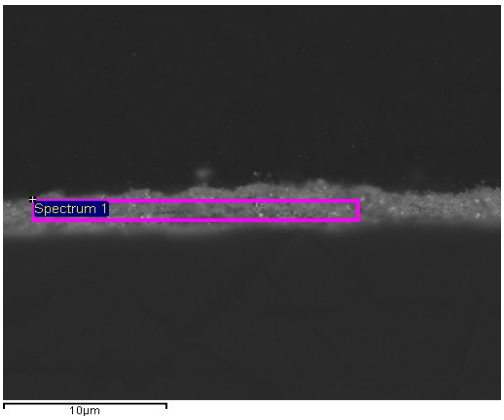

NS1

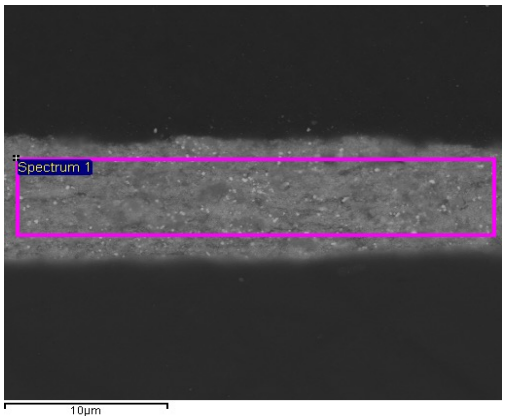

Table 7.3: EDS Maps for Sample NH1/NS2, NH2, NH3, NS3, and NS1

7.4 Appendix D

In this section, the STEM-EDS process and conditions used for analysis are recorded for sample NH1, NH3 and NS1

Table 7.4: STEM-EDS conditions

Priority	Sample Code	HySA Code	Anode Composition	Anode Ir Loading / mg_{Ir} cm^{-2}	Anode Ionomer Loading / wt.% (dry electrode basis)	Cathode Composition	Cathode Pt Loading / mg_{Pt} cm^{-2}	Cathode Ionomer Loading / wt.% (dry electrode basis)	Anode EDX map	Cathode EDX map	Notes
NH1	020621-CCM-01	NM-CCM240220-01	Ir, Ti, O, Nafion	1.87	12	No cathode	NA	NA	Yes: 1 lower mag (e.g 7K) and 2 higher mag (e.g. 79K)	No	Required: **Regular STEM images for anode only**: 1 at 7K and 2 at 79k magnification. Please perform **EDX maps: 7K-1 map and 79K-2 maps for anode only**. The only deliverable are images from those maps: distribution of elements (**individual and overlap: Ir, Ti, O and F**). No further data processing is required.
NH3	020621-CCM-02	NM-CCM240220-03	Ir, Ti, O, Nafion	1.27	12	No cathode	NA	NA	Yes: 1 lower mag (e.g 7K) and 2 higher mag (e.g. 79K)	No	Required: **Regular STEM images for anode only**: 1 at 7K and 2 at 79k magnification. Please perform **EDX maps: 7K-1 map and 79K-2 maps for anode only**. The only deliverable are images from those maps: distribution of elements (**individual and overlap: Ir, Ti, O and F**). No further data processing is required.
NS1	020621-CCM-03	NM-CCM240220-05	Ir, Ti, O, Nafion	2.84	12	No cathode	NA	NA	Yes: 1 lower mag (e.g 7K) and 2 higher mag (e.g. 79K)	No	Required: **Regular STEM images for anode only**: 1 at 7K and 2 at 79k magnification. Please perform **EDX maps: 7K-1 map and 79K-2 maps for anode only**. The only deliverable are images from those maps: distribution of elements (**individual and overlap: Ir, Ti, O and F**). No further data processing is required.
AL1	020621-CCM-04	NM-CCM211220-01	Ir, O, Nafion	0.54	12	No cathode	NA	NA	Yes: 1 lower mag (e.g 7K) and 2 higher mag (e.g. 79K)	No	Required: **Regular STEM images for anode only**: 1 at 7K and 2 at 79k magnification. Please perform **EDX maps: 7K-1 map and 79K-2 maps for anode only**. The only deliverable are images from those maps: distribution of elements (**individual and overlap: Ir, O and F**). No further data processing is required.
AL3	020621-CCM-05	NM-CCM211220-03	Ir, O, Nafion	2.06	12	No cathode	NA	NA	Yes: 1 lower mag (e.g 7K) and 2 higher mag (e.g. 79K)	No	Required: **Regular STEM images for anode only**: 1 at 7K and 2 at 79k magnification. Please perform **EDX maps: 7K-1 map and 79K-2 maps for anode only**. The only deliverable are images from those maps: distribution of elements (**individual and overlap: Ir, O and F**). No further data processing is required.
AL4	020621-CCM-06	NM-CCM211220-04	Ir, O, Nafion	3.99	12	No cathode	NA	NA	Yes: 1 lower mag (e.g 7K) and 2 higher mag (e.g. 79K)	No	Required: **Regular STEM images for anode only**: 1 at 7K and 2 at 79k magnification. Please perform **EDX maps: 7K-1 map and 79K-2 maps for anode only**. The only deliverable are images from those maps: distribution of elements (**individual and overlap: Ir, O and F**). No further data processing is required.

NH1

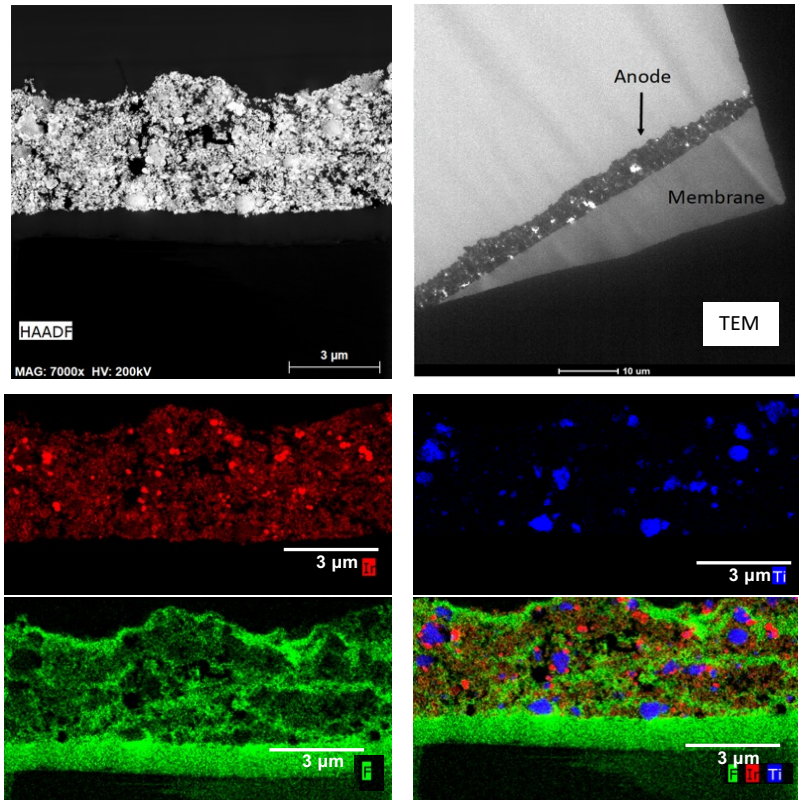

Table 7.5: NH1 STEM-EDS and TEM Analysis

NH3

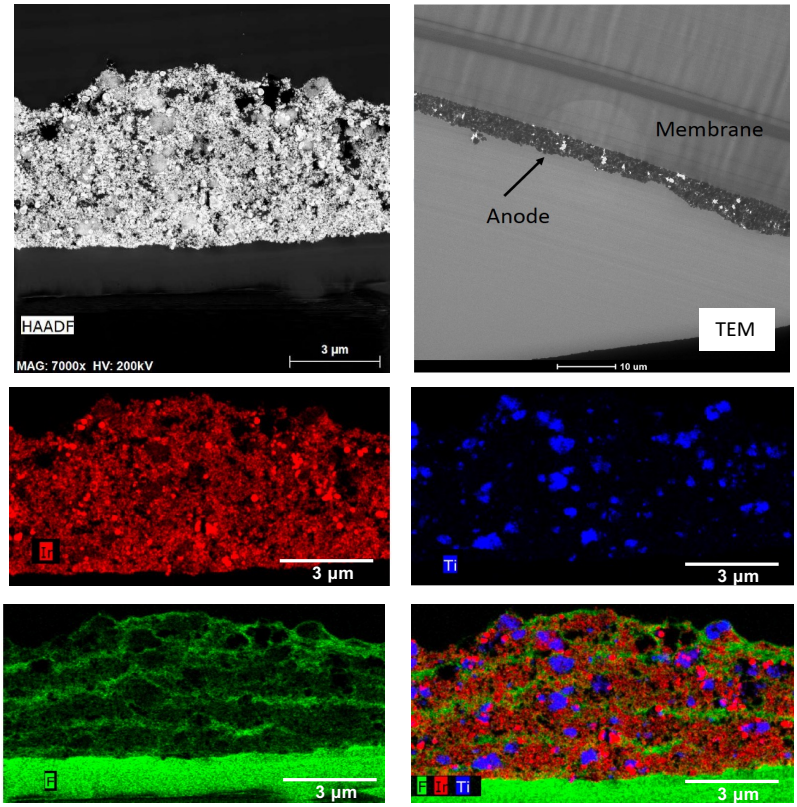

NS1

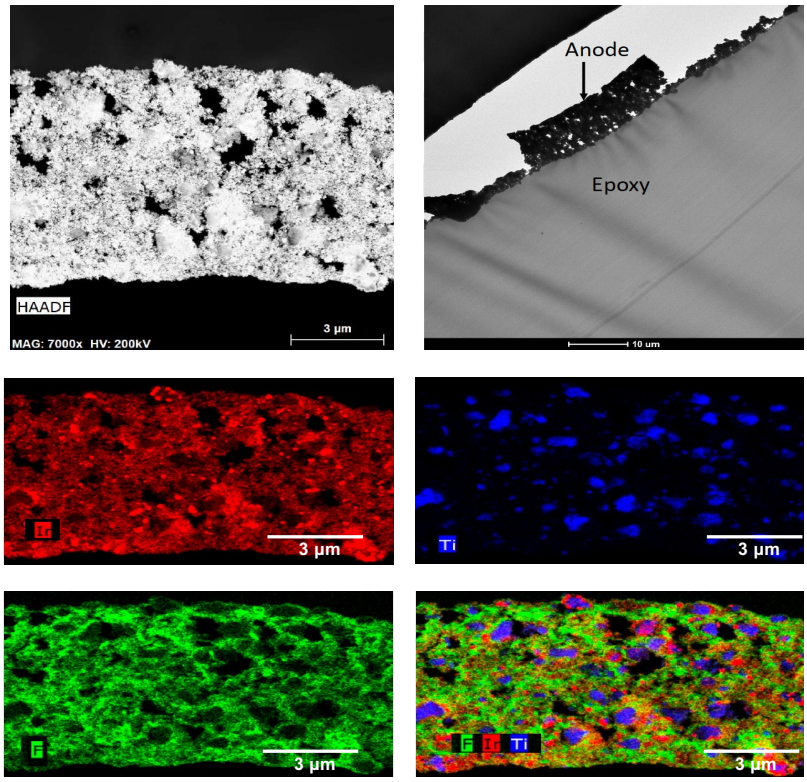

Figure 7.2: NH3 and NS1 sample STEM-EDS and TEM Analysis